Hong Kong Journal of Radiology

Vol. 27 No. 1, 2024 Pages e1-76

Hong Kong Journal of Radiology

HKJR

香港放射科醫學雜誌

VOLUME 27 · NUMBER 1 · 2024

ISSN 2307-4620

Highlights of this issue:

- Tolerability and Efficacy of Palbociclib and Ribociclib in Breast Cancer in Hong Kong: A Single-Centre Study
- Contrast-Enhanced Ultrasound with Perfluorobutane for Hepatocellular Cancer Surveillance: Our Initial Local Experience
- Pathologies and Postoperative Features of Posterior Tibial Tendon Dysfunction: A Pictorial Essay

In the article "Contrast-Enhanced Ultrasound with Perfluorobutane for Hepatocellular Cancer Surveillance: Our Initial Local Experience". Hepatocellular carcinoma (arrow). Perfluorobutane-enhanced ultrasound images in arterial phase showing the lesion to be arterial hyperenhancing.

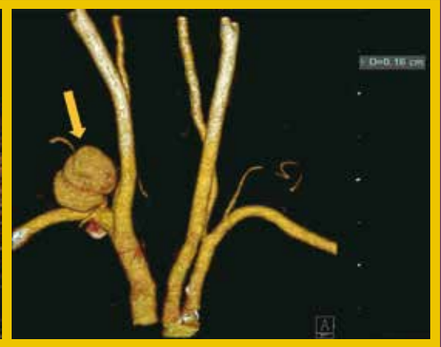

In the article "Endovascular Management of Iatrogenic Neck Vascular Injury After Central Venous Catheterisation". Three-dimensional reformats of the computed tomography angiogram showing a right subclavian artery pseudoaneurysm (arrow) formed after right internal jugular vein split catheter insertion.

Official Publication of
Hong Kong College of Radiologists

HKAM PRESS

HKJR

COVER IMAGES

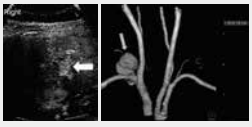

..... SEE PAGES e23 & e70

Hong Kong Journal of Radiology

Hong Kong Journal of Radiology is a continuation of the *Journal of the Hong Kong College of Radiologists*. This journal is dedicated to publish all aspects of clinical oncology, diagnostic radiology, and nuclear medicine.

VOLUME 27 • NUMBER 1 • MARCH 2024

Editorial

Original Articles

Case Reports

Pictorial Essays

When citing this journal, abbreviate as ***Hong Kong J Radiol***.

The Hong Kong Society of Diagnostic Radiologists Trust Fund

Hong Kong Society of Diagnostic Radiologists Research Grant

The Hong Kong Society of Diagnostic Radiologists (HKSDR) was founded in 1977 to promote interflow of professional knowledge in diagnostic radiology and to foster close contact among doctors working in the field of diagnostic radiology. The HKSDR Trust Fund was established in 1985.

Taking into account the rapid progress in imaging technology and thus the need to promote research to advance our knowledge and to serve our patients better, the Trust Fund offers three awards of up to HK$17,000 each and is open to application.

The application should be made by the principal investigator of the research project related to the scientific or clinical aspects of diagnostic radiology to be conducted in Hong Kong. The principal investigator should be a trainee/specialist in the field of diagnostic radiology. He/she has to be a registered medical practitioner in Hong Kong.

Application and enquiry can be directed to:

Dr. Lam Chiu Ying Flora, Hon Secretary of Trust Fund Working Group
c/o Ms. HY Ng, Department of Diagnostic & Interventional Radiology
Kwong Wah Hospital
25 Waterloo Road, Yaumatei, Kowloon, Hong Kong.
Tel: (852) 3517 5189

Hong Kong Journal of Radiology

Aims and Editorial Policy

Hong Kong Journal of Radiology **香港放射科醫學雜誌** is the official peer-reviewed academic journal of Hong Kong College of Radiologists, a founder College of the Hong Kong Academy of Medicine. The Journal is published online quarterly and is indexed in EMBASE/*Excerpta Medica*, SCOPUS, Emerging Sources Citation Index, and Index Copernicus. Papers are published on all aspects of diagnostic imaging, clinical oncology, and nuclear medicine, including original research, editorials, review articles, and case reports. Papers on radiological protection, quality assurance, audit in radiology, and matters related to radiological training or education are included.

All papers submitted are subject to peer review, and the Editorial Board reserves the right to edit papers in preparation for publication in the Journal. Authors are asked to refer to the *Information for Authors* published in each issue of the Journal, regarding the style and presentation of their articles. Failure to do so may result in rejection of their papers by the Editorial Board.

Manuscripts should be submitted online via the HKAMedTrack <www.hkamedtrack.org/hkjr>. Correspondence should be sent to:

Managing Editor, HKJR Editorial Office
c/o Hong Kong Academy of Medicine Press
10/F, Hong Kong Academy of Medicine Jockey Club Building
99 Wong Chuk Hang Road, Aberdeen, Hong Kong
Tel: (852) 2871 8809; Fax: (852) 2515 9061
Email: hkjr@hkam.org.hk

Advertisements

Correspondence concerning advertisements should be addressed to:

Executive Assistant
Hong Kong College of Radiologists
Room 909, 9/F Hong Kong Academy of Medicine Jockey Club Building
99 Wong Chuk Hang Road, Aberdeen, Hong Kong.
Tel: (852) 2871 8788; Fax: (852) 2554 0739
Email: hkjr@hkcr.org

Reprints

Reprints of individual articles are available to authors only. Reprints in large quantities (non-authors), for commercial or academic use, may be purchased from the publisher. For information and prices, please send an email to: hkjr@hkam.org.hk.

Copyright

On acceptance of an article by the Journal, the corresponding author will be asked to transfer copyright of the article to the College. The Copyright Transfer Assignment Form will be sent to the author at the time of acceptance.

Disclaimer

Hong Kong Journal of Radiology and the publisher do not guarantee, directly or indirectly, the quality or efficacy of any product or service described in the advertisements or other material which is commercial in nature in this issue. All articles published, including editorials and letters, represent the opinions of the authors and do not reflect the official policy of the Journal, Hong Kong College of Radiologists, the publisher, or the institution with which the author is affiliated, unless this is clearly specified.

Hong Kong Journal of Radiology
Online ISSN: 2307-4620

Hong Kong J Radiol. 2024;27(1):e4. Published 23 February 2024 | https://doi.org/10.12809/hkjr24ed

EDITORIAL

The shift to online publishing and promoting innovation in the *Hong Kong Journal of Radiology*

WCW Chu

Editor-in-Chief, *Hong Kong Journal of Radiology*

To support a greener future and embrace digital advances, the *Hong Kong Journal of Radiology* (HKJR) will switch to an online-only format this year. We will continue to publish four issues annually, on a quarterly basis. Articles will be available on our website as soon as they are ready, before they are collated in an issue. This will enable readers to access the most up-to-date research and insights in a timely manner. Articles will be featured separately as well as in an issue that will be accessible with just one click.

Last year, for the first time, our journal achieved a journal impact factor of 0.2 (Clarivate, 2023). My sincere thanks to the dedication and tireless efforts of our esteemed editorial board members, reviewers, editorial office staff, and everyone else involved for their valuable contributions and unwavering support. Our open access publishing option increases accessibility to research, potentially attracting more authors and readers to our journal. In addition, we have been striving to publish high-quality research articles, case studies, and reviews that address current and emerging trends in radiology. Our robust peer review process encourages timely and constructive feedback from reviewers to ensure publication of the highest quality accurate and relevant research. Looking forward, we will explore the use of digital platforms to expand the reach of the journal. Apart from the existing user-friendly website with enhanced search functions, our articles can be promoted via social media channels with multimedia content such as video summaries to engage a broader audience.

We invite researchers, clinicians, and scholars to contribute their valuable insights to our journal. The HKJR is dedicated to showcasing the most recent advances, interesting cases, novel techniques, and opinions on a specific topic or issue. Popular topics include emerging trends in clinical oncology and the application of artificial intelligence in clinical practice. Submission guidelines and instructions are featured on our journal's website. We look forward to receiving your valuable contributions. Together we can advance the frontiers of radiological knowledge and improve patient care through innovative research and expertise.

Correspondence: *Prof WCW Chu, Editor-in-Chief, Hong Kong Journal of Radiology*
Email: hkjr@hkam.org.hk

Hong Kong J Radiol. 2024;27(1):e5-15. Published 13 March 2024 | https://doi.org/10.12809/hkjr2317720

ORIGINAL ARTICLE

CME

Tolerability and Efficacy of Palbociclib and Ribociclib in Breast Cancer in Hong Kong: A Single-Centre Study

JLC Hung, IS Soong

Department of Clinical Oncology, Pamela Youde Nethersole Eastern Hospital, Hong Kong SAR, China

ABSTRACT

Introduction: *This study aimed to analyse the safety, tolerability, and other potential factors affecting the treatment outcome of advanced breast cancer (including inoperable stage III or stage IV, as per the eighth edition of the American Joint Committee on Cancer staging manual) treated with palbociclib or ribociclib at a single institution in Hong Kong.*

Methods: *The medical records of all breast cancer patients receiving palbociclib or ribociclib at a hospital in Hong Kong during the period of July 2016 to February 2022 were reviewed. Data regarding baseline demographics, treatment-related adverse events, need for dose reduction, and disease progression were collected.*

Results: *A total of 211 patients were included in the study, where 88.6% received palbociclib and 11.4% received ribociclib. Among the patients started on full doses (91.4% for palbociclib and 91.7% for ribociclib), 48.5% and 54.5% required dose reduction, respectively, most often due to neutropenia. No statistically significant factor could be identified for predicting the severity of neutropenia in this cohort. In patients on first-line treatment, dose reduction, treatment delay, high levels of oestrogen receptor and progesterone receptor were associated with longer progression-free survival, with respective p values of < 0.001, 0.010, 0.002, and 0.001.*

Conclusion: *Palbociclib and ribociclib were safe and well-tolerated in a predominantly Asian population in real-life clinical practice, with comparable treatment outcomes to those quoted in international clinical trials. Dose reduction did not compromise the treatment efficacy.*

Key Words: *Asian; Breast neoplasms; Drug tolerance; Hong Kong*

Correspondence: *Dr JLC Hung, Department of Clinical Oncology, Pamela Youde Nethersole Eastern Hospital, Hong Kong SAR, China*
Email: hlc388@ha.org.hk

Submitted: 6 April 2023; Accepted: 15 August 2023.

Contributors: Both authors designed the study. JLCH acquired and analysed the data, and drafted the manuscript. Both authors critically revised the manuscript for important intellectual content. Both authors had full access to the data, contributed to the study, approved the final version for publication, and take responsibility for its accuracy and integrity.

Conflicts of Interest: As an editor of the journal, JLCH was not involved in the peer review process. ISS has disclosed no conflicts of interest.

Funding/Support: This research received no specific grant from any funding agency in the public, commercial, or not-for-profit sectors.

Data Availability: All data generated or analysed during the present study are available from the corresponding author on reasonable request.

Ethics Approval: This research was approved by the Hong Kong East Cluster Research Ethics Committee of Hospital Authority, Hong Kong (Ref No.: HKECREC-2022-67). The requirement for informed patient consent was waived by the Committee due to the retrospective nature of the study.

Supplementary Material: The supplementary material was provided by the authors and some information may not have been peer reviewed. Any opinions or recommendations discussed are solely those of the author(s) and are not endorsed by the Hong Kong College of Radiologists. The Hong Kong College of Radiologists disclaims all liability and responsibility arising from any reliance placed on the content. To view the file, please visit the journal online (https://doi.org/10.12809/hkjr2317720).

中文摘要

在香港使用帕博西尼及瑞博西尼治療乳癌的耐受性及效用：單一中心研究

孔朗程、宋崧

引言：本研究旨在分析在香港某所醫院使用帕博西尼及瑞博西尼治療晚期乳癌（包括根據美國癌症聯合委員會癌症分期系統第8版分類的無法進行手術的第III期或第IV期）的安全性、耐受性及影響治療結果的其他潛在因素。

方法：我們回顧了2016年7月至2022年2月期間所有在香港某所醫院接受帕博西尼或瑞博西尼治療的乳癌患者的醫療紀錄，收集的資料包括基線人口特徵、與治療相關的不良事件、減少劑量的需要及病情惡化情況。

結果：本研究共包括211名患者，當中88.6%使用帕博西尼，11.4%使用瑞博西尼。在開始時使用全劑量的患者中（91.4%使用帕博西尼的患者及91.7%使用瑞博西尼的患者），分別有48.5%及54.5%需要減少劑量，大多由嗜中性白血球減少症引致。在預測本隊列的嗜中性白血球減少症的嚴重程度方面，我們找不到具統計學意義的因素。在接受一線治療的患者中，減少劑量、延遲治療、雌激素受體及孕酮受體水平偏高與較長的疾病無惡化存活相關，p值分別為< 0.001、0.010、0.002及0.001。

結論：在以亞裔人口為主的真實臨床診療情況中，帕博西尼及瑞博西尼是安全及具耐受性的藥物，其治療結果與多個國際臨床試驗所引述的相若。減少劑量並無降低治療效用。

INTRODUCTION

Breast cancer is the leading type of female cancer in Hong Kong, accounting for 27.4% of female cancers diagnosed in 2019,[1] of which approximately 70% to 80% exhibit oestrogen receptor (ER) and/or progesterone receptor (PR) positivity.[2]

Cyclin-dependent kinase 4 and 6 (CDK4/6) inhibitors have been established as the standard of care in hormone receptor–positive, human epidermal growth factor receptor 2 (HER2)–negative advanced breast cancer not at risk of imminent visceral compromise,[3] based on their superior treatment effect in landmark registration trials (i.e., the clinical trials that led the drugs to their approval by the United States Food and Drug Administration [FDA]).[4-12]

Palbociclib, ribociclib, and abemaciclib are the three CDK4/6 inhibitors currently available in Hong Kong.[13-15] Abemaciclib was not made available in the Hospital Authority Drug Formulary until 11 July 2020.[16]

We hereby present our data in a real-life cohort of patients from an institution in Hong Kong. We aimed to analyse the safety and tolerability of palbociclib and ribociclib in our centre. We sought to evaluate for any association between various clinicopathological and treatment-related factors such as dose reduction or occurrences of dose delay and treatment outcome, and whether the treatment outcomes demonstrated in international trials were reproducible in Asians.

METHODS

Data Collection

All patients who received palbociclib or ribociclib for treating advanced breast cancer (including inoperable stage III or stage IV, as per the eighth edition of the American Joint Committee on Cancer staging manual) during the period from July 2016 to February 2022 at Pamela Youde Nethersole Eastern Hospital were included in the study. Medical records were reviewed for data collection.

Study Objectives

The primary objective of this study was the safety and tolerability of treatment, as measured by the frequencies of adverse events (AEs) and need for dose reductions. Toxicities were charted based on patients' self-reported symptoms and the regular review of laboratory results before each cycle. AEs were graded according to the Common Terminology Criteria for Adverse Events version 5.0.

The secondary objective was the treatment outcome as reflected by the progression-free survival (PFS), which is defined as the time from treatment commencement until the date of clinical or radiological progression of measurable disease or death due to any cause. Disease was assessed by physical examination at each visit and regular imaging, including computed tomography or positron emission tomography–computed tomography scan that was usually performed at 4- to 6-month intervals. Patients were followed up from date of CDK4/6 inhibitor commencement till date of disease progression or death.

Patients without evidence of disease progression at the time of data cut-off (on 30 November 2022) or those who defaulted follow-up were censored. Those who developed disease progression or expired due to any cause during treatment were defined as having had an event.

Statistical Analysis

Statistical analysis was conducted by SPSS (Windows version 26.0; IBM Corp, Armonk [NY], United States). Continuous variables were analysed by independent sample *t* tests. Categorical variables were analysed by Pearson's Chi squared test or Fisher's exact test. The Kaplan–Meier method was used for estimation of the PFS, with comparison made via the log-rank test. The effects of multiple patient factors and of clinicopathological and treatment-related factors on the PFS were studied by the Cox proportional hazard model. Factors deemed statistically significant (with a p value < 0.05) on univariate analysis were further analysed by multivariable analysis.

This manuscript was prepared in accordance with the STROBE (Strengthening the Reporting of Observational Studies in Epidemiology) guidelines.

RESULTS

Patient Demographics

Patient demographics are detailed in Table 1. A total of 211 female patients with a median age of 61 years (range, 36-89) were included in the study, of which 96.7% were Chinese, 2.8% were other Asians, and 0.5% were Caucasians. A total of 77.7% had an Eastern Cooperative Oncology Group performance status (ECOG PS) score of 0-1 at the start of treatment, and 11.4% and 10.9% were of ECOG PS score of 2 or 3, respectively. A total of 88.6% received palbociclib and 11.4% received ribociclib, with 57.3% receiving palbociclib or ribociclib as first-line therapy and 18.0% and 24.6% receiving one of the drugs for second-line, third-line, or beyond. The median duration of follow-up was 387 days (range, 5-2024).

Primary Outcome: Treatment Safety and Tolerability

Occurrence of Adverse Events

The occurrence of AEs (by toxicity grades) and onset time (in weeks) are displayed in Table 2. The most commonly observed AE of all grades was neutropenia (96.2%), followed by anaemia (80.6%) and thrombocytopaenia (66.4%). In all, 72.5% experienced Grade ≥ 3 neutropenia, though the overall incidence of febrile neutropenia was low (3.3%). Of note, one patient (0.5%) experienced grade 5 hyperbilirubinaemia and grade 4 thrombocytopaenia after 5.72 months of ribociclib, dying of liver failure.

Occurrence of Dose Adjustments

In all, 171 out of 187 patients (91.4%) on palbociclib and 22 out of 24 patients (91.7%) on ribociclib were started on the standard dose (Table 1). The remaining patients were started on a reduced dose due to advanced age or poor ECOG PS upon their physician's discretion.

Among the patients on the standard starting dose, 48.5% on palbociclib and 54.5% on ribociclib required dose reduction, most commonly due to neutropenia. The pattern and cause of dose reduction among patients on standard starting doses are shown in Figures 1 and 2, respectively. Dose reduction was largely adherent to the recommended dosing levels of the FDA. Other dose reductions included five weekly cycles or '2 weeks on 2 weeks off' regimens.

Patient Factors on the Presentation of Neutropenia

We analysed the association of multiple patient factors on the grade of neutropenia, including age, ECOG PS score, presence of bone metastasis, first-line vs. later treatment, and prior chemotherapy exposure. No statistically significant predicting factors could be identified. The results are detailed in Table 3.

Secondary Outcome: Treatment Outcome

At the time of data cut-off, 59% (n = 125) patients experienced an event of which 56% (n = 119) experienced disease progression and 3% (n = 6) died due to causes unrelated to oncological illness. A total of 40% (n = 84) patients did not experience disease progression. A total of 1% of patients (n = 2) were censored due to lack of follow-up.

Table 1. Patient demographics (n = 211).*

	Subgroup	No. (%)
Median age, y		61 (range, 36-89)
Age-group, y	≤ 40	7 (3.3%)
	41-60	95 (45.0%)
	61-75	89 (42.2%)
	≥ 76	20 (9.5%)
Eastern Cooperative Oncology Group performance status score	0	4 (1.9%)
	1	160 (75.8%)
	2	24 (11.4%)
	3	23 (10.9%)
Race	Chinese	204 (96.7%)
	Other Asians	6 (2.8%)
	Caucasians	1 (0.5%)
Allred score–oestrogen receptor	0-2	0
	3-5	7 (3.3%)
	6-8	190 (90.1%)
	Missing	14 (6.6%)
Allred score–progestogen receptor	0-2	35 (16.6%)
	3-5	50 (23.7%)
	6-8	112 (53.1%)
	Missing	14 (6.6%)
Disease-free interval	*De novo*	89 (42.2%)
	≤12 mo	6 (2.8%)
	13-24 mo	10 (4.7%)
	>24 mo	106 (50.2%)
No. of metastatic sites	0	2 (0.9%)
	1	69 (32.7%)
	2	42 (19.9%)
	3	45 (21.3%)
	4	29 (13.7%)
	5	17 (8.1%)
	≥ 6	7 (3.3%)
Distribution of metastatic sites	Bone	153 (72.5%)
		Bone only: 35 (16.6%)†
	DLN	119 (56.4%)
		DLN only: 14 (6.6%)†
	Lung	103 (48.8%)
		Lung only: 13 (6.2%)†
	Liver	60 (28.4%)
		Liver only: 4 (1.9%)†
	Brain	7 (3.3%)
	Others	39 (18.5%)
Upfront treatment used in advanced breast cancer	Tamoxifen	5 (2.4%)
	Aromatase inhibitors	24 (11.4%)
	Aromatase inhibitors + ovarian ablation	2 (0.9%)
	Chemotherapy	46 (21.8%)
	CDK4/6 inhibitors	121 (57.3%)
	Others	13 (6.2%)
Series of treatments	First-line	121 (57.3%)
	Second-line	38 (18.0%)
	Third-line or beyond	52 (24.6%)
Hormone used with CDK4/6 inhibitor	Letrozole	126 (59.7%)
	Exemestane	14 (6.6%)
	Anastrozole	5 (2.4%)
	Fulvestrant	64 (30.3%)
	Others‡	2 (0.9%)
CDK4/6 inhibitor used	Palbociclib	187 (88.6%)
	Ribociclib	24 (11.4%)
Starting dose–palbociclib, mg daily (n = 187)	125	171 (91.4%)
	100	13 (7.0%)
	75	3 (1.6%)
Starting dose–ribociclib, mg daily (n = 24)	600	22 (91.7%)
	400	1 (4.2%)
	200	1 (4.2%)
Local ablative therapy before or during CDK4/6 inhibitor treatment	Yes	46 (21.8%)§
	No	165 (78.2%)

Abbreviations: CDK4/6 = cyclin-dependent kinase 4 and 6; DLN = distant lymph node.

* Data are shown as No. (%), unless otherwise specified.

† Patients only had metastasis over the corresponding sites without other metastatic involvement.

‡ One patient was under study, and one patient was initially started on fulvestrant then switched to exemestane as the patient was unfit to continue with injections.

§ Twelve patients (26.1%) during CDK4/6 inhibitor treatment and 34 patients (73.9%) before CDK4/6 inhibitor treatment.

Table 2. Occurrence of common adverse events (by toxicity grades) and onset time (in weeks).*

	All patients (n = 211)	Palbociclib only (n = 187)	Ribociclib only (n = 24)
Neutropenia			
Any grade	203 (96.2%)	181 (96.8%)	22 (91.7%)
Grade ≥ 3	153 (72.5%)	136 (72.7%)	17 (70.8%)
Onset time	3 (1-90)	3 (1-90)	3.5 (2-84)
Anaemia			
Any grade	170 (80.6%)	153 (81.8%)	17 (70.8%)
Grade ≥ 3	27 (12.8%)	25 (13.4%)	2 (8.3%)
Onset time	4 (1-213)	4 (1-213)	4 (2-188)
Thrombocytopaenia			
Any grade	140 (66.4%)	126 (67.4%)	14 (58.3%)
Grade ≥ 3	13 (6.2%)	11 (5.9%)	2 (8.3%)
Onset time	3 (1-97)	3 (1-97)	8.5 (2-45)
Febrile neutropenia			
Yes	7 (3.3%)	7 (3.7%)	0
No	204 (96.7%)	180 (96.3%)	24 (100%)
Onset time	3 (2-88)	3 (2-88)	N/A
Diarrhoea			
Any grade	35 (16.6%)	31 (16.6%)	4 (16.7%)
Grade ≥ 3	1 (0.5%)	1 (0.5%)	0
Onset time	8 (1-84)	8 (1-84)	12.5 (5-47)
Fatigue			
Any grade	46 (21.8%)	43 (23.0%)	3 (12.5%)
Grade ≥ 3	6 (2.8%)	5 (2.7%)	1 (4.2%)
Onset time	5 (1-75)	5 (1-75)	20 (2-24)
Nausea			
Any grade	24 (11.4%)	21 (11.2%)	3 (12.5%)
Grade ≥ 3	1 (0.5%)	1 (0.5%)	0
Onset time	7 (1-26)	7 (1-26)	2 (2-21)
ALT elevation			
Any grade	43 (20.4%)	36 (19.3%)	7 (29.2%)
Grade ≥ 3	1 (0.5%)	1 (0.5%)	0
Onset time	11 (1-178)	9 (1-178)	14 (1-150)
Prolonged QTc interval			
Any grade	22/94 (23.4%)	13/71 (18.3%)	9/23 (39.1%)
Grade ≥ 3	4/94 (4.3%)	2/71 (2.8%)	2/23 (8.7%)
Missing (excluded from the percentage)	117	116	1
Onset time	4 (1-54)	4 (1-54)	2 (1-32)
Non-neutropenic infection requiring hospitalisation			
Yes	17 (8.1%)	16 (8.6%)	1 (4.2%)
No	194 (91.9%)	171 (91.4%)	23 (95.8%)
Onset time	9.5 (3-233)	10 (4-233)	3
Mucositis			
Any grade	62 (29.4%)	55 (29.4%)	7 (29.2%)
Grade ≥ 3	1 (0.5%)	0	1 (4.2%)
Onset time	9 (1-93)	8 (1-93)	21 (4-86)
Rash			
Any grade	17 (8.1%)	13 (7.0%)	4 (16.7%)
Grade ≥ 3	0	0	0
Onset time	5 (1-39)	6 (1-39)	4 (2-20)
Hand/foot syndrome			
Any grade	4 (1.9%)	4 (2.1%)	0
Grade ≥ 3	1 (0.5%)	1 (0.5%)	0
Onset time	19 (2-79)	19 (2-79)	N/A
Peripheral neuropathy			
Any grade	5 (2.4%)	5 (2.7%)	0
Grade ≥ 3	0	0	0
Onset time	6 (3-48)	6 (3-48)	N/A
Alopecia			
Any grade	4 (1.9%)	4 (2.1%)	0
Grade ≥ 3	0	0	0
Onset time	6 (4-16)	6 (4-16)	N/A

Abbreviations: ALT = alanine aminotransferase; N/A = not available.
* Data are shown as No. (%) or median (range), unless otherwise specified.

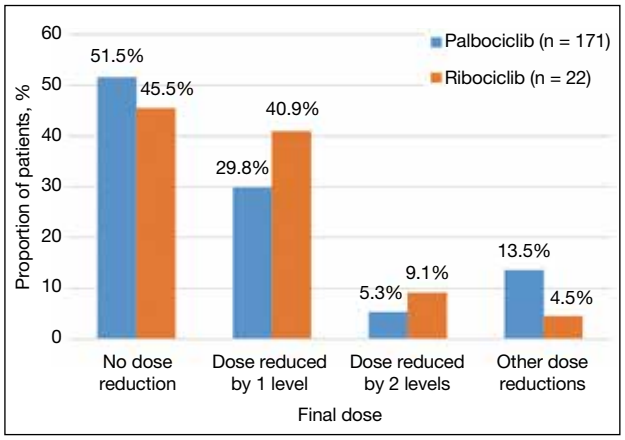

Figure 1. Pattern of dose reduction in patients on standard starting dose.

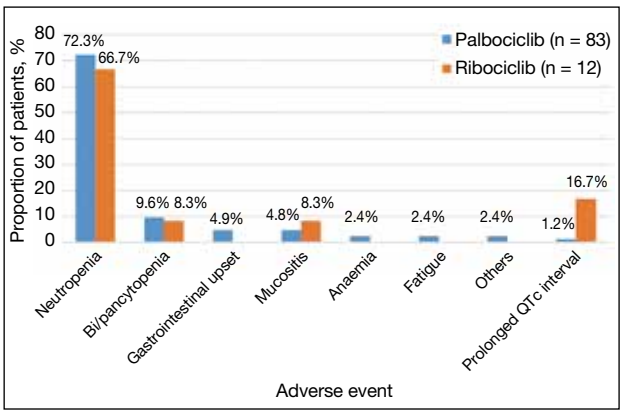

Figure 2. Adverse events necessitating dose reduction.

Patients who received palbociclib or ribociclib as first-line therapy enjoyed longer PFS than those at later lines. Median PFS for first-, second-, and third-line and beyond were 35 months, 20.6 months, and 6.2 months, respectively (Figure 3).

Potential Factors Affecting Treatment Outcome in Patients on First-Line Treatment

Dose reduction, treatment delay (defined by any delay between cycles of ≥ 2 weeks), and high ER and PR levels (with Allred score of 6-8) were each associated with longer PFS, with p values of < 0.001, 0.010, 0.002, and 0.001, respectively. The absence of visceral involvement was not statistically significant (p = 0.352). There was no statistically significant difference in PFS between younger and older age-groups (defined by cut-off at 60 years old), nor between those with ECOG PS scores of 0-1 and 2-3. Subsequent multivariable analysis illustrated that dose reduction and strong PR levels were predictors of longer PFS. ER levels and treatment delay were significant factors in univariate analysis, but such statistical significance was lost upon multivariable analysis. Results are detailed in Table 4 and online supplementary Figure.

Pattern of Dose Reduction on the Treatment Outcome

Amongst the patients started on standard dose regimens who subsequently required dose reductions (n = 95),

Table 3. Patient factors and the grade of neutropenia (n = 211).*

	Grade 0-2 neutropenia (n = 58)	Grade 3-4 neutropenia (n = 153)	p Value
Age, y	61.05 ± 10.54	60.59 ± 11.14	0.787
CDK4/6 inhibitor used			
Palbociclib	51 (87.9%)	136 (88.9%)	
Ribociclib	7 (12.1%)	17 (11.1%)	
Eastern Cooperative Oncology			0.694
Group performance status score			
0	2 (3.4%)	2 (1.3%)	
1	42 (72.4%)	118 (77.1%)	
2	8 (13.8%)	16 (10.5%)	
3	6 (10.3%)	17 (11.1%)	
Presence of bone metastasis			0.291
No	19 (32.8%)	39 (25.5%)	
Yes	39 (67.2%)	114 (74.5%)	
Line of treatment			0.373
First	35 (60.3%)	86 (56.2%)	
Second	7 (12.1%)	31 (20.3%)	
Third	16 (27.6%)	36 (23.5%)	
Prior chemotherapy exposure			0.940
No	25 (43.1%)	74 (48.4%)	
Yes	33 (56.9%)	79 (51.6%)	

Abbreviation: CDK4/6 = cyclin-dependent kinase 4 and 6.
* Data are shown as No. (%) or mean ± standard deviation, unless otherwise specified.

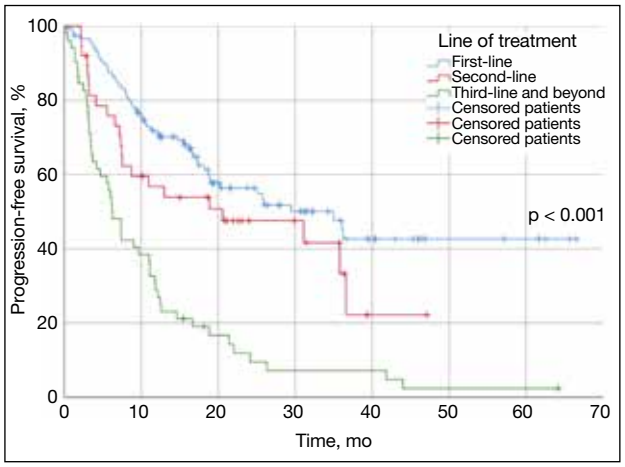

Figure 3. Progression-free survival of patients with different treatment histories.

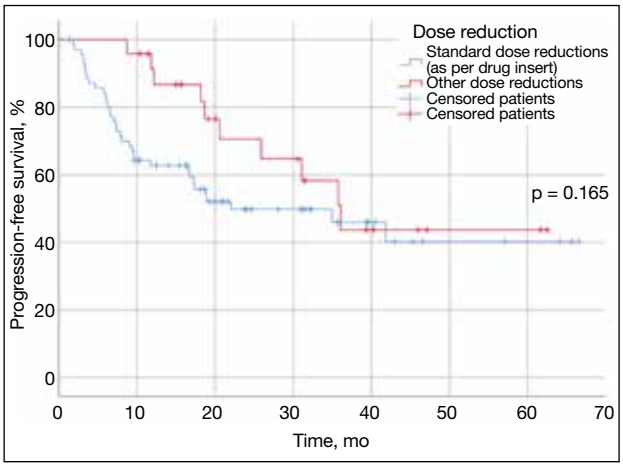

Figure 4. Pattern of dose reduction and treatment outcome shown by progression-free survival in patients on palbociclib or ribociclib who experienced standard dose reductions and other dose reductions.

Table 4. Potential factors affecting treatment outcome in patients on first-line treatment.

	HR (95% CI)	All patients (n = 211)	Patients on palbociclib (n = 104)	Patients on ribociclib (n = 17)
		p Value	p Value	p Value
Dose reduction: no (reference) vs. yes	0.365 (0.209-0.639)	< 0.001	< 0.001	0.277
Treatment delay: no (reference) vs. yes	0.405 (0.204-0.806)	0.010	0.018	0.411
ER level: Allred score 3-5 (reference) vs. 6-8	0.256 (0.107-0.612)	0.002	0.004	0.346
PR level: Allred score 0-5 (reference) vs. 6-8	0.357 (0.198-0.643)	0.001	0.001	0.532
Visceral metastases: present (reference) vs. absent	0.743 (0.397-1.389)	0.352	0.357	0.825
No. of metastatic sites: 0-2 (reference) vs. ≥ 3	1.226 (0.716-2.097)	0.458	0.334	0.750
Age-group: ≤ 60 y (reference) vs. > 60 y	0.949 (0.552-1.631)	0.849	0.734	0.878
ECOG PS: score 0-1 (reference) vs. 2-3	1.167 (0.614-2.218)	0.638	0.971	0.292
Disease status: recurrent disease (reference) vs. *De novo* metastatic disease	0.889 (0.507-1.559)	0.683	0.948	0.304
Starting dose: reduced dose (reference) vs. full dose	2.103 (0.512-8.638)	0.302	0.319	0.721
Multivariable analysis				
Dose reduction: no (reference) vs. yes	0.405 (0.222-0.739)	0.003	0.002	N/A
Treatment delay: no (reference) vs. yes	0.550 (0.262-1.157)	0.115	0.146	N/A
ER level: Allred score 3-5 (reference) vs. 6-8	0.527 (0.211-1.314)	0.169	0.182	N/A
PR level: Allred score 0-5 (reference) vs. 6-8	0.421 (0.228-0.779)	0.006	0.002	N/A

Abbreviations: 95% CI = 95% confidence interval; ECOG = Eastern Cooperative Oncology Group; ER = oestrogen receptor; HR = hazard ratio; N/A = not applicable; PR = progesterone receptor; PS = performance status.

no statistically significant differences in PFS could be observed between those who underwent dose reductions adherent to the FDA drug insert, and those who received dose reductions of other dosing regimens (Figure 4).

DISCUSSION

The treatment landscape of advanced hormone-responsive, HER2-negative breast cancer has transformed dramatically since the emergence of CDK4/6 inhibitors. Palbociclib demonstrated a median PFS of 24.8 and 11.2 months as first- or second-line treatment in PALOMA-2[4] and 3[5] studies, respectively. Ribociclib exhibited consistent PFS advantage in first- and second-line treatment, and in premenopausal women in MONALEESA-2,[6,7] 3,[8] and 7[9] studies (median PFS = 20.5-25.3 months), with updated results revealing a 12.5-month overall survival benefit in first-line therapy.[10] First-line abemaciclib also showed a superior PFS of

28.2 months compared to aromatase inhibitors alone in MONARCH-3 trial.[11,12]

However, Asian patients are often underrepresented in such clinical trials, with only 14.6% and 20% included in PALOMA-2[4] and 3[5] studies, respectively, and 8.4%, 9.3%, and 30% included in MONALESSA-2,[6,7] 3,[8] and 7[9] studies, respectively. There are various cohorts reporting clinical outcomes of CDK4/6 inhibitors around Asia.[17-22] While the recently published PALOMA-4 trial recruited patients from 52 centres across Asia, patients were all of ECOG PS score of 0-1,[21] which was different from the average patients we encounter in our daily clinical practice.

Spanning the dates from July 2016 to February 2022, our study population was predominantly on palbociclib with nearly a quarter of patients not being exposed to CDK4/6 inhibitors unless on third-line therapy or beyond. Such practice was largely influenced by drug availability in our locality. Palbociclib, ribociclib, and abemaciclib were registered in Hong Kong on 2 December 2016,[13] 26 January 2018,[14] and 18 December 2019,[15] respectively. Before their corresponding inclusion into the Hospital Authority Drug Formulary on 14 July 2018,[23] 13 October 2018,[24] and 11 July 2020,[16] patients had to receive such treatment on a named patient basis. The monthly treatment cost of HKD$18,000 to $23,100 precluded its initial accessibility within our public hospital setting, with more widespread use of palbociclib and ribociclib observed since their coverage under the Community Care Fund on 12 January 2019[25] and 13 July 2019,[26] respectively. Abemaciclib was not covered by the Fund till 9 January 2021,[27] and none of our patients in this study received it.

Table 5 displays the median PFS, dose reduction rate, and frequency of toxicities reported in landmark clinical trials and other regional cohorts, compared with our experience. The longer median PFS in first- and second-line treatment in our cohort as compared to those reported in landmark clinical trials could be due to the less unified timing of response assessment in the real-world setting and the relatively short median follow-up time of 12.6 months. While acknowledging that direct comparisons of the PFS with landmark clinical trials are hindered by our heterogeneous patient group, the overall pattern of treatment outcome remains comparable to international standards.

Our dose reduction rates were higher than those of the PALOMA-2 study[4] but similar to those reported in the MONALEESA-2 study[6,7] and other regional Asian cohorts.

Higher rates of grade ≥ 3 haematological toxicities were seen in our cohort than in PALOMA-2 or 3 and MONALEESA-2, 3, or 7 studies, but they were similar to those in PALOMA-4 study and other regional Asian cohorts. This echoes the reports of a higher incidence of grade ≥ 3 neutropenia in Asians, which can be up to 92%.[28] Febrile neutropenia remained low.

Consistent with other international cohorts,[18,19,28-31] dose reduction did not compromise the treatment efficacy.

In a detailed safety analysis of the PALOMA-2 study, Diéras et al[29] conducted a landmark analysis of dose reduction on treatment efficacy at 3, 6, and 9 months in the palbociclib arm. It showed similar PFS in patients who experienced dose reduction and those who did not.[29] Similarly, a pooled safety analysis of MONALEESA-2, 3 and 7 studies showed similar median PFS of 24.8 to 29.6 months across patients on various dose intensities that ranged from ≤ 71% to 100%, which reaffirmed that the PFS, overall response rate, and clinical benefit rate were maintained regardless of dose modifications.[30] One suggestion made by the authors was that variations in drug metabolism and pharmacodynamic effects were present such that patients who experienced more treatment-related AEs, hence requiring dose modifications, were also subjected to enhanced drug exposure leading to an enhanced therapeutic effect.[30] Further studies are warranted to explore the reasons behind this.

Interestingly, we reproduced the same observations noted in a multicentre study from the United Kingdom,[31] in which dose reduction and delays were associated with longer PFS. Owing to the retrospective nature of our study consisting of a relatively small and heterogeneous population, we do not aim to conclude superiority of such dose alterations over the standard dose. Nonetheless, this could be a reassurance that de-escalation of palbociclib or ribociclib dose can be considered in patients when deemed clinically necessary without compromising the treatment outcome.

High PR levels were identified as a statistically significant predictor of longer PFS. High ER levels trended towards statistically significant longer PFS only on univariate but not multivariate analysis. This could be limited by the small number of low–ER level patients (3.3%, n =

Table 5. Published clinical studies on cyclin-dependent kinase 4 and 6 inhibitors for metastatic breast cancer.

	Setting	mPFS, mo	Dose reduction rate	Grade ≥ 3 neutro-penia	Grade ≥ 3 anaemia	Grade ≥ 3 thrombo-cytopenia	Febrile neutro-penia	Fatigue	ALT/AST rise	Diarrhoea
PALOMA-2[4]	1L palbociclib + letrozole	24.8	36%	66.5%	5.4%	1.6%	1.8%	37.4%	ALT: 0.23%	26.1%
PALOMA-3[5]	2L palbociclib + fulvestrant	11.2	N/A	69.6%	4.3%	2.9%	1%	44.1%	AST: 11.6%	27.2%
PALOMA-4[21]	1L palbociclib + letrozole in Asians	21.5	28.6%	84.5%	4.8%	6.5%	2.4%	10.1%	ALT: 33.3% AST: 34.5%	10.7%
Lee et al[17]	Palbociclib + letrozole or fulvestrant in Koreans (1L-3L)	25.6 (letrozole) 6.37 (fulvestrant)	32.1%	85.8%	6.5%	8.3%	N/A	27.2%	N/A	3.6%
Shangguan et al[18]	Palbociclib in Chinese	12.8	27.5%	N/A	N/A	N/A	N/A	N/A	N/A	N/A
Shen et al[19]	Palbociclib in Chinese	1L: 21 2L: 14 3L: 7	11.1%	30%	32.6% (all grades)	22.1% (all grades)	4.2%	48.4%	N/A	7.9%
MONALEESA-2[6,7]	1L ribociclib + letrozole	25.3	53.9%	59.3%	1.2%	N/A (all grades < 15%)	1.5%	36.5%	ALT: 15.6% AST: 15%	35% (Grade 3: 1.2%)
MONALEESA-3[8]	1L/2L ribociclib + fulvestrant	20.5	37.9%	53.4%	3.1%	1%	1%	31.5%	23.6%	29%
MONALESSA-7[9]	1L ribociclib in pre menopausal patients	23.8	35%	61%	3%	1%	2%	22%	ALT: 7% AST: 8%	19%
Low et al[20]	Palbociclib or ribociclib in Singapore (1L-4L)	1L: 28.2 2L: 18.4 3L: 7.7 ≥ 4L: 9.4	48%	N/A	N/A	N/A	2%	1%	N/A	N/A
MONALEESASIA[22]	Ribociclib + letrozole in Asians	ORR: 56.5%	52.2%	73.9%	N/A	N/A	N/A	N/A	17.4%	N/A
MONARCH-3[11]	1L abemaciclib + aromatase inhibitor	28.2	43.4%	21.1%	5.8%	1.9%	0.3%	40.1%	15.6%	81.3%
The current study	Palbociclib and ribociclib	1L: 35 2L: 20.6 ≥ 3L: 6.2	49.2%	72.5%	12.8%	6.2%	3.3%	21.8%	20.4%	16.6%

Abbreviations: 1L = first-line treatment; 2L = second-line treatment; 3L = third-line treatment; 4L = fourth-line treatment; ALT = alanine aminotransferase; AST = aspartate aminotransferase; mPFS = median progression-free survival; N/A = not available; ORR = overall response rate.

7) in our cohort, precluding analysis. Nevertheless, this mirrored with the observation of PR levels—the other surrogate marker for endocrine responsiveness—and resonates with the exploratory analysis results of the PADA-1 trial presented at the European Society for Medical Oncology Breast Cancer Congress 2022.[32] ER and PR immunohistochemistry scores were shown to have significant impact on PFS achieved with first-line palbociclib, with each 10% gain in ER level being associated with a 10% reduced risk of PFS events (hazard ratio = 0.90; p = 0.002), and each 10% gain in PR level being associated with a 8% risk of PFS events (hazard ratio = 0.92; $p < 0.001$).[32] This could be a potential area for future studies, aiming to elucidate whether patients with higher ER and PR levels could benefit from a tailor-made reduced dose while still achieving similar therapeutic effect.

Limitations

Limited by its retrospective nature, our clinical study was inevitably influenced by environmental factors such as the varying availability of the drugs due to time and

cost constraints, deviation from standard dose reduction protocol, and underreporting of non-haematological toxicities leading to minor deviations from international cohorts. Nonetheless, the clinical outcomes and safety profile of palbociclib and ribociclib in our centre largely mirrored that seen in drug registration clinical trials and other regional Asian cohorts.

CONCLUSION

To our knowledge, this is the largest cohort of its kind reported locally in Hong Kong. The treatment outcomes and safety profiles of palbociclib and ribociclib demonstrated in our institution, with a predominantly Asian population with ECOG PS scores ranging from 0 to 3, were comparable to those quoted in international clinical trials and other regional Asian cohorts. Dose reduction could be considered when deemed clinically necessary, in hopes of maximising patients' tolerance to treatment and maintaining patients' quality of life, either upon treatment commencement in perhaps older and frailer patients, or in face of AEs, as it did not compromise the treatment efficacy.

REFERENCES

1. Hong Kong Cancer Registry, Hospital Authority, Hong Kong SAR Government. Leader cancer sites in Hong Kong in 2019. Available from: https://www3.ha.org.hk/cancereg/pdf/top10/rank_2019.pdf. Accessed 11 Dec 2022.
2. Hong Kong Breast Cancer Foundation. Hong Kong Breast Cancer Registry Report No. 12. 2020. Available from: http://www.hkbcf.org/en/our_research/main/519/upload/category/519/self/5f7bdc6663cf9.pdf. Accessed 11 Dec 2022.
3. Gennari A, André F, Barrios CH, Cortés J, de Azambuja E, DeMichele A, et al. ESMO Clinical Practice Guideline for the diagnosis, staging and treatment of patients with metastatic breast cancer. Ann Oncol. 2021;32:1475-95.
4. Finn RS, Martin M, Rugo HS, Jones S, Im SA, Gelmon K, et al. Palbociclib and letrozole in advanced breast cancer. N Engl J Med. 2016;375:1925-36.
5. Turner NC, Slamon DJ, Ro J, Bondarenko I, Im SA, Masuda N, et al. Overall survival with palbociclib and fulvestrant in advanced breast cancer. N Engl J Med. 2018;379:1926-36.
6. Hortobagyi GN, Stemmer SM, Burris HA, Yap YS, Sonke GS, Paluch-Shimon S, et al. Ribociclib as first-line therapy for HR-positive, advanced breast cancer. N Engl J Med. 2016;375:1738-48.
7. Hortobagyi GN, Stemmer SM, Burris HA, Yap YS, Sonke GS, Paluch-Shimon S, et al. Updated results from MONALEESA-2, a phase III trial of first-line ribociclib plus letrozole versus placebo plus letrozole in hormone receptor–positive, HER2-negative advanced breast cancer. Ann Oncol. 2018;29:1541-7.
8. Slamon DJ, Neven P, Chia S, Fasching PA, De Laurentiis M, Im SA, et al. Phase III randomized study of ribociclib and fulvestrant in hormone receptor–positive, human epidermal growth factor receptor 2–negative advanced breast cancer: MONALEESA-3. J Clin Oncol. 2018;36:2465-72.
9. Tripathy D, Im SA, Colleoni M, Franke F, Bardia A, Harbeck N, et al. Ribociclib plus endocrine therapy for premenopausal women with hormone-receptor–positive, advanced breast cancer (MONALEESA-7): a randomised phase 3 trial. Lancet Oncol. 2018;19:904-15.
10. Hortobagyi GN, Stemmer SM, Burris HA, Yap YS, Sonke GS, Hart L, et al. Overall survival with ribociclib plus letrozole in advanced breast cancer. N Engl J Med. 2022;386:942-50.
11. Goetz MP, Toi M, Campone M, Sohn J, Paluch-Shimon S, Huober J, et al. MONARCH 3: abemaciclib as initial therapy for advanced breast cancer. J Clin Oncol. 2017;35:3638-46.
12. Johnston S, Martin M, Di Leo A, Im SA, Awada A, Forrester T, et al. MONARCH 3 final PFS: a randomized study of abemaciclib as initial therapy for advanced breast cancer. NPJ Breast Cancer. 2019;5:5.
13. Drug Office, Department of Health, Hong Kong SAR Government. Drug database—Ibrance capsules 125 mg. Available from: https://www.drugoffice.gov.hk/eps/drug/productDetail2/en/consumer/138597. Accessed 9 Dec 2022.
14. Drug Office, Department of Health, Hong Kong SAR Government. Drug database—Kisqali tablets 200 mg. Available from: https://www.drugoffice.gov.hk/eps/drug/productDetail2/en/consumer/125912. Accessed 9 Dec 2022.
15. Drug Office, Department of Health, Hong Kong SAR Government. Drug database—Verzenio tablets 150 mg. Available from: https://www.drugoffice.gov.hk/eps/drug/productDetail2/en/consumer/124855. Accessed 9 Dec 2022.
16. Hospital Authority, Hong Kong SAR Government. Update of Hospital Authority Drug Formulary - version 16.1. 2020 July 11.
17. Lee J, Park HS, Won HS, Yang JH, Lee HY, Woo IS, et al. Real-world clinical data of palbociclib in Asian metastatic breast cancer patients: experiences from eight institutions. Cancer Res Treat. 2021;53:409-23.
18. Shangguan CF, Jiang M, Yang C, Lou GY, Li YT, Qu Q. Clinical efficacy of palbociclib-based therapy in women with HR+/HER2- metastatic breast cancer in the real-world setting for Chinese women: a comparison with the IRIS study. Eur Rev Med Pharmacol Sci. 2021;25:6138-48.
19. Shen L, Zhou J, Chen Y, Ding J, Wei H, Liu J, et al. Treatment patterns, effectiveness, and patient-reported outcomes of palbociclib therapy in Chinese patients with advanced breast cancer: a multicenter ambispective real-world study. Cancer Med. 2022;11:4157-68.
20. Low JL, Lim E, Bharwani L, Wong A, Wong K, Ow S, et al. Real-world outcomes from use of CDK4/6 inhibitors in the management of advanced/metastatic breast cancer in Asia. Ther Adv Med Oncol. 2022;14:17588359221139678.
21. Xu B, Hu X, Li W, Sun T, Shen K, Wang S, et al. Palbociclib plus letrozole versus placebo plus letrozole in Asian postmenopausal women with oestrogen receptor–positive/human epidermal growth factor receptor 2–negative advanced breast cancer: primary results from PALOMA-4. Eur J Cancer. 2022;175:236-45.
22. Yap YS, Chiu J, Ito Y, Ishikawa T, Aruga T, Kim SJ, et al. Ribociclib, a CDK 4/6 inhibitor, plus endocrine therapy in Asian women with advanced breast cancer. Cancer Sci. 2020;111:3313-26.
23. Hospital Authority, Hong Kong SAR Government. Update of Hospital Authority Drug Formulary - version 14.1. 2018 July 14.
24. Hospital Authority, Hong Kong SAR Government. Update of Hospital Authority Drug Formulary - version 14.2. 2018 October 13.
25. Hospital Authority, Hong Kong SAR Government. Update of Hospital Authority Drug Formulary - version 14.3. 2019 January 12.

26. Hospital Authority, Hong Kong SAR Government. Items supported by the CCF Medical Assistance Programmes. Available from: https://www.ha.org.hk/visitor/ha_visitor_index.asp?content_id=208076. Accessed 15 Feb 2024.
27. Hospital Authority, Hong Kong SAR Government. Update of Hospital Authority Drug Formulary - version 16.3. 2021 January 9.
28. Verma S, Bartlett CH, Schnell P, DeMichele AM, Loi S, Ro J, et al. Palbociclib in combination with fulvestrant in women with hormone receptor–positive/HER2-negative advanced metastatic breast cancer: detailed safety analysis from a multicenter, randomised, placebo-controlled, phase III study (PALOMA-3). Oncologist. 2016;21:1165-75.
29. Diéras V, Harbeck N, Joy AA, Gelmon K, Ettl J, Verma S, et al. Palbociclib with letrozole in postmenopausal women with ER+/HER2- advanced breast cancer: haematologic safety analysis of the randomized PALOMA-2 trial. Oncologist. 2019;24:1514-25.
30. Burris HA, Chan A, Bardia A, Thaddeus Beck J, Sohn J, Neven P, et al. Safety and impact of dose reductions on efficacy in the randomised MONALEESA-2, -3 and -7 trials in hormone receptor–positive, HER2-negative advanced breast cancer. Br J Cancer. 2021;125:679-86.
31. El Badri S, Tahir B, Balachandran K, Bezecny P, Britton F, Davies M, et al. Palbociclib in combination with aromatase inhibitors in patients ≥75 years with oestrogen receptor–positive, human epidermal growth factor receptor 2–negative advanced breast cancer: a real-world multicentre UK study. Breast. 2021;60:199-205.
32. De La Motte Rouge T, Frenel JS, Hardy-Bessard AC, Bachelot T, Pistilli B, Delaloge S, et al. 167MO — Association between ER, PR and HER2 levels and outcome under palbociclib (Pal) + aromatase inhibitors (AIs) as first-line therapy for ER+/HER2- metastatic breast cancer (MBC): an exploratory analysis of the PADA-1 trial. Ann Oncol. 2022;33 Suppl 3:S200.

Hong Kong J Radiol. 2024;27(1):e16-27. Published 20 March 2024 | https://doi.org/10.12809/hkjr2217649

ORIGINAL ARTICLE

CME

Contrast-Enhanced Ultrasound with Perfluorobutane for Hepatocellular Cancer Surveillance: Our Initial Local Experience

YS Chan[1,2], CCM Cho[1,2], TY Yuen[1,2], HY Hung[1,2], PKM Wong[1], MMY Sou[1], SSY Ho[2], GLH Wong[3], WCW Chu[2]

[1]*Department of Imaging and Interventional Radiology, Prince of Wales Hospital, Hong Kong SAR, China*
[2]*Department of Imaging and Interventional Radiology, Faculty of Medicine, The Chinese University of Hong Kong, Hong Kong SAR, China*
[3]*Medical Data Analytic Centre, Department of Medicine and Therapeutics, Faculty of Medicine, The Chinese University of Hong Kong, Hong Kong SAR, China*

ABSTRACT

Introduction: *Ultrasound is the most commonly used modality for hepatocellular cancer (HCC) surveillance in Hong Kong but has limitations in lesion characterisation. A second-generation perfluorobutane (PFB) ultrasound contrast agent allows for lesion characterisation through the usual vascular enhancement phases and provides an additional late Kupffer phase. We reviewed current evidence of PFB use in HCC care and investigated the value of contrast-enhanced ultrasound with PFB (PFB-CEUS) compared with brightness mode (B-mode) ultrasound in surveillance for HCC in high-risk patients in Hong Kong.*

Methods: *This prospective single-centre study assessed 50 high-risk patients under HCC surveillance undergoing B-mode ultrasound and PFB-CEUS, followed by gadoxetic acid–enhanced magnetic resonance imaging (MRI) within 3 weeks of the initial ultrasound scan. The MRI findings were considered the reference standard for the diagnosis of HCC. Detection rates of all and small (≤ 2 cm) HCCs on both modalities and the adverse event rate for each modality were evaluated.*

Results: *The detection rate of small HCCs was 4% by B-mode ultrasound and 6% by PFB-CEUS. A total of four small HCCs were identified in our cohort. The immediate (day 0), short-term (day 7), and long-term (day 90) adverse event rates were 0%, 12% and 6%, respectively. All adverse events were mild and self-limiting, with an uncertain causal relationship to PFB administration.*

Conclusion: *PFB-CEUS is emerging as a useful imaging modality in evaluation of liver lesions and HCC detection. Our initial local experience provides positive agreement with the literature and identifies areas requiring further investigation.*

Key Words: *Carcinoma, hepatocellular; Diagnostic imaging; Liver neoplasms*

Correspondence: *Dr CCM Cho, Department of Imaging and Interventional Radiology, Prince of Wales Hospital, Hong Kong SAR, China*
Email: ccm193@ha.org.hk

Submitted: 11 October 2022; Accepted: 20 March 2023.

Contributors: CCMC, SSYH, GLHW and WCWC designed the study. CCMC, TYY, HYH, PKMW and MMYS acquired the data. YSC and PKMW analysed the data. YSC drafted the manuscript. All authors critically revised the manuscript for important intellectual content. All authors had full access to the data, contributed to the study, approved the final version for publication, and take responsibility for its accuracy and integrity.

Conflicts of Interest: GLHW has served as an advisory committee member for Gilead Sciences and Janssen, as a speaker for Abbot, AbbVie, Bristol Myers Squibb, Echosens, Furui, Gilead Sciences, Janssen and Roche, and received research grant from Gilead Sciences. As an editor of the journal, WCWC was not involved in the peer review process. Other authors have disclosed no conflicts of interest.

Funding/Support: This research received no specific grant from any funding agency in the public, commercial, or not-for-profit sectors.

Data Availability: All data generated or analysed during the present study are available from the corresponding author on reasonable request.

Ethics Approval: The research was approved by the Joint Chinese University of Hong Kong–New Territories East Cluster Clinical Research Ethics Committee (Ref No.: 2018.542) and was conducted in accordance with the Declaration of Helsinki and the International Conference on Harmonisation Good Clinical Practice. All patients gave informed consent for all treatments and procedures, and consent for publication.

中文摘要

以全氟丁烷對比增強超聲波監測肝細胞癌：我們的初步本地經驗

陳奕璇、曹子文、袁子祐、洪曉義、王嘉文、蘇妙怡、何倩儀、黃麗虹、朱昭穎

引言：超聲波是香港最常使用的肝細胞癌監測方式，但在病變定性方面有其局限性。第二代全氟丁烷超聲波造影劑可通過通常的血管增強期來表徵病變，且提供額外的更晚的Kupffer期。我們回顧了目前全氟丁烷在肝細胞癌臨床處理的證據，並調查全氟丁烷對比增強超聲波與亮度模式（B模式）超聲波在監測本港肝細胞癌高風險患者方面的價值。

方法：本前瞻性單一中心研究評估了50名接受肝細胞癌監測的高風險患者，他們接受了B模式超聲波和全氟丁烷對比增強超聲波掃描，隨後在初次超聲波掃描後3週內進行了釓塞酸增強磁力共振。磁力共振結果是診斷肝細胞癌的參考標準。我們評估了兩種模式下所有肝細胞癌和小肝細胞癌（≤ 2厘米）的檢出率以及不良事件發生率。

結果：B模式超聲波的小肝細胞癌檢出率為4%，全氟丁烷對比增強超聲波則為6%。我們的隊列中總共發現四宗小肝細胞癌。即時（第0天）、短期（第7天）和長期（第90天）不良事件發生率分別為0%、12%和6%。所有不良事件均為輕微且具有自限性，與全氟丁烷給藥之間的因果關係不確定。

結論：全氟丁烷對比增強超聲波正成為評估肝臟病變和肝細胞癌檢測的一種有用影像手段。我們最初的本地經驗與文獻一致，並確定了需要進一步研究的方向。

INTRODUCTION

According to the Hong Kong Cancer Registry, hepatocellular carcinoma (HCC) is currently the fifth leading cancer and third leading cause of cancer deaths in Hong Kong despite the declining incidence of hepatitis B infection in recent years.[1] Chronic hepatitis B infection has an established association with, and is the major cause of, HCC. The latest territory-wide study performed in 2015 to 2016 showed a prevalence of 7.8% for hepatitis B infection in Hong Kong.[2] Many individuals with known infection are in imaging surveillance programmes, mostly using ultrasound as a screening tool.

Ultrasound is a relatively simple, radiation-free, widely available, low-cost imaging procedure with good patient acceptance. Ultrasound alone, however, is of limited sensitivity and is inadequate for an imaging diagnosis of HCC, which relies on the characteristic enhancement pattern of the lesion.[3]

Basis of Ultrasound Contrast Agents and Technique of Contrast-Enhanced Ultrasound

The use of contrast-enhanced ultrasound dates back to 1969, when agitated normal saline was used in echocardiography, progressing to the wider application of manufactured microbubbles in the 2000s to image different organs. Microbubbles are formed from an inert gas protected by an outer shell and are smaller than red blood cells. After intravenous injection, they can pass through the pulmonary capillaries and enter the systemic circulation. Being mainly extracellular blood pool agents, they stay in the vasculature, unlike iodinated contrast for computed tomography (CT) which is a soluble agent that will pass through vessel walls and can enter hepatocytes and the nephron. Both are able to provide information about the vascular pattern of the lesion of concern. The mechanism of action is that microbubbles increase the backscatter of ultrasound signal. They oscillate under ultrasound and the non-linear oscillations can cause harmonic emissions. These signals can be captured and processed to produce images with enhanced differentiation between vascular structures (with microbubbles within) and adjacent soft tissue.[4]

Currently, second-generation ultrasound contrast agents (UCAs) are in use worldwide. Commonly known second-generation UCAs include sulphur hexafluoride, which is used in Hong Kong, and perfluorobutane (PFB) which has been licensed in multiple countries for liver-specific imaging. Sonazoid (GE Healthcare, Milwaukee [WI], US) essentially contains PFB microbubbles

stabilised with a lipid coating with a well-defined diameter of approximately 3 μm. Sonazoid to be used in imaging is prepared by reconstitution with 2-mL sterile water for injection. The usual recommended dose was 0.015 mL/kg. In addition to the standard vascular phases including arterial, portal venous and delayed phases, PFB has the unique ability to be taken up by the Kupffer cells. This enables Kupffer phase imaging which resembles the imaging obtained with a nuclear hepatobiliary scan. The microbubbles can stay in the Kupffer cells for up to a few hours. This aids in lesion detection and characterisation. During the Kupffer phase, the liver parenchyma should normally be uniformly enhancing; the presence of defects would indicate lesions devoid of Kupffer cells, allowing otherwise subtle lesions, in particular, lesions that may be isoechoic on brightness mode (B-mode) ultrasound, to become visible. Most malignancies, hepatic or metastatic, do not contain Kupffer cells, whereas benign entities such as focal nodular hyperplasia do contain such cells. This is comparable with using a liver-specific contrast agent such as gadoxetic acid in magnetic resonance imaging (MRI) for hepatobiliary phase imaging. Leveraging this unique property of PFB, an imaging technique called defect reperfusion imaging was developed, using an additional contrast bolus injection for evaluation of the vascular characteristics of a defect in the Kupffer phase, further improving its diagnostic value.[5]

The time frames for the phases are as follows (assuming a normal cardiac output): the arterial phase starts at 10 seconds, peaks at 30 to 50 seconds, and is sustained until approximately 1 minute; the portovenous phase starts at 30 seconds, peaks at 80 to 90 seconds, and is sustained until approximately 2 minutes; the late vascular phase then ensues and is followed by the Kupffer phase (also called the post-vascular phase), which starts at approximately 10 minutes.[6]

Perfluorobutane Applications

In 2008, the superiority of contrast-enhanced ultrasound with PFB (PFB-CEUS) versus unenhanced ultrasound in the diagnosis of focal liver lesions was confirmed by a phase III clinical trial by Miyamoto et al.[7] One study reported an even higher sensitivity and accuracy for PFB-CEUS than contrast-enhanced CT in detecting hepatic malignancy.[8] CEUS has value for lesions that are indeterminate on CT or MRI due to its heightened sensitivity in detecting vascular enhancement and real-time continuous evaluation of the enhancement pattern.[9] Compared with the other widely applied second-generation UCAs, several studies have confirmed the non-inferiority of PFB.[10,11] A retrospective study published in 2010 by Kan et al[12] found a high sensitivity and specificity for detection of small (≤ 2 cm) HCCs with additional tumours detected by PFB-CEUS compared with contrast-enhanced CT.

Beyond aiding initial imaging diagnosis, PFB has been found to increase the localisation rate of focal hepatic lesions for percutaneous biopsy.[13,14] Along the same lines, lesion localisation for radiofrequency ablation can also be improved, with a higher success rate and fewer treatment sessions required.[15-17]

Several studies have explored the utility of PFB in prediction of treatment response of HCC treated with transarterial chemoembolisation and other targeted therapies, using a reduction in lesion vascularity in an early post-intervention scan to predict the outcome.[18-21] In 2021, Funaoka et al[22] published their retrospective study testing the ability of PFB to evaluate the efficacy of radiotherapy for HCC, which further expands the potential indications of PFB-CEUS as the results were encouraging.

Standardisation and Regulation

With the increasing recognition of PFB's utility, a consensus statement with guidelines for PFB's use was released in 2020 by the Asian Federation of Societies for Ultrasound in Medicine and Biology.[6] In the same year, the World Federation for Ultrasound in Medicine and Biology also published a good practice recommendation.[9] Part of the reporting standardisation of liver imaging is reliant on the use of the Liver Reporting and Data System (LI-RADS). The current version of LI-RADS, however, only applies to CEUS performed with sulphur hexafluoride microbubbles (SonoVue) and lipid-coated perfluoropropane microbubbles (Definity). An early study of a modified CEUS LI-RADS for PFB showed the LI-RADS categories LR-5 and LR-M to be good predictors of HCC and non-HCC malignancies.[23] A recent study also found no statistically significant difference between modified CEUS LI-RADS, CT, and the 2018 version of MRI LI-RADS in 31 histologically proven lesions.[24] Further inclusion of PFB is to be expected in the next version of CEUS LI-RADS, which can provide formal recognition of its value in HCC imaging.[25]

Safety Consideration

PFB has an established low-risk profile. The incidence of adverse events was quoted to be 0.5% to 11.4%.[6,26,27]

No serious adverse events have been reported to date.[6] Common adverse effects include diarrhoea, proteinuria, and headache.[6] The overwhelming majority of these reported events did not require treatment.[6,26,27] Urticaria has been reported as an adverse effect. It must be noted that despite the lack of reported cases, anaphylaxis is a possible risk for any injectable agent. The most likely culprit for this potential allergic reaction is the lipid shell of PFB, which is derived from eggs. Therefore, egg allergy is the one and only contraindication to PFB use. Patients with renal insufficiency, or iodine or gadolinium contrast allergy, can undergo PFB-CEUS.

Initial Local Experience

As PFB is an unregistered drug in Hong Kong, it is not currently in widespread use. We performed a pilot study to investigate the value of PFB-CEUS compared with conventional B-mode ultrasound for surveillance detection of HCC in high-risk patients.

METHODS

Design and Setting

This was a prospective, single-centre, single-arm study performed in Prince of Wales Hospital, a tertiary referral centre with hepatology and hepatobiliary surgery services available. The STARD (Standards for Reporting of Diagnostic Accuracy Studies) 2015 guidelines were used for reporting our results.

Patient Recruitment

Patients were recruited by convenience sampling through clinician referral. A total of 50 patients were recruited from the period 1 June 2020 to 3 May 2021. The inclusion and exclusion criteria are listed in Table 1.

Table 1. Inclusion and exclusion criteria for the study cohort.

Inclusion criteria	- Age ≥ 18 y - Known chronic liver disease with or without liver cirrhosis - Nodular liver parenchyma on ultrasonography - LSM-HCC score ≥ 11 in chronic hepatitis B patients[11] - LSM ≥ 12.0 kPa in other chronic liver diseases[2] - Informed written consent obtained
Exclusion criteria	- Child-Pugh score ≥ 8 - Previous or current HCC patients - Previous liver surgery - Liver transplantation - Contraindications to transient elastography (e.g., pregnancy, previous pacemaker implantation) - Contraindications to perfluorobutane contrast - Contraindications to gadoxetic acid contrast - Contraindications to magnetic resonance imaging (e.g., metallic implants, pacemaker implantation) - Refusal to consent

Abbreviations: HCC = hepatocellular carcinoma; LSM = liver stiffness measurement.

Imaging Workflow and Image Interpretation

Eligible patients were assessed via a standard workflow, starting with B-mode ultrasound and PFB-CEUS of the liver performed with the same settings, followed by MRI with gadoxetic acid (Primovist; Bayer Schering Pharma, Berlin, Germany) within 3 weeks of the initial ultrasound scan (Figure 1). The B-mode ultrasound and PFB-CEUS were performed by two registered sonographers who have > 20 years of ultrasound experience, following standard technical specifications (Tables 2 and 3). Standard protocol was also implemented for the gadoxetic acid–enhanced MRI (Table 4). The assessors were not blinded to clinical information of patients or past radiological investigations.

The findings of B-mode ultrasound, PFB-CEUS, and MRI were interpreted and reported separately by three radiologists who had > 5 years of experience in hepatobiliary imaging. As there were no standardised interpretation criteria for B-mode or PFB-CEUS in the diagnosis of HCC, interpretation of the findings from these two scans were based on a 3-point Likert scale (Table 5), while MRI findings were interpreted based on the 2018 version of LI-RADS.[28] The radiologists interpreting MRI were blinded to the results of ultrasound and vice versa. Any equivocal MRI findings were resolved by consensus between two radiologists subspecialising in hepatobiliary radiology. Those with negative findings on both PFB-CEUS and MRI, meaning no focal lesion or focal lesion(s) with low probability of HCC, followed the standard surveillance programme. Patients with intermediate probability for HCC were managed at the discretion of the referring team and underwent closer interval follow-up imaging or biopsy. Patients diagnosed with HCC were referred to the Joint Hepatoma Clinic of Prince of Wales Hospital for further management.

Reference Standards

For patients undergoing hepatic surgery or biopsy, the final diagnosis was based on histological findings. For those who did not undergo surgery or biopsy, the diagnosis of HCC was based on MRI features fulfilling the LR-5 or LR-4 category of the 2018 version of LI-RADS.[28] They were managed in a similar manner in our clinical practice. For LR-3 lesions, which were not biopsied, additional follow-up CT or MRI was performed at the discretion of the referring clinical team.

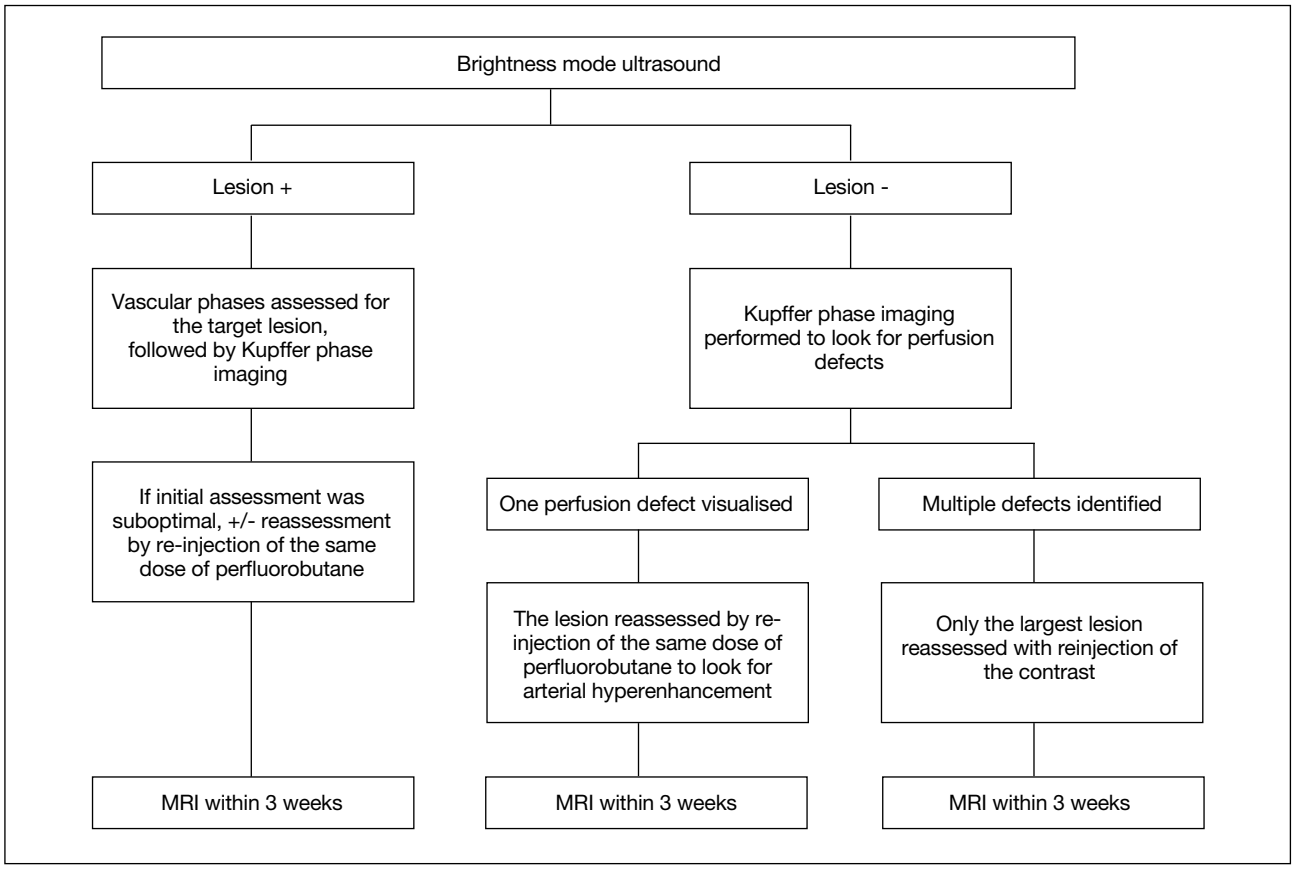

Figure 1. Imaging workflow for the study cohort.
Abbreviation: MRI = magnetic resonance imaging.

Table 2. Technical specifications of brightness mode ultrasound.

Transducer	8-1 MHz curvilinear transducer of Canon Aplio i800 ultrasound system (Toshiba, Otawara, Japan)
Scanning approaches	Supine - Subcostal - Intercostal - Coronal Left lateral decubitus (supplementary) Left posterior oblique (supplementary)
Coverage	Entire liver
Brightness mode imaging	Liver size, parenchymal echotexture, surface, and any focal liver lesion
Colour Doppler imaging	Evaluation of patency of portal veins Evaluation of intralesional vascularity if focal liver lesion is detected

Table 3. Technical specifications of contrast-enhanced ultrasound with perfluorobutane.

Intravenous access	Antecubital or forearm vein
Contrast preparation	16 μg of perfluorobutane suspended in 2 mL of sterile water
Injection dose	0.015 mL/kg body weight
Injection method	Bolus with 10 mL saline flush
CEUS setting	
Scanning view	Dual view (brightness mode + contrast mode)
Mechanical index	0.20-0.26
Dynamic range	60-65 dB
Location of beam focus	Posterior margin of liver
Vascular phases	(after injection)
Arterial phase	10-20 seconds
Portal phase	30-45 seconds
Late phase	> 120 seconds
Post-vascular/Kupffer phase	10-15 minutes after contrast injection

Abbreviation: CEUS = contrast-enhanced ultrasound.

Primary Endpoints

The primary endpoints were the detection rate of small (≤ 2 cm) HCCs on B-mode US and PFB-CEUS. The detection rate was defined as the percentage of positive findings on the respective imaging modality confirmed with a reference standard out of all patients in the study cohort. A positive finding was defined as a high-risk lesion on the Likert scale.

Table 4. Imaging protocol for magnetic resonance imaging with gadoxetic acid.

MRI scanner	3T scanner (Achieva; Philips Medical Systems, Eindhoven, the Netherlands)
Coil	Phase-array body coil
Sequences	
Pre-contrast T1W	Dual-echo axial T1W out-/in-phase gradient-echo images (TR/TE: 122/1.15 ms and 2.3 ms; FA: 70°)
T2W*	Respiratory-triggered single-shot T2W fast spin-echo 4-mm axial images with driven equilibrium (TR/TE: 838 ms/70 ms)
DWI*	DWI 5-mm axial images with b factors 0, 300 and 600
Multiphasic dynamic study	Three-dimensional axial T1W gradient-echo (TR/TE: 3.4 ms/1.7 ms; FA: 10°; matrix size: 211 × 172; field of view: 400 mm; No. of excitations: 1; slice thickness/gap: 4 mm/-2 mm; transverse slices: 100; for fat saturation: spectral pre-saturation with inversion recovery; parallel imaging factor: 3; scan time: 15.4 seconds)
Hepatobiliary phase imaging	T1W images with fat suppression
Contrast injection	Intravenous bolus injection of 25 μmol/kg (0.1 mL/kg) of gadoxetic acid (Primovist; Bayer Schering Pharma, Berlin, Germany) by means of a power injector at a rate of 1 mL/s, followed by 20 mL of saline chaser at the same rate during breath holding
Vascular phases	(after injection)
Arterial	30 seconds
Portal	70 seconds
Delayed	110 seconds
Late delayed	190 seconds
Hepatobiliary phase imaging	20 minutes

Abbreviations: DWI = diffusion-weighted imaging; FA = flip angle; MRI = magnetic resonance imaging; T1W = T1-weighted; T2W = T2-weighted; TE = echo time; TR = repetition time.
* Performed during the 20-minute time gap before hepatobiliary phase imaging.

Table 5. Interpretation criteria for brightness mode ultrasound and perfluorobutane-enhanced ultrasound.

Risk of HCC	Brightness mode ultrasound	Perfluorobutane-enhanced ultrasound
Low	Ill-defined lesion with barely visible margin No or minimal vascularity	Isoenhancement with surrounding liver parenchyma in all vascular phases
Intermediate	Relatively well-defined lesion with discernible margin No or variable intralesional vascularity	Weak hyperenhancement in arterial phase No or mild washout in late vascular or Kupffer phase
High	Well-defined lesion with discernible or irregular margin Apparent/chaotic intralesional vascularity	Hyperenhancement in arterial phase with washout in vascular phase or washout in Kupffer phase

Abbreviation: HCC = hepatocellular cancer.

Secondary Endpoints

The secondary endpoints included the detection rate of all sizes of HCC and immediate (day 0), short-term (day 7) and long-term (day 90) adverse event rates. Adverse events were recorded according to the CTCAE (Common Terminology Criteria for Adverse Events) version 5.0 with structured telephone interviews at 1 week and 90 days after the ultrasound examination.[29]

RESULTS

A total of 50 patients were included in the study, consisting of 32 men and 18 women with a mean age of 62.6 years (Table 6). The majority (72%) of the patients were in the HCC surveillance programme due to hepatitis B. All of the patients had had prior surveillance imaging. For 94% of the patients, the previous surveillance scans were B-mode ultrasound while the rest were contrast-enhanced CT. The median time from prior surveillance imaging to ultrasound evaluation our study was 12.5 months. The median time from PFB-CEUS to MRI was 11 days. None of the detected lesions underwent biopsy or surgical resection during the study period.

Primary Endpoints

The detection rates of small HCCs were 4% (n = 2) by B-mode ultrasound and 6% (n = 3) by PFB-CEUS. A

total of four small HCCs were identified in our cohort (Table 7). Figures 2 to 5 show the key imaging features of these four HCCs found in our cohort.

Secondary Endpoints

There was no HCC > 2 cm identified in the study cohort. The immediate adverse event rate was 0%, the short-term adverse event rate was 12% (n = 6), and the long-term adverse event rate was 6% (n = 3) [Table 8]. All of the adverse events were mild and self-limiting, with an uncertain causal relationship to PFB administration.

DISCUSSION

In our study, PFB-CEUS had a slightly better detection rate of HCC than B-mode ultrasound. Although all of the HCCs were detectable by either modality, B-mode ultrasound falsely classified two of the lesions as intermediate risk on the Likert scale, while PFB-CEUS was able to add value by reclassifying one of these lesions underclassified by B-mode ultrasound as a high-risk lesion. This finding is in keeping with that of Park et al,[30] though no statistical significance was identified in their study for the detection of additional small HCCs by PFB-CEUS.

With this initial trial of PFB application, we have learned a few lessons in its use. First of all, deep lesions are difficult to evaluate by PFB-CEUS. The one false-negative lesion on PFB-CEUS was a lesion located deep in the parenchyma, 9 cm from the skin surface (Figure 3). The difficulty of evaluating deep lesions by PFB-CEUS was recognised due to ultrasound attenuation in low mechanical index settings.[6] Although switching to high mechanical index settings in B-mode ultrasound can aid assessment, the limited assessment by PFB-CEUS precludes its value addition in deep lesion characterisation.

In addition to the technical aspect of PFB use, we made an observation of a unique property. One of the LR-4 lesions was identified in the Kupffer phase as a defect on PFB-CEUS, while showing hyperintensity on the hepatobiliary phase in gadoxetic acid–enhanced MRI. This evokes a complex discussion involving both PFB, liver-specific MRI contrast properties and HCC cell biology. PFB-CEUS has often been compared with gadoxetic acid–enhanced MRI for its characteristic liver-specific phase—the Kupffer phase. The two phases share similarities by predominantly identifying HCC as focal defects, but have fundamentally different principles underlying them. For gadoxetic acid–enhanced MRI, the hepatobiliary phase appearance is based upon the organic anion transporting polypeptide 8 (*OATP8*)

Table 6. Patient demographics (n = 50).*

Sex	
Male	32 (64%)
Female	18 (36%)
Mean age, y (range)†	62.6 (41-86)
Body mass index	18.3-49.5
Albumin level, g/L	24-47
Bilirubin level, μmol/L	5-45
Alpha fetoprotein level, μg/mL	1-12
Cause of surveillance	
Hepatitis B	36 (72%)
Hepatitis C	3 (6%)
Hepatitis B and alcoholic cirrhosis	2 (4%)
Autoimmune hepatitis	6 (12%)
Hepatitis B and autoimmune hepatitis	1 (2%)
Primary biliary cholangitis	1 (2%)
Cryptogenic cirrhosis	1 (2%)
Current antiviral treatment	
Yes	38 (76%)
No	12 (24%)
Child-Pugh class	
A	10 (20%)
B	6 (12%)
C	2 (4%)
Unclassified	32 (64%)

* Data are shown as No. (%) or range, unless otherwise specified.
† Mean age of male: 61.7; mean age of female: 64.1.

Table 7. Characteristics of hepatocellular cancer detected in the study cohort.

Case No.		Cause of surveillance	Location	Size, mm	Likert scale on B-mode US	Likert scale on PFB-CEUS	MRI LI-RADS	Management	Figure
3	Lesion 1	Primary biliary cholangitis	S6	13	Intermediate	High	5	MWA	2
12	Lesion 1	Hepatitis B	S5	19	High	High	4	Palliative care	3
23		Hepatitis B	S8	10	Intermediate	Intermediate	4	MWA	4
40		Hepatitis B	S3	16	High	High	4	Palliative care	5

Abbreviations: B-mode US = brightness mode ultrasound; LI-RADS = Liver Reporting and Data System; MRI = magnetic resonance imaging; MWA = microwave ablation; PFB-CEUS = contrast-enhanced ultrasound with perfluorobutane; S3 = segment 3; S5 = segment 5; S6 = segment 6; S8 = segment 8.

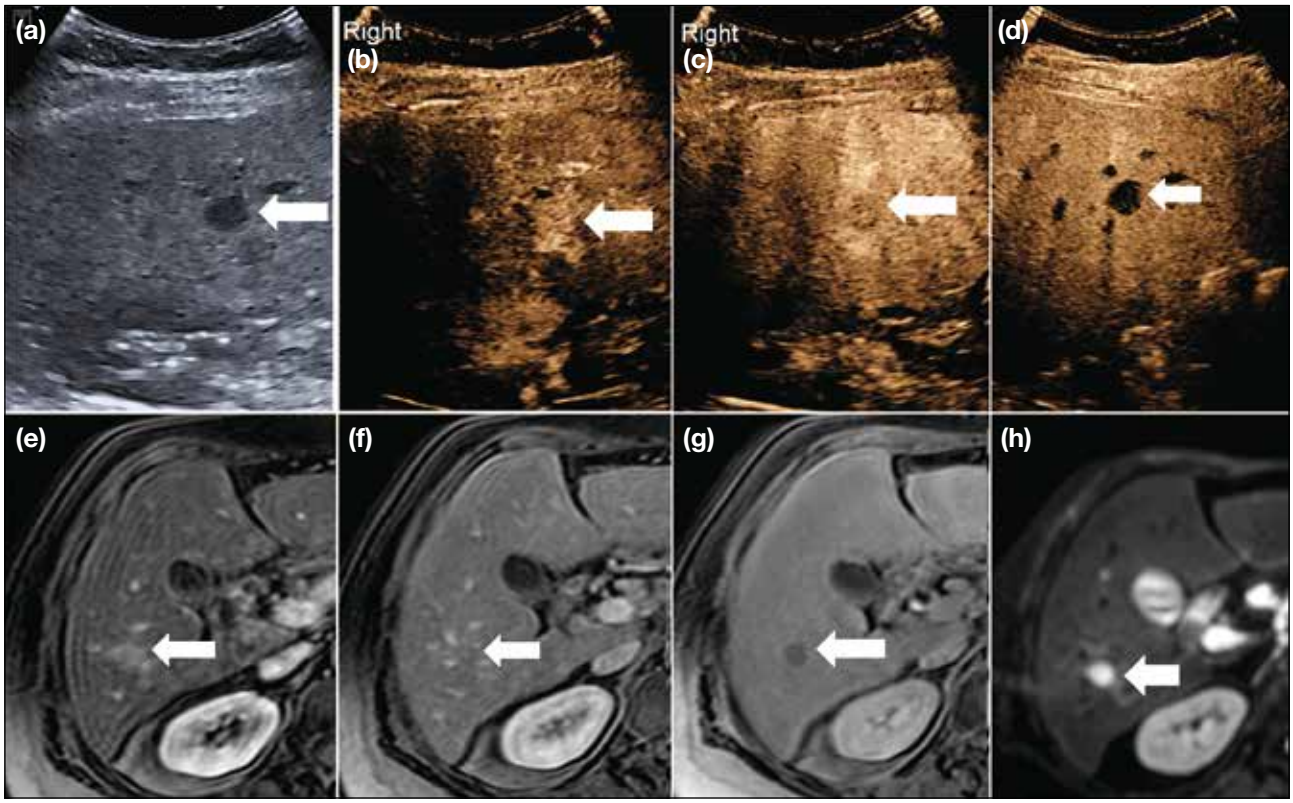

Figure 2. A hepatocellular carcinoma (arrows) in a patient with underlying primary biliary cholangitis. (a) Brightness mode ultrasound showing a well-defined round hypoechoic lesion. Perfluorobutane-enhanced ultrasound images in (b) arterial, (c) portovenous, and (d) Kupffer phases showing the lesion to be arterial hyperenhancing in the arterial phase, with portovenous washout and a Kupffer phase defect. T1-weighted fat-saturated axial gadoxetic acid–enhanced magnetic resonance imaging images in (e) arterial and (f) portovenous phases showing corresponding enhancing pattern. (g) Hepatobiliary phase image showing corresponding focal defect. (h) Diffusion-weighted imaging (DWI) image showing high DWI value, with corresponding low apparent diffusion coefficient value (not shown) in keeping with restricted diffusion.

expression of cells. Normal hepatocytes take up contrast through *OATP*, while both early and progressed HCCs often have a reduced expression of *OATP* during hepatocarcinogenesis, reducing their contrast uptake in the hepatobiliary phase, leading to a hepatobiliary phase defect.[31] Hepatobiliary phase–hyperintense HCC is, however, not uncommon, constituting up to 10% of cases.[32] It has been suggested that hepatobiliary phase hyperintensity may be seen in some moderately- or well-differentiated HCCs, but has been reported in poorly differentiated HCC as well and is due to paradoxical upregulation of *OATP*.[33] On the other hand, for PFB-CEUS, the contrast between normal parenchyma and HCC is achieved by differences in the number of Kupffer cells. Kupffer cells are liver-specific macrophages, which phagocytose the microbubbles, causing enhancement of hepatic parenchyma. The Kupffer cell count is seen to decline with hepatocarcinogenesis and has been suggested to decline more slowly than *OATP8* expression.[32] The presence of a Kupffer phase defect strongly suggests progression of HCC. Korenaga et al[34] found that all the moderately and poorly differentiated HCCs in their study showed Kupffer phase defects while well-differentiated HCCs tended to lack them. Our LR-4 lesion did not undergo histological confirmation, but we speculated that it is a moderately differentiated HCC based on the uptake. Further studies are warranted to look into the potential use of PFB-CEUS versus gadoxetic acid–enhanced MRI for predicting the histological differentiation of HCC.

We have also identified a potential advantage of using PFB-CEUS, which is in patients with hepatic iron overload. One of the patients was found to have heavy iron deposition on MRI. This markedly impaired the assessment on hepatobiliary phase as the whole

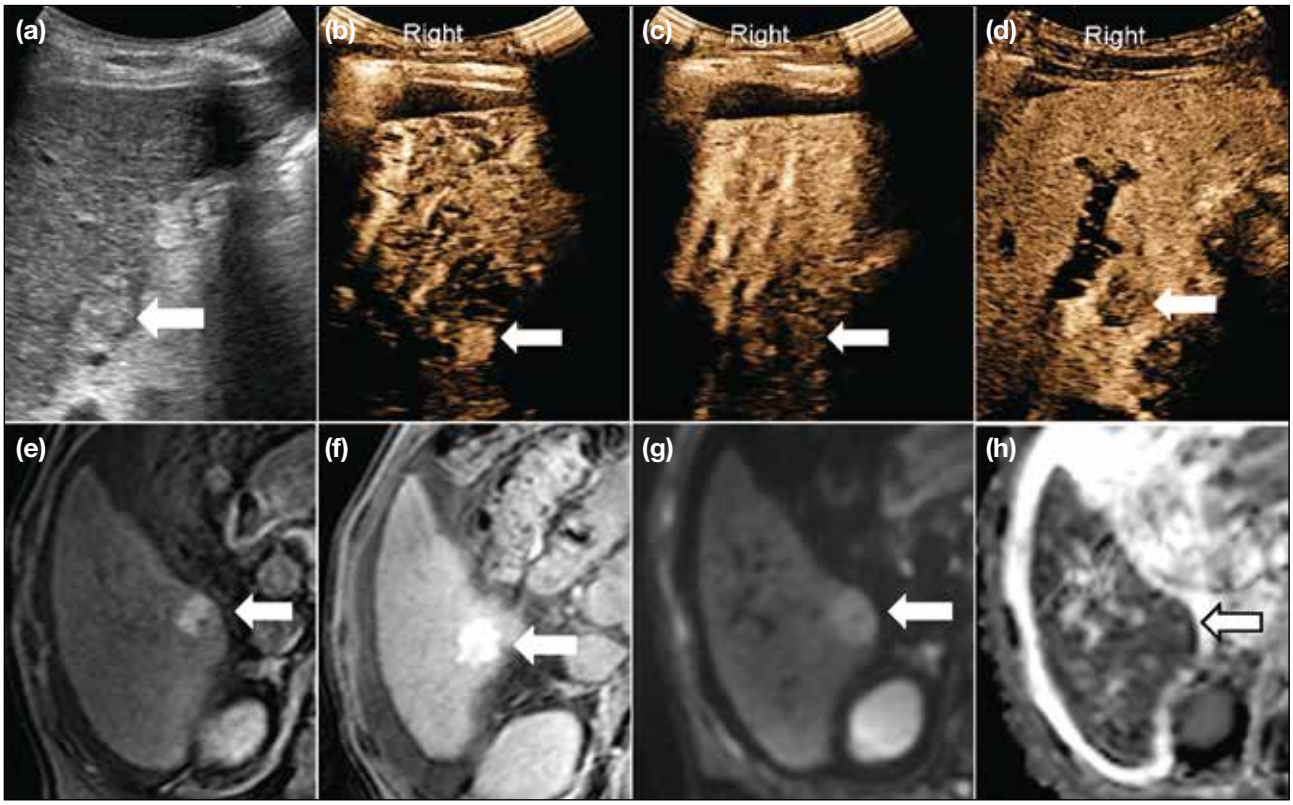

Figure 3. A hepatocellular carcinoma (arrows) in a patient with chronic hepatitis B infection. (a) Brightness mode ultrasound identified a well-defined hyperechoic lesion. Perfluorobutane-enhanced ultrasound in (b) arterial, (c) portovenous, and (d) Kupffer phases identified characteristic pattern of arterial hyperenhancement, portovenous washout with a Kupffer phase defect. (e) T1-weighted fat-saturated axial gadoxetic acid–enhanced magnetic resonance imaging image showing arterial hyperenhancement of the lesion. (f) Hepatobiliary phase image showing hepatobiliary phase uptake of the lesion. (g) Diffusion-weighted image and (h) apparent diffusion coefficient map confirmed restricted diffusion in the lesion.

liver remained hypointense due to iron deposition. Iron overload is a recognised risk factor for HCC development. Due to the paramagnetic effect of iron, iron-overloaded liver parenchyma shows markedly hypointense signal on T1-weighted and T2-weighted images, providing excellent contrast for iron-sparing HCC. It should be noted, however, that siderotic nodules may also be found in such patients. Siderotic nodules are hypointense, making them inconspicuous due to a similar hypointense appearance to the surrounding liver tissue which is also iron-overloaded. With the similar liver-specific nature of PFB and liver-specific MRI contrast, we pondered the possibility of the superiority of use of PFB-CEUS in iron-overloaded liver in demonstrating a liver-specific phase defect. Up to now, the effect of hepatic iron overload on Kupffer cell function and Kupffer phase defects for HCC detection has not been described. Our study has identified a unique area in PFB-CEUS use that has not been previously described, and further investigation into the use of PFB-CEUS Kupffer phase imaging as an alternative screening method for patients with hepatic iron overload should be carried out. This also brings out the possibility of using PFB-CEUS in other conditions where the hepatobiliary phase assessment on MRI is limited, e.g., patients with poor hepatic function, severe cirrhosis, or cholestasis.[30]

Limitation

The main limitation of our study is the small sample size and low incidence of HCC in our cohort, which limits the potential for statistical evaluation. This study framework served more as a standardised approach to our initial experience with PFB use in HCC surveillance. Despite the small size, we were able to identify a few points in the use of PFB that require further development and found additional value of PFB use that is in keeping with

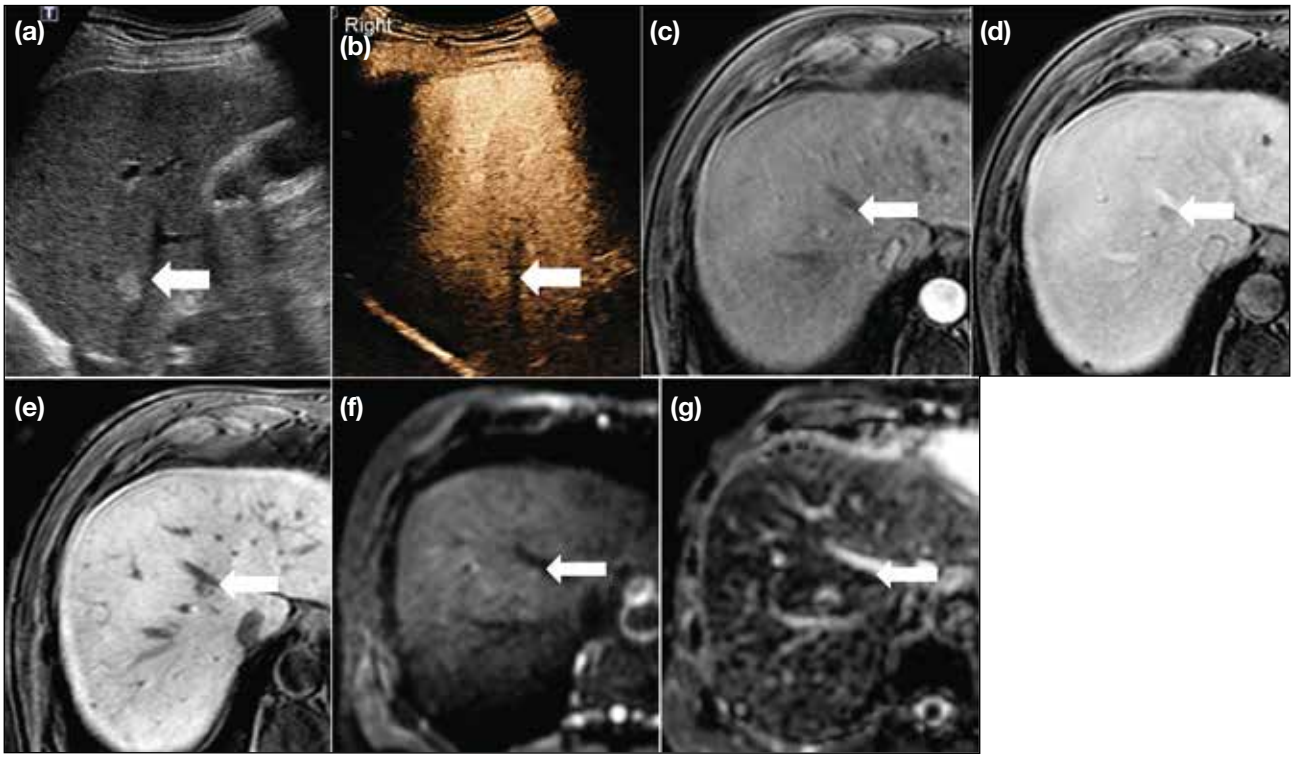

Figure 4. A hepatocellular carcinoma (HCC) [arrows] in a patient with hepatitis B. The HCC was seen as a deep-seated well-defined hyperechoic lesion on brightness mode ultrasound (a), with subtle corresponding arterial hyperenhancement on perfluorobutane-enhanced ultrasound (b). The deep-seated location rendered assessment difficult in subsequent phases. T1-weighted fat-saturated gadoxetic acid–enhanced magnetic resonance imaging image in arterial phase (c) did not reveal any abnormal enhancement, but a focal lesion abutting the middle hepatic vein was seen to washout on portovenous phase (d), with corresponding defect on hepatobiliary phase (e). Faint restricted diffusion was evident with focal hyperintensity at the corresponding site diffusion-weighted imaging MRI on (f) and hypointensity on apparent diffusion coefficient image (g).

findings in the literature. Further studies with a larger sample size may be attempted to allow for statistical evaluation of this slowly maturing modality of choice.

CONCLUSION

PFB-CEUS is an emerging imaging modality in evaluation of liver lesions and HCC detection, with increased recognition worldwide and expanding potential uses. Our initial local experience provides positive agreement with the literature and identified areas requiring further investigation, including correlation of Kupffer phase defects and hepatobiliary phase defects with histological differentiation, and potential use of the Kupffer phase in assessment of patients with iron-overloaded livers.

REFERENCES

1. Hospital Authority. Overview of Hong Kong Cancer Statistics of 2019. 2021. Available from: https://www3.ha.org.hk/cancereg/pdf/overview/Overview%20of%20HK%20Cancer%20Stat%202019.pdf. Accessed 27 Feb 2024.
2. Liu KS, Seto WK, Lau EH, Wong DK, Lam YF, Cheung KS, et al. A territorywide prevalence study on blood-borne and enteric viral hepatitis in Hong Kong. J Infect Dis. 2019;219:1924-33.
3. Chou R, Cuevas C, Fu R, Devine B, Wasson N, Ginsburg A, et al. Imaging techniques for the diagnosis of hepatocellular carcinoma: a systematic review and meta-analysis. Ann Intern Med. 2015;162:697-711.
4. Baun J. Contrast-enhanced ultrasound: a technology primer. J Diagn Med Sonogr. 2017;33:446-52.
5. Kudo M, Hatanaka K, Maekawa K. Newly developed novel ultrasound technique, defect reperfusion ultrasound imaging, using Sonazoid in the management of hepatocellular carcinoma. Oncology. 2010;78 Suppl 1:40-5.
6. Lee JY, Minami Y, Choi BI, Lee WJ, Chou YH, Jeong WK, et al. The AFSUMB consensus statements and recommendations for the clinical practice of contrast-enhanced ultrasound using Sonazoid. Ultrasonography. 2020;39:191-220.
7. Miyamoto Y, Ito T, Takada E, Omoto K, Hirai T, Moriyasu F. Efficacy of Sonazoid (perflubutane) for contrast-enhanced ultrasound in the differentiation of focal breast lesions: phase 3 multicenter clinical trial. AJR Am J Roentgenol. 2014;202:W400-7.

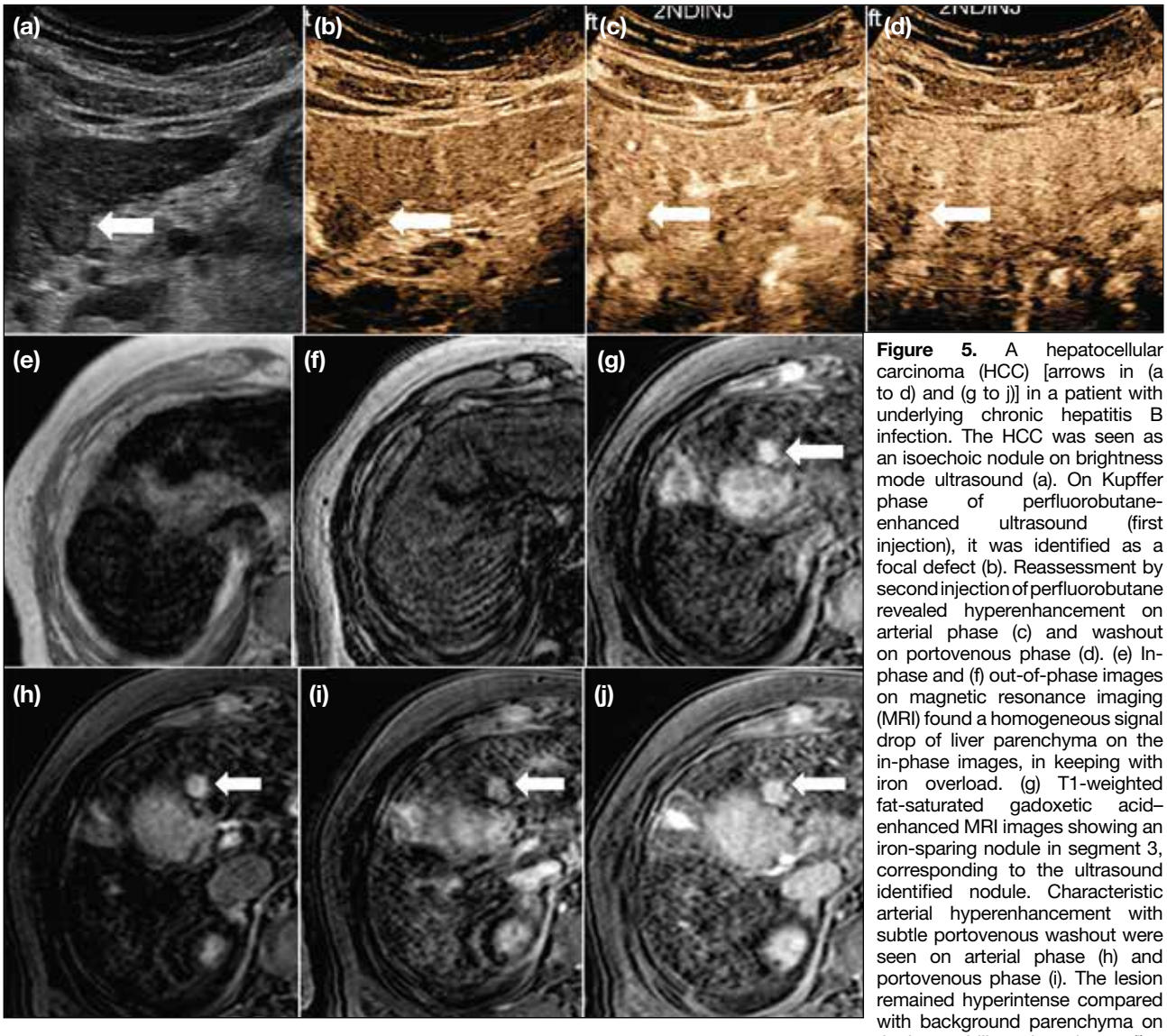

Figure 5. A hepatocellular carcinoma (HCC) [arrows in (a to d) and (g to j)] in a patient with underlying chronic hepatitis B infection. The HCC was seen as an isoechoic nodule on brightness mode ultrasound (a). On Kupffer phase of perfluorobutane-enhanced ultrasound (first injection), it was identified as a focal defect (b). Reassessment by second injection of perfluorobutane revealed hyperenhancement on arterial phase (c) and washout on portovenous phase (d). (e) In-phase and (f) out-of-phase images on magnetic resonance imaging (MRI) found a homogeneous signal drop of liver parenchyma on the in-phase images, in keeping with iron overload. (g) T1-weighted fat-saturated gadoxetic acid–enhanced MRI images showing an iron-sparing nodule in segment 3, corresponding to the ultrasound identified nodule. Characteristic arterial hyperenhancement with subtle portovenous washout were seen on arterial phase (h) and portovenous phase (i). The lesion remained hyperintense compared with background parenchyma on the hepatobiliary phase image (j).

Table 8. Adverse events.*

	Day 7 No. of patients (Grade)	Day 90 No. of patients (Grade)	Duration
Injection site pain	1 (1)	0	N/A
Sore throat	1 (1)	0	2 days
Cough	1 (1)	0	2 days
Hand stiffness	1 (1)	0	2 hours
Leg cramp	0	1 (1)	Once
Anal pain	1 (1)	0	1 week
Gastrointestinal discomfort	1 (2)	1 (1)	1 week
Malaise	0	1 (1)	N/A

Abbreviation: N/A = not available.
* No immediate adverse event was recorded.

8. Hatanaka K, Kudo M, Minami Y, Maekawa K. Sonazoid-enhanced ultrasonography for diagnosis of hepatic malignancies: comparison with contrast-enhanced CT. Oncology. 2008;75 Suppl 1:42-7.
9. Dietrich CF, Nolsøe CP, Barr RG, Berzigotti A, Burns PN, Cantisani V, et al. Guidelines and good clinical practice recommendations for contrast-enhanced ultrasound (CEUS) in the liver—update 2020—WFUMB in cooperation with EFSUMB, AFSUMB, AIUM, and FLAUS. Ultraschall Med. 2020;41:562-85.
10. Zhai HY, Liang P, Yu J, Cao F, Kuang M, Liu FY, et al. Comparison of Sonazoid and SonoVue in the diagnosis of focal liver lesions: a preliminary study. J Ultrasound Med. 2019;38:2417-25.
11. Lv K, Zhai H, Jiang Y, Liang P, Xu HX, Du L, et al. Prospective assessment of diagnostic efficacy and safety of Sonazoid™ and SonoVue® ultrasound contrast agents in patients with focal liver lesions. Abdom Radiol (NY). 2021;46:4647-59.
12. Kan M, Hiraoka A, Uehara T, Hidaka S, Ichiryu M, Nakahara H,

et al. Evaluation of contrast-enhanced ultrasonography using perfluorobutane (Sonazoid®) in patients with small hepatocellular carcinoma: comparison with dynamic computed tomography. Oncol Lett. 2010;1:485-8.
13. Eso Y, Takai A, Takeda H, Matsumoto T, Lee M, Inuzuka T, et al. Sonazoid-enhanced ultrasonography guidance improves the quality of pathological diagnosis in the biopsy of focal hepatic lesions. Eur J Gastroenterol Hepatol. 2016;28:1462-7.
14. Park HS, Kim YJ, Yu MH, Jung SI, Jeon HJ. Real-time contrast-enhanced sonographically guided biopsy or radiofrequency ablation of focal liver lesions using perfluorobutane microbubbles (Sonazoid): value of Kupffer-phase imaging. J Ultrasound Med. 2015;34:411-21.
15. Minami Y, Kudo M, Hatanaka K, Kitai S, Inoue T, Hagiwara S, et al. Radiofrequency ablation guided by contrast harmonic sonography using perfluorocarbon microbubbles (Sonazoid) for hepatic malignancies: an initial experience. Liver Int. 2010;30:759-64.
16. Masuzaki R, Shiina S, Tateishi R, Yoshida H, Goto E, Sugioka Y, et al. Utility of contrast-enhanced ultrasonography with Sonazoid in radiofrequency ablation for hepatocellular carcinoma. J Gastroenterol Hepatol. 2011;26:759-64.
17. Dohmen T, Kataoka E, Yamada I, Miura K, Ohshima S, Shibuya T, et al. Efficacy of contrast-enhanced ultrasonography in radiofrequency ablation for hepatocellular carcinoma. Intern Med. 2012;51:1-7.
18. Shiozawa K, Watanabe M, Kikuchi Y, Kudo T, Maruyama K, Sumino Y. Evaluation of sorafenib for hepatocellular carcinoma by contrast-enhanced ultrasonography: a pilot study. World J Gastroenterol. 2012;18:5753-8.
19. Sugimoto K, Moriyasu F, Saito K, Rognin N, Kamiyama N, Furuichi Y, et al. Hepatocellular carcinoma treated with sorafenib: early detection of treatment response and major adverse events by contrast-enhanced US. Liver Int. 2013;33:605-15.
20. Xia Y, Kudo M, Minami Y, Hatanaka K, Ueshima K, Chung H, et al. Response evaluation of transcatheter arterial chemoembolization in hepatocellular carcinomas: the usefulness of Sonazoid-enhanced harmonic sonography. Oncology. 2008;75 Suppl 1:99-105.
21. Kono Y, Lucidarme O, Choi SH, Rose SC, Hassanein TI, Alpert E, et al. Contrast-enhanced ultrasound as a predictor of treatment efficacy within 2 weeks after transarterial chemoembolization of hepatocellular carcinoma. J Vasc Interv Radiol. 2007;18:57-65.
22. Funaoka A, Numata K, Takeda A, Saigusa Y, Tsurugai Y, Nihonmatsu H, et al. Use of contrast-enhanced ultrasound with Sonazoid for evaluating the radiotherapy efficacy for hepatocellular carcinoma. Diagnostics (Basel). 2021;11:486.
23. Sugimoto K, Kakegawa T, Takahashi H, Tomita Y, Abe M, Yoshimasu Y, et al. Usefulness of modified CEUS LI-RADS for the diagnosis of hepatocellular carcinoma using Sonazoid. Diagnostics (Basel). 2020;10:828.
24. Hwang JA, Jeong WK, Min JH, Kim YY, Heo NH, Lim HK. Sonazoid-enhanced ultrasonography: comparison with CT/MRI liver imaging reporting and data system in patients with suspected hepatocellular carcinoma. Ultrasonography. 2021;40:486-98.
25. Minami Y, Kudo M. Contrast-enhanced ultrasonography with Sonazoid in hepatocellular carcinoma diagnosis. Hepatoma Res. 2020;6:46.
26. Miyamoto Y, Ito T, Takada E, Omoto K, Hirai T, Moriyasu F. Efficacy of Sonazoid (perflubutane) for contrast-enhanced ultrasound in the differentiation of focal breast lesions: phase 3 multicenter clinical trial. AJR Am J Roentgenol. 2014;202:W400-7.
27. Mori Y, Hayakawa A, Abe K, Tanigawa M, Takahashi M, Naruse H, et al. The safety and the efficacy of ultrasound contrast media perflubutane microbubbles in clinical practice. Choonpa Igaku. 2011;38:541-48.
28. American College of Radiology Committee on LI-RADS. CT/MRI LI-RADS® v2018 CORE. Available from: https://www.acr.org/-/media/ACR/Files/RADS/LI-RADS/LI-RADS-2018-Core.pdf. Accessed 17 Jul 2022.
29. Department of Health and Human Services, United States Government. Common Terminology Criteria for Adverse Events (CTCAE) Version 5.0. 2017. Available from: https://ctep.cancer.gov/protocoldevelopment/electronic_applications/docs/ctcae_v5_quick_reference_5x7.pdf. Accessed 2 May 2022.
30. Park JH, Park MS, Lee SJ, Jeong WK, Lee JY, Park MJ, et al. Contrast-enhanced US with perfluorobutane for hepatocellular carcinoma surveillance: a multicenter diagnostic trial (SCAN). Radiology. 2019;292:638-46.
31. Choi JY, Lee JM, Sirlin CB. CT and MR imaging diagnosis and staging of hepatocellular carcinoma: Part II. Extracellular agents, hepatobiliary agents, and ancillary imaging features. Radiology. 2014;273:30-50.
32. Kim MJ, Rhee HJ, Jeong HT. Hyperintense lesions on gadoxetate disodium–enhanced hepatobiliary phase imaging. AJR Am J Roentgenol. 2012;199:W575-86.
33. Kim JY, Kim MJ, Kim KA, Jeong HT, Park YN. Hyperintense HCC on hepatobiliary phase images of gadoxetic acid–enhanced MRI: correlation with clinical and pathological features. Eur J Radiol. 2012;81:3877-82.
34. Korenaga K, Korenaga M, Furukawa M, Yamasaki T, Sakaida I. Usefulness of Sonazoid contrast-enhanced ultrasonography for hepatocellular carcinoma: comparison with pathological diagnosis and superparamagnetic iron oxide magnetic resonance images. J Gastroenterol. 2009;44:733-41.

Hong Kong J Radiol. 2024;27(1):e28-38. Published 21 March 2024 | https://doi.org/10.12809/hkjr2217606

ORIGINAL ARTICLE

Contrast-Enhanced Spectral Mammography Versus Magnetic Resonance Imaging: Intra- and Inter-Observer Agreements in Tumour Size Assessment

TY Ko[1], AYT Lai[1], BST Leung[2], MKK Law[1], AHC Wong[1], KH Chin[1], WWC Wong[1]

[1]*Department of Radiology, Pamela Youde Nethersole Eastern Hospital, Hong Kong SAR, China*
[2]*Department of Radiology, CUHK Medical Centre, Hong Kong SAR, China*

ABSTRACT

Introduction: *In patients with locally advanced breast carcinomas undergoing neoadjuvant chemotherapy (NAC), imaging monitoring is important for guiding clinical management. Contrast-enhanced spectral mammography (CESM) is a recently introduced modality that may serve this purpose as an alternative to magnetic resonance imaging (MRI). We aimed to investigate intra- and inter-observer agreements in CESM and MRI in assessment of tumour size.*

Methods: *Imaging studies performed between December 2019 and March 2022 for breast cancer patients undergoing NAC were retrospectively reviewed. Two radiologists measured the largest lesion sizes, intra- and inter-observer agreements were measured using the intraclass correlation coefficient. To assess the agreement between CESM and MRI findings, Lin's concordance correlation coefficient (CCC) and Bland–Altman plots were used. Scanning time and reading time were recorded and compared.*

Results: *12 cases of patients who had undergone a total of 20 CESM studies and 18 MRI studies were assessed. The intra-observer agreement for the two radiologists on CESM was 0.983 and 0.996. The inter-observer agreement on CESM was 0.995. For MRI, the intra-observer agreement was 0.975 and 0.984, while the inter-observer agreement was 0.982. The agreement between the 10 baseline CESM and MRI studies was high (CCC = 0.972). Both the scanning time and reading time were significantly shorter for CESM than MRI (both $p < 0.001$).*

Conclusion: *Our results provide further evidence of CESM measurement reproducibility before, during, and after NAC. CESM can be considered an alternative assessment modality for monitoring NAC response.*

Key Words: *Breast neoplasms; Magnetic resonance imaging; Mammography; Neoadjuvant therapy*

Correspondence: *Dr TY Ko, Department of Radiology, Pamela Youde Nethersole Eastern Hospital, Hong Kong SAR, China*
Email: kty164@ha.org.hk

Submitted: 6 July 2022; Accepted: 22 January 2023.

Contributors: TYK, AYTL and BSTL designed the study. All authors acquired the data. TYK and AYTL analysed the data and drafted the manuscript. All authors critically revised the manuscript for important intellectual content. All authors had full access to the data, contributed to the study, approved the final version for publication, and take responsibility for its accuracy and integrity.

Conflicts of Interest: All authors have disclosed no conflicts of interest.

Funding/Support: This research received no specific grant from any funding agency in the public, commercial, or not-for-profit sectors.

Data Availability: All data generated or analysed during the present study are available from the corresponding author on reasonable request.

Ethics Approval: This research was approved by the Hong Kong East Cluster Research Ethics Committee of Hospital Authority, Hong Kong (Ref No.: HKECREC-2022-046). The requirement for informed patient consent was waived by the Committee due to the retrospective nature of the study.

Acknowledgement: The authors thank the following individuals for their contribution in patient selection and clinical assessment: Dr Yeuk-hei Ling (Ruttonjee Hospital), Dr Bonnie Pui-ling Chau (Ruttonjee Hospital), Dr Jennifer Suet-ying Lee (Pamela Youde Nethersole Eastern Hospital), and Dr Lorraine Wai-yan Ma (Pamela Youde Nethersole Eastern Hospital).

中文摘要

對比增強波譜乳房造影與磁力共振：腫瘤大小評估中觀察者內和觀察者間的一致性

高子恩、黎爾德、梁肇庭、羅嘉麒、黃可澄、錢凱、黃慧中

引言：對於接受術前輔助化療的局部晚期乳腺癌患者，影像監測在指導臨床治療方面非常重要。對比增強波譜乳房造影（CESM）是最近推出的一種模式，可用於此目的並作為磁力共振的替代方案。本文研究CESM和磁力共振中觀察者內和觀察者間評估腫瘤大小的一致性。

方法：我們對2019年12月至2022年3月期間接受術前輔助化療的乳腺癌患者的影像學檢查進行回顧性分析。最大的病灶尺寸由兩位放射科醫生測量，並使用組內相關系數評估觀察者內和觀察者間的一致性。我們使用Lin氏一致性相關系數和Bland-Altman圖評估CESM和磁力共振結果之間的一致性，以及記錄並比較掃描時間和閱片時間。

結果：12例患者接受了共20次CESM檢查和18次磁力共振檢查。兩位放射科醫生的CESM觀察者內一致性為0.983和0.996，觀察者間一致性為0.995。磁力共振觀察者內一致性為0.975和0.984，觀察者間一致性為0.982。十次基線CESM和磁力共振檢查間的一致性很高（一致性相關系數 = 0.972）。CESM的掃描時間和閱片時間均顯著短於磁力共振（兩者p值均為 < 0.001）。

結論：我們的結果進一步證明了術前輔助化療之前、期間和之後CESM測量的可重複性。CESM可視為術前輔助化療療效監測的替代方式。

INTRODUCTION

Neoadjuvant chemotherapy (NAC) is currently the treatment of choice for patients presenting with unresectable disease, locally advanced disease, or inflammatory breast cancer, all of which NAC may render resectable.[1,2] After NAC, an improved tumour-breast ratio may allow breast-conserving surgery, which leads to a better cosmetic outcome. In patients with human epidermal growth factor receptor 2–positive and triple-negative breast cancer (TNBC) subtypes, findings of residual disease after NAC provide prognostic information and can guide further adjuvant therapy.[3,4] Accurate assessment of NAC response is therefore important to guide subsequent management. Initially, response to NAC was assessed by a combination of clinical examination, mammography, and ultrasound. Subsequently, contrast-enhanced magnetic resonance imaging (MRI) was proven to be a superior imaging modality, with better assessment of tumour extent, visualisation of additional tumour foci, and identification of residual disease after NAC.[5,6] One of the major advantages of MRI is the fact that it allows contrast-enhanced imaging. However, the relatively high cost, low availability, and long image acquisition time of MRI may restrict patient access. Recently, contrast-enhanced spectral mammography (CESM) has been developed as an imaging tool which utilises a dual-energy technique to combine the advantages of digital mammography with contrast-enhanced imaging. When evaluating tumour extent, CESM had better correlation with the size measured in histopathology specimens when compared with standard mammography and ultrasound.[7] In the setting of NAC response monitoring, early data have shown CESM to be promising when compared to MRI.[8-10] One study concluded that CESM has better agreement with histological assessment of surgical specimen in demonstrating complete pathological response as compared to MRI.[8] Initial results[8-10] have suggested CESM to be a viable alternative to MRI in the setting of NAC response monitoring.

The aim of this study was to assess the intra-observer and inter-observer agreements in CESM and MRI to further study the validity of CESM as an alternative option for tumour size evaluation before and after NAC.

METHODS

Patients

From December 2019 to March 2022, a total of 12 patients were referred to Pamela Youde Nethersole

Eastern Hospital for imaging monitoring of NAC response. All patients had confirmed locally invasive breast carcinoma through tissue sampling and underwent CESM and/or MRI prior to the commencement of NAC as a baseline study, with 10 patients undergoing both CESM and MRI within 3 days of each other. Follow-up CESM and/or MRI was performed at mid-cycle and/or end of treatment.

Contrast-Enhanced Spectral Mammography

CESM was performed using the Selenia Dimensions Mammography system (Hologic, Marlborough [MA], US). Iohexol (Omnipaque; GE Healthcare, Milwaukee [WI], US) was used as the CESM contrast agent. The amount administered was calculated at 1.5 mL/kg,[11] and administered at a rate of 3 mL/s through a power injector. CESM images were then acquired 2 minutes after contrast injection and completed within 10 minutes, allowing an 8-minute window for image acquisition (Figure 1).[11] CESM high-energy (45-49 kV) and low-energy (28-33 kV) images were obtained in the craniocaudal and mediolateral oblique projections for each breast. CESM high-energy images were used to produce subtracted images; the low-energy and subtracted images were displayed for review by radiologists. The CESM images were then immediately reviewed by the session radiologist, and additional views, e.g., magnified and compression views, were obtained if deemed necessary (Figure 1). The time required for each CESM study was recorded, starting at contrast injection and concluding at the last image acquired.

Magnetic Resonance Imaging

MRI was performed utilising the Siemens-Avanto 1.5T MRI scanner (Erlangen, Germany), with patients in the prone position. Gadoterate meglumine (Dotarem; Guerbet, Villepinte, France) was used as contrast agent. Sequences acquired included fat-suppressed axial T2-weighted sequence, coronal T2-weighted sequence, axial T1-weighted sequence with dynamic contrast (first sequence before contrast administration and seven acquisitions after contrast agent administration each spaced 1 minute apart), and axial diffusion-weighted sequences. The time required for each MRI study was recorded.

Imaging Interpretation

CESM and MRI images were interpreted by two radiologists: a specialist radiologist with > 7 years' experience in breast imaging, and a trainee radiologist with 1 year of experience in breast imaging. During image interpretation, the radiologists were blinded to the measurements of the other imaging modality as well as the measurements of the other radiologist. The images from different patients were interpreted in a randomised sequence and were interpreted twice by each radiologist with a 2-month interval. In CESM, both low-energy and subtracted images were reviewed (Figure 2). The largest lesion in each breast was measured, disregarding peritumoral calcifications. In MRI, the single largest lesion was assessed in different sequences and planes, where the largest dimension was recorded (Figures 3 and 4). The presence of any satellite lesions was also

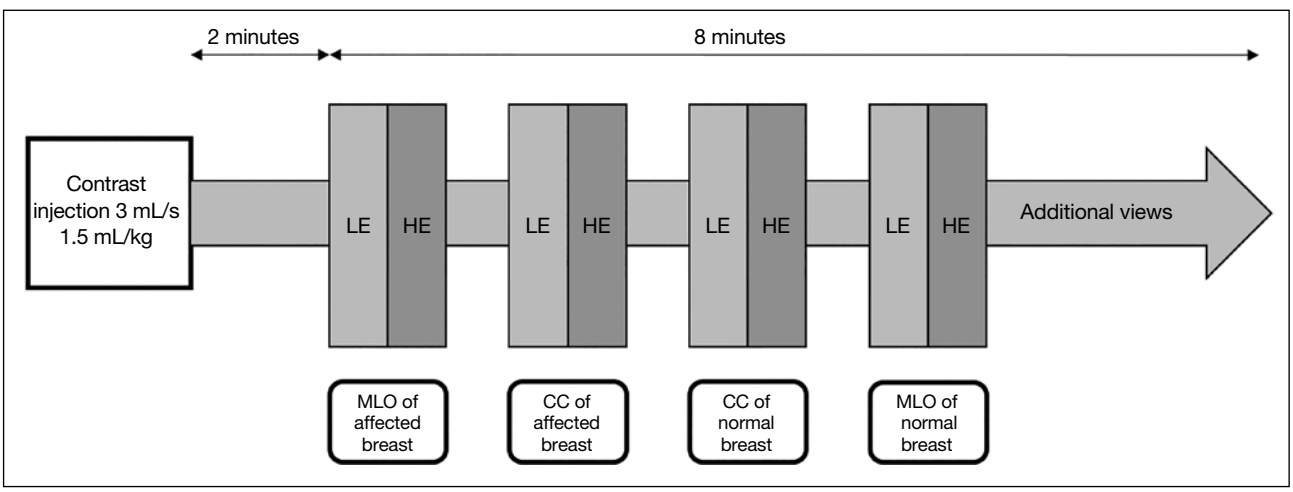

Figure 1. Workflow of contrast-enhanced spectral mammography. Contrast was injected by a power injector. After injection, the patient was disconnected from the injector and led to the mammography machine where the breasts were positioned and compressed and images were acquired. After review by a radiologist, additional views were acquired if deemed necessary.
Abbreviations: CC = craniocaudal view; HE = high-energy; LE = low-energy; MLO = mediolateral oblique view.

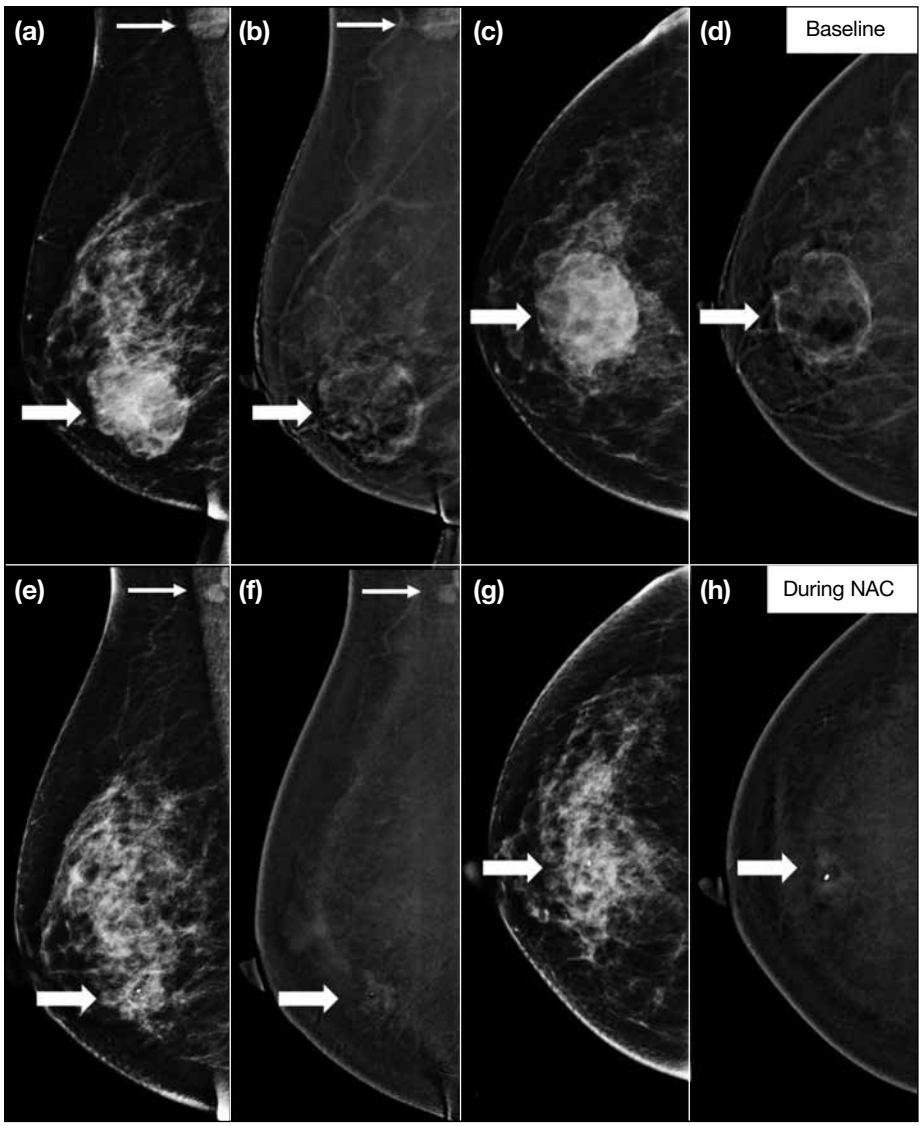

Figure 2. Contrast-enhanced spectral mammography showing partial response (comparing upper and lower rows) in a 52-year-old woman with invasive ductal carcinoma (luminal A subtype). The primary tumour (thick arrows) show size reduction from 44 mm to 18 mm. A right axillary lymph node metastasis (thin arrows in [a], [b], [e], and [f]) also shows reduction in size. A marker was placed within the tumour under ultrasound guidance before the commencement of neoadjuvant chemotherapy (NAC). (a) Low-energy right mediolateral oblique (MLO) view at baseline. (b) Subtracted right MLO view at baseline. (c) Low-energy right craniocaudal (CC) view at baseline. (d) Subtracted right CC view at baseline. (e) Low-energy right MLO view at mid-cycle. (f) Subtracted right MLO view at mid-cycle. (g) Low-energy right CC view at mid-cycle. (h) Subtracted right CC view at mid-cycle.

recorded on both CESM and MRI, and, if the entire lesion was included, the largest dimension of the satellite lesion was measured (Figure 5). Reading time for each imaging study was also recorded, defined as the time between opening and closing the images on the viewing programme after recording the dimension of the largest lesion.

Statistical Analysis

The intraclass correlation coefficient (ICC) was used to evaluate the intra- and inter-observer agreements of both CESM and MRI results, using a two-way mixed model testing for absolute agreement with a 95% confidence interval (CI). Intra-observer agreement was analysed for both radiologists, while inter-observer agreement was analysed using the first measurements by both radiologists. Subgroup analysis was performed by dividing the CESM studies into baseline studies and non-baseline studies, i.e., mid-cycle and end-of-cycle studies. Intra- and inter-observer agreements of these subgroups was calculated by ICC. Lin's concordance correlation coefficient (CCC) and Bland–Altman plots were used to evaluate for agreement between the CESM and MRI studies in the cases of 10 patients who had undergone both baseline imaging studies within 3 days. The Mann–Whitney *U* test was used to compare the scanning and reading times of CESM and MRI. Statistical analysis was performed using SPSS (Windows version 20.0; IBM Corp, Armonk [NY], US).

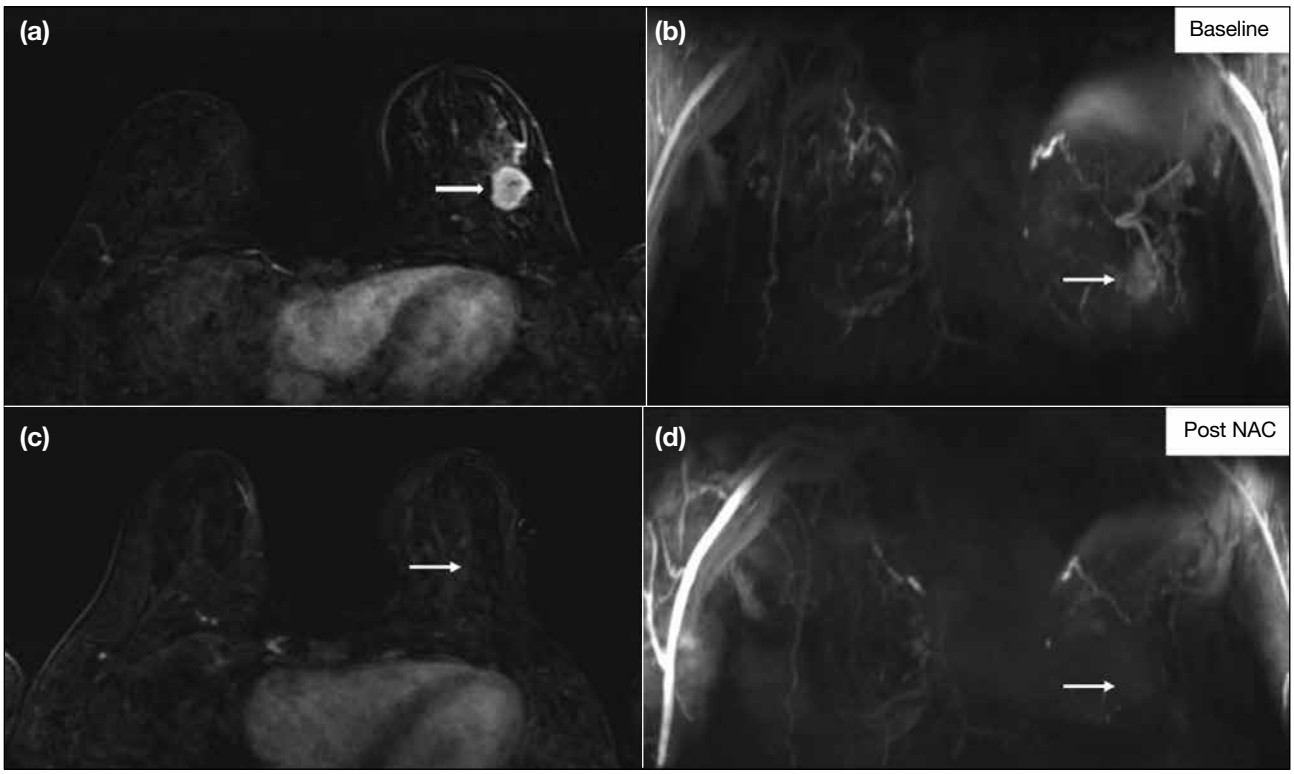

Figure 3. Magnetic resonance imaging (MRI) showing complete response (comparing upper and lower rows) in a 45-year-old woman with invasive ductal carcinoma (luminal A subtype). At baseline, the largest lesion measured 21 mm (arrows in [a] and [b]). No residual lesion was noted on post–neoadjuvant chemotherapy (NAC) MRI. Postoperative pathology confirmed no residual tumour (arrows in [c] and [d]). (a) Axial post-contrast baseline T1-weighted subtracted image at peak enhancement. (b) Coronal post-contrast baseline T1-weighted maximum intensity projection (MIP) image. (c) Axial post-contrast T1-weighted subtracted image after NAC. (d) Coronal post-contrast T1-weighted MIP image after NAC.

RESULTS

All 12 cases were female, with a mean age of 50.7 years (range, 32-66). Eleven cases were of invasive ductal carcinoma and there was one case of invasive lobular carcinoma. There were six cases of luminal A subtype, three of luminal B subtype, and three of human epidermal growth factor receptor 2–positive subtype. There were no cases of TNBC. Out of the 12 cases, one patient presented with urticaria after iodinated contrast administration during CESM. None of the patients presented with contrast reactions after gadolinium contrast administration.

In total, 20 CESM studies and 18 MRI studies were interpreted by the two radiologists. Individual measurements for the largest lesion detected for each study are summarised in Tables 1 and 2. Overall, the ICCs for both CESM and MRI were high, as summarised in Table 3. The results for the subgroup analysis comparing baseline and non-baseline CESM studies are summarised in Table 4.

Table 5 summarises the results of the baseline CESM and MRI studies. The CCC for comparing between the two sets of baseline CESM and MRI studies was 0.972 (95% CI = 0.893-0.993; n = 10). The Bland–Altman plot showed a bias of -1.1 mm and limits of agreement of -9.7 to 7.5 mm between modalities (Figure 6).

A satellite lesion was only identified in one CESM study. Both radiologists identified the lesion, with measurements of 12 mm and 14 mm, respectively. MRI was not performed on this patient; therefore, comparison cannot be made. On the end-of-cycle CESM study performed on this patient, both radiologists concurred that the satellite lesion had resolved (Figure 5).

The median scanning time for CESM was 4.9 minutes (interquartile range [IQR] = 1.3), while that for MRI was 43.9 minutes (IQR = 10.8). The median reading time for measuring the dimension of the largest lesion on CESM was 54.5 seconds (IQR = 17.5), while that for MRI was 96 seconds (IQR = 55). The results of the

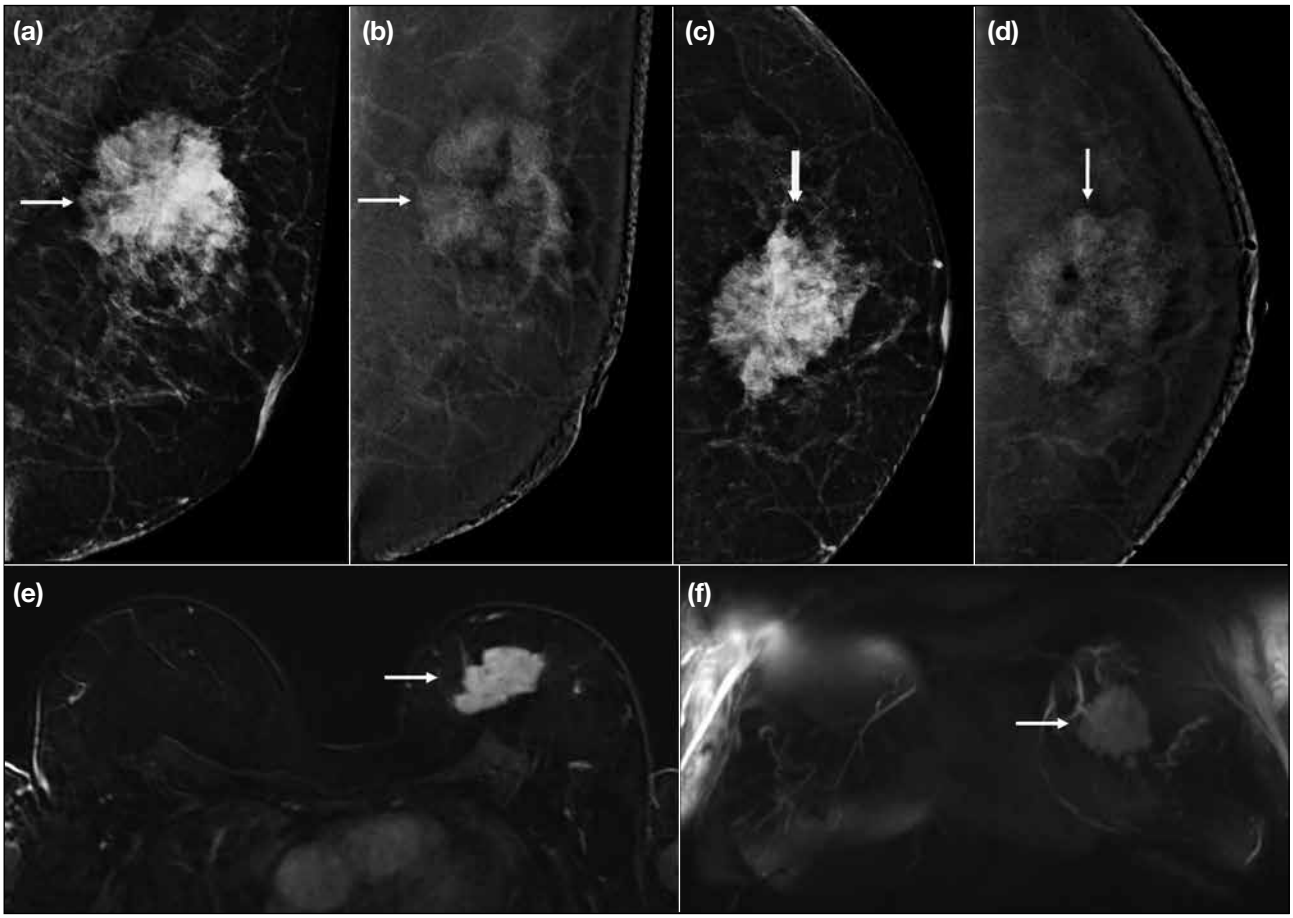

Figure 4. Contrast-enhanced spectral mammography and magnetic resonance imaging performed at baseline for a 57-year-old woman with invasive ductal carcinoma (luminal B subtype). Both modalities measured the largest dimension at 48 mm (arrows). (a) Low-energy left mediolateral oblique (MLO) view. (b) Subtracted left MLO view. (c) Low-energy left craniocaudal (CC) view. (d) Subtracted left CC view. (e) Axial post-contrast T1-weighted subtracted image at peak enhancement. (f) Coronal post-contrast T1-weighted maximum intensity projection image.

Mann–Whitney *U* test showed that both the scanning and reading times for CESM were significantly shorter ($p < 0.001$).

DISCUSSION

Contrast-enhanced imaging has substantial advantages in assessing NAC response. Contrast enhancement is based on abnormal angiogenesis in malignant tumours, which results in the leakage of contrast medium from the immature tumour vessels into the interstitial spaces. MRI, which benefits from contrast-enhanced imaging, has been proven to be a superior imaging modality to traditional mammography and ultrasound.[5,6] CESM is another emerging modality which also benefits from contrast-enhanced imaging. Intravenous iodinated contrast is administered to the patient, and after 2 minutes contrast material reaches the breast tissues,[11] allowing image acquisition to begin. It utilises a dual-energy technique, obtaining two spectral images using different energy levels in quick succession while the breast remains compressed. In the low-energy setting, the energy is below the k-edge of iodine and contrast material is not imaged, and the image can be interpreted as a standard mammogram. In the high-energy setting, which is above the k-edge of iodine, a non-interpretable image is produced. Using subtraction, an image depicting only areas of contrast enhancement results. The low-energy image and the subtracted image are then interpreted together by a radiologist. Owing to the subtraction method and contrast-enhanced imaging, CESM has been shown to be superior to standard mammography in cancer diagnosis even in dense breasts.[12]

Along with the advancements in CESM, several

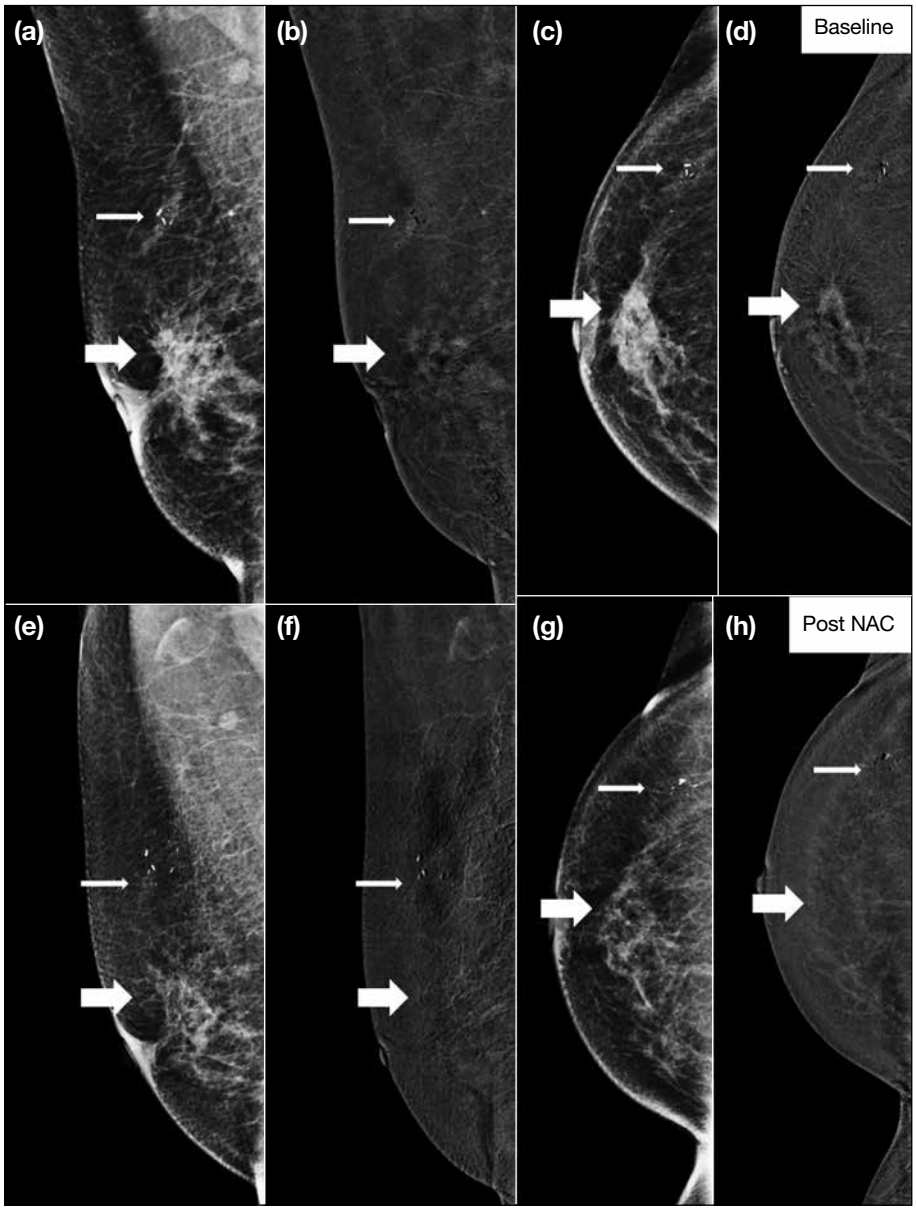

Figure 5. Contrast-enhanced spectral mammography showing complete response in a 61-year-old woman with invasive ductal carcinoma (human epidermal growth factor receptor 2–positive subtype). At baseline (upper row), a primary tumour (thick arrows) is noted in the centre of the right breast. An additional satellite lesion is noted in the upper outer quadrant (thin arrows), with associated calcifications. Both the primary tumour and satellite lesion showed resolution of enhancement after neoadjuvant chemotherapy (NAC) [lower row], while calcifications associated with the satellite lesion are more dispersed. Postoperative pathology confirmed no residual tumour. (a) Low-energy right mediolateral oblique (MLO) baseline view. (b) Subtracted right MLO baseline view. (c) Low-energy right craniocaudal (CC) baseline view. (d) Subtracted right CC baseline view. (e) Low-energy post-NAC right MLO view. (f) Subtracted post-NAC right MLO view. (g) Low-energy post-NAC right CC view. (h) Subtracted right post-NAC CC view.

studies have compared the performance of CESM to MRI in monitoring NAC response. One study showed that even though the use of CESM and MRI both led to underestimation of the extent of residual tumour compared to histology findings, CESM demonstrated pathologic complete responses to NAC better than MRI.[8] Other studies showed that CESM had good correlation and agreement with histopathology comparable to MRI, also showing high positive predictive values.[9,10] Despite the positive results, these studies did not thoroughly compare intra- and inter-observer agreements in CESM and MRI when assessing NAC. As shown by our results, the intra- and inter-observer agreements for CESM were excellent, all showing ICCs > 0.98. These results are comparable with the intra- and inter-observer agreements in MRI, which showed ICCs > 0.97. Despite the fact that one of the radiologists in the current study was a trainee radiologist with only 1 year of experience in breast imaging, the inter-observer agreement remained high. This concurred with findings in previous studies,[12,13] suggesting that CESM techniques could be easily learned by breast radiologists, which may be attributed to its findings being akin to basic mammography observations. Subgroup analysis was performed comparing the intra-

Table 1. Measurements of the largest lesion detected in each contrast-enhanced spectral mammography study.

Patient	Age, y	Treatment status	CESM (largest lesion dimension, mm)			
			Rater 1		Rater 2	
			First read	Second read	First read	Second read
A	56	Baseline	55	51	56	57
		Mid-cycle	12	11	13	15
B	52	Baseline	44	45	43	43
		Mid-cycle	19	18	20	20
C	56	Baseline	50	50	51	51
D	53	Baseline	19	19	18	19
E	48	Baseline	91	109	91	93
		Mid-cycle	22	24	24	25
F	52	Baseline	39	38	37	33
		Mid-cycle	15	16	11	13
G	54	Baseline	41	41	42	41
		End-of-cycle	12	15	13	13
H	45	Baseline	22	20	23	22
		Mid-cycle	0	0	0	0
I	33	Baseline	47	51	52	50
		Mid-cycle	0	0	0	0
J	32	Baseline	35	39	32	37
K	66	Baseline	20	19	25	29
L	61	Baseline	13	15	14	13
		End-of-cycle	0	0	0	0

Abbreviation: CESM = contrast-enhanced spectral mammography.

Table 2. Measurements of the largest lesion detected in each magnetic resonance imaging study.

Patient	Age, y	Treatment status	MRI (largest lesion dimension, mm)			
			Rater 1		Rater 2	
			First read	Second read	First read	Second read
A	56	Baseline	65	54	52	66
		End-of-cycle	0	0	0	0
B	52	Baseline	50	48	50	54
		End-of-cycle	19	18	17	20
C	56	Baseline	50	49	48	49
D	53	Baseline	24	24	31	28
		End-of-cycle	15	18	17	15
E	48	Baseline	59	109	90	85
		End-of-cycle	33	33	26	25
F	52	Baseline	41	38	34	37
G	54	Baseline	38	38	37	38
		End-of-cycle	15	15	13	15
H	45	Baseline	22	22	21	22
		End-of-cycle	0	0	0	0
I	33	Baseline	44	44	47	52
		End-of-cycle	0	0	0	0
J	32	Baseline	31	33	32	33
		Mid-cycle	22	22	22	21

Abbreviation: MRI = magnetic resonance imaging.

and inter-observer agreements in studies performed at baseline prior to the commencement of NAC, and in studies during or after NAC. It was thought that after NAC, responding tumours may show shrinkage in both size and enhancement, possibly affecting the agreement in size measurement as lesions may be less conspicuous.[8] Results showed that even though there was in fact a slight drop in ICC, inter-observer agreement remained excellent in the non-baseline group with an ICC of 0.983 (95% CI = 0.917-0.997), meaning that measurement reproducibility remained high during or after NAC. Ten of the patients in the current study underwent both CESM and MRI prior to the commencement of NAC. Agreement between the measurements of the two modalities was high: CCC was 0.972 and mean difference was only 1.1 mm. This provides further support for CESM as a viable alternative.

One of the advantages of CESM over MRI is the fact that the scanning time is much shorter. This was proven in the current study; scanning time in CESM was significantly shorter than MRI ($p < 0.001$). In fact, when considering the median scanning time required, more than eight CESM studies can be performed during the time required for one MRI study. Reading time was also significantly shorter in CESM than MRI ($p < 0.001$). This could be attributed to the fact that there are more sequences and images in an MRI study compared with CESM. However, it is important to keep in mind that the reading time measured in the current study is only regarding the measurement of the dimension of the largest lesion, disregarding background and incidental findings. Regardless, in the common scenario where there are large numbers of patients, the potential time saved through both scanning time and reading time is a major advantage of CESM over MRI.

Despite the excellent results shown in the current study, there are limitations to CESM. One of the patients presented with iodinated contrast allergy in the form of urticaria. Additionally, the rate of adverse reactions in iodinated contrast, such as nausea and headache, were found to be significantly higher than those of gadolinium contrast.[14] Thorough history taking and explanation must be performed with patients before proceeding to CESM. Radiation exposure is also an additional factor to consider.

The ability to evaluate microcalcifications is an advantage of CESM over MRI. Since this study only measured the dimension of the largest lesion, the effect of microcalcifications was not examined. Some studies concluded that residual microcalcifications

Table 3. Intraclass correlation coefficient scores for intra- and inter-observer agreements in contrast-enhanced spectral mammography and magnetic resonance imaging studies.*

	Intra-observer agreement		Inter-observer agreement
	Rater 1	Rater 2	
CESM (n = 20)	0.983 (0.957-0.993)	0.996 (0.991-0.998)	0.995 (0.989-0.998)
MRI (n = 18)	0.975 (0.934-0.990)	0.984 (0.958-0.994)	0.982 (0.953-0.993)

Abbreviations: CESM = contrast-enhanced spectral mammography; MRI = magnetic resonance imaging.
* Scores in parentheses are the 95% confidence intervals.

Table 4. Intraclass correlation coefficient scores for intra- and inter-observer agreements in contrast-enhanced spectral mammography studies performed at baseline and non-baseline.*

	Intra-observer agreement		Inter-observer agreement
	Rater 1	Rater 2	
Baseline	0.971 (0.905-0.991)	0.994 (0.978-0.998)	0.993 (0.978-0.998)
Non-baseline	0.988 (0.947-0.998)	0.994 (0.963-0.999)	0.983 (0.917-0.997)

* Scores in parentheses are the 95% confidence intervals.

Table 5. Comparison of results for both contrast-enhanced spectral mammography and magnetic resonance imaging studies performed on the same patients at baseline.

Patient	Age, y	CESM (largest lesion dimension, mm)				MRI (largest lesion dimension, mm)			
		Rater 1		Rater 2		Rater 1		Rater 2	
		First read	Second read	First read	Second read	First read	Second read	First read	Second read
A	56	55	51	56	57	65	54	52	66
B	52	44	45	43	43	50	48	50	54
C	56	50	50	51	51	50	49	48	49
D	53	19	19	18	19	24	24	31	28
E	48	91	109	91	93	59	109	90	85
F	52	39	38	37	33	41	38	34	37
G	54	41	41	42	41	38	38	37	38
H	45	22	20	23	22	22	22	21	22
I	33	47	51	52	50	44	44	47	52
J	32	35	39	32	37	31	33	32	33

Abbreviations: CESM = contrast-enhanced spectral mammography; MRI = magnetic resonance imaging.

after NAC correlated poorly with tumour size on final pathology.[15,16] Others showed that by including both contrast enhancement and residual calcifications in post-NAC CESM, sensitivity in residual disease detection increased but the false positive rate also increased.[17] Therefore, the effect and reporting of residual microcalcifications on post-NAC CESM requires further research.

A satellite lesion was only detected in one case in the current study. Correct identification of satellite lesions is important for monitoring NAC response since it may impact subsequent surgical planning. Multifocal or multicentric disease are also known to be associated with higher risk of locoregional recurrence after breast-conserving surgery.[18] The performance of CESM on detecting satellite lesions may require further research.

Limitations

There were several limitations of the current study. It was a single-institution study with a small patient population. The lack of TNBC within the molecular subgroups may limit the applicability of our results to the general population, given the fact that TNBC is one of

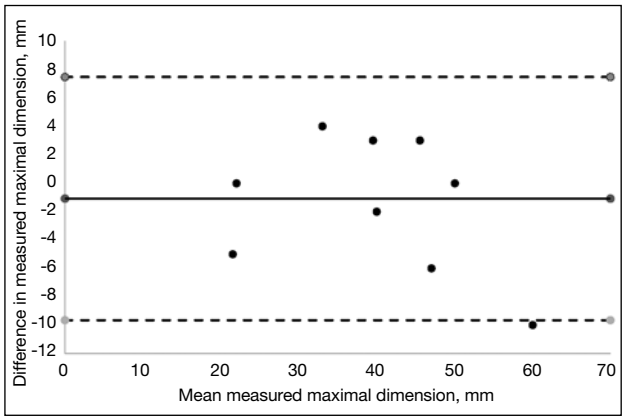

Figure 6. Bland–Altman plot of agreement between contrast-enhanced spectral mammography and magnetic resonance imaging studies performed on the same patients during baseline studies. Solid line represents the mean of differences. Dashed lines represent the 95% limit of agreement (± 1.96 times the standard deviation).

the indications for NAC. Due to the retrospective design and constraint in resources (as shown in Tables 1 and 2), patients could not be arranged to undergo both CESM and MRI at each point of the NAC cycle, therefore agreement in results of the two modalities could not always be compared to the non-baseline studies. Due to the same reason, comparison with postoperative histopathology could not be performed since most patients did not undergo both CESM and MRI as end-of-cycle imaging evaluations. Further research with histopathological correlation would be beneficial. Lastly, when evaluating intra-observer agreement, despite a 2-month interval between image evaluation, recognition of cases may produce measurement bias.

CONCLUSION

The current results showed that CESM had excellent intra- and inter-observer agreements which were comparable with MRI. Excellent agreement was found when comparing baseline CESM and MRI studies. Scanning and reading times were both significantly shorter in CESM. These results provided further evidence for CESM as a viable alternative to MRI for tumour size monitoring in assessing NAC response.

REFERENCES

1. Korde LA, Somerfield MR, Carey LA, Crews JR, Denduluri N, Hwang ES, et al. Neoadjuvant chemotherapy, endocrine therapy, and targeted therapy for breast cancer: ASCO guideline. J Clin Oncol. 2021;39:1485-505.
2. Ditsch N, Untch M, Thill M, Müller V, Janni W, Albert US, et al. AGO recommendations for the diagnosis and treatment of patients with early breast cancer: update 2019. Breast Care (Basel). 2019;14:224-45.
3. Morigi C. Highlights of the 16th St Gallen International Breast Cancer Conference, Vienna, Austria, 20-23 March 2019: personalised treatments for patients with early breast cancer. Ecancermedicalscience. 2019;13:924.
4. Werutsky G, Untch M, Hanusch C, Fasching PA, Blohmer JU, Seiler S, et al. Locoregional recurrence risk after neoadjuvant chemotherapy: a pooled analysis of nine prospective neoadjuvant breast cancer trials. Eur J Cancer. 2020;130:92-101.
5. Martincich L, Montemurro F, De Rosa G, Marra V, Ponzone R, Cirillo S, et al. Monitoring response to primary chemotherapy in breast cancer using dynamic contrast-enhanced magnetic resonance imaging. Breast Cancer Res Treat. 2004;83:67-76.
6. Lobbes MB, Prevos R, Smidt M, Tjan-Heijnen VC, van Goethem M, Schipper R, et al. The role of magnetic resonance imaging in assessing residual disease and pathologic complete response in breast cancer patients receiving neoadjuvant chemotherapy: a systematic review. Insights Imaging. 2013;4:163-75.
7. Ali-Mucheru M, Pockaj B, Patel B, Pizzitola V, Wasif N, Stucky CC, et al. Contrast-enhanced digital mammography in the surgical management of breast cancer. Ann Surg Oncol. 2016;23(Suppl 5):649-55.
8. Iotti V, Ravaioli S, Vacondio R, Coriani C, Caffarri S, Sghedoni R, et al. Contrast-enhanced spectral mammography in neoadjuvant chemotherapy monitoring: a comparison with breast magnetic resonance imaging. Breast Cancer Res. 2017;19:106.
9. Barra FR, Sobrinho AB, Barra RR, Magalhães MT, Aguiar LR, de Albuquerque GF, et al. Contrast-enhanced mammography (CEM) for detecting residual disease after neoadjuvant chemotherapy: a comparison with breast magnetic resonance imaging (MRI). Biomed Res Int. 2018;2018:8531916.
10. Patel BK, Hilal T, Covington M, Zhang N, Kosiorek HE, Lobbes M, et al. Contrast-enhanced spectral mammography is comparable to MRI in the assessment of residual breast cancer following neoadjuvant systemic therapy. Ann Surg Oncol. 2018;25:1350-6.
11. Jochelson MS, Dershaw DD, Sung JS, Heerdt AS, Thornton C, Moskowitz CS, et al. Bilateral contrast-enhanced dual-energy digital mammography: feasibility and comparison with conventional digital mammography and MR imaging in women with known breast carcinoma. Radiology. 2013;266:743-51.
12. Cheung YC, Lin YC, Wan YL, Yeow KM, Huang PC, Lo YF, et al. Diagnostic performance of dual-energy contrast-enhanced subtracted mammography in dense breasts compared to mammography alone: interobserver blind-reading analysis. Eur Radiol. 2014;24:2394-403.
13. Lalji UC, Houben IP, Prevos R, Gommers S, van Goethem M, Vanwetswinkel S, et al. Contrast-enhanced spectral mammography in recalls from the Dutch breast cancer screening program: validation of results in a large multireader, multicase study. Eur Radiol. 2016;26:4371-9.
14. Hunt CH, Hartman RP, Hesley GK. Frequency and severity of adverse effects of iodinated and gadolinium contrast materials: retrospective review of 456,930 doses. AJR Am J Roentgenol. 2009;193:1124-7.
15. Weiss A, Lee KC, Romero Y, Ward E, Kim Y, Ojeda-Fournier H, et al. Calcifications on mammogram do not correlate with tumor size after neoadjuvant chemotherapy. Ann Surg Oncol. 2014;21:3310-6.
16. Adrada BE, Huo L, Lane DL, Arribas EM, Resetkova E, Yang W. Histopathologic correlation of residual mammographic microcalcifications after neoadjuvant chemotherapy for locally

advanced breast cancer. Ann Surg Oncol. 2015;22:1111-7.
17. Iotti V, Ragazzi M, Besutti G, Marchesi V, Ravaioli S, Falco G, et al. Accuracy and reproducibility of contrast-enhanced mammography in the assessment of response to neoadjuvant chemotherapy in breast cancer patients with calcifications in the tumor bed. Diagnostics (Basel). 2021;11:435.
18. Vera-Badillo FE, Napoleone M, Ocana A, Templeton AJ, Seruga B, Al-Mubarak M, et al. Effect of multifocality and multicentricity on outcome in early-stage breast cancer: a systematic review and meta-analysis. Breast Cancer Res Treat. 2014;146:235-44.

Hong Kong J Radiol. 2024;27(1):e39-42. Published 12 March 2024 | https://doi.org/10.12809/hkjr2317697

CASE REPORT

Intraventricular H3K27-Altered Diffuse Midline Glioma in Lateral Ventricle: A Case Report

PL Kwok[1], YH Lui[2], HK Chin[1], LY Ho[3], SK Chan[3], CY Chu[1]

[1]*Department of Radiology, Pamela Youde Nethersole Eastern Hospital, Hong Kong SAR, China*
[2]*Department of Clinical Pathology, Pamela Youde Nethersole Eastern Hospital, Hong Kong SAR, China*
[3]*Department of Neurosurgery, Pamela Youde Nethersole Eastern Hospital, Hong Kong SAR, China*

CASE PRESENTATION

A 41-year-old man with glucose-6-phosphate dehydrogenase deficiency who was a light smoker of 5 pack years and social drinker first presented in 2022 in Hong Kong with left hemiparesis, unsteady gait and headache, with Glasgow Coma Scale score of 13. Non-contrast axial computed tomography of the brain revealed a tumour at the foramen of Monro with hydrocephalus (Figure 1a). Mannitol was administered and urgent external ventricular shunting was performed to relieve the hydrocephalus. A well-defined solitary intraventricular tumour (Figure 1b-h) measuring 2 × 2.3 × 2.7 cm^3 was seen on subsequent magnetic resonance imaging (MRI), epicentred at the right lateral ventricle/foramen of Monro. It was T1 iso- to hypointense, and T2 hyperintense with restricted diffusion and internal small foci of enhancement. There was no abnormal blooming artefact. The mass displaced the septum pellucidum to the left while the third ventricle was displaced to the left and inferiorly. Owing to its intraventricular location, it was first suspected to be a subependymoma, ependymoma, or central neurocytoma. Frozen section of a limited endoscopic biopsy was consistent with a glial tumour. Given the clinical history, an ependymoma or subependymoma remained possible but no definitive diagnosis was reached.

More formalin-fixed paraffin-embedded tissue was subsequently examined. The glial tumour (Figure 2a) showed moderate cellularity, moderate nuclear pleomorphism, enlarged hyperchromatic nuclei, and fibrillary eosinophilic cytoplasm. Mitotic count was up to 4 mitotic figures per 10 high-power fields. There was microvascular proliferation but no necrosis was seen. There was no rosette or pseudorosette. Immunohistochemical studies revealed that the tumour cells were positive for GFAP (glial fibrillary acidic protein), Olig2 (oligodendrocyte transcription factor

Correspondence: *Dr PL Kwok, Department of Radiology, Pamela Youde Nethersole Eastern Hospital, Hong Kong SAR, China*
Email: kpl995@ha.org.hk

Submitted: 9 January 2023; Accepted: 23 May 2023.

Contributors: PLK and CYC designed the study. All authors acquired the data. PLK and YHL analysed the data, drafted the manuscript, and critically revised the manuscript for important intellectual content. All authors had full access to the data, contributed to the study, approved the final version for publication, and take responsibility for its accuracy and integrity.

Conflicts of Interest: All authors have disclosed no conflicts of interest.

Funding/Support: This study received no specific grant from any funding agency in the public, commercial, or not-for-profit sectors.

Data Availability: All data generated or analysed during the present study are available from the corresponding author on reasonable request.

Ethics Approval: This study was approved by the Hong Kong East Cluster Research Ethics Committee of Hospital Authority, Hong Kong (Ref No.: HKECREC-2022-057). The patient was treated in accordance with the Declaration of Helsinki and patient consent was waived by the Committee due to no disclosure of patient's identity.

Acknowledgement: The authors thank Prof HK Ng, Department of Anatomical and Cellular Pathology of Prince of Wales Hospital, for advising on the pathological diagnosis of the study.

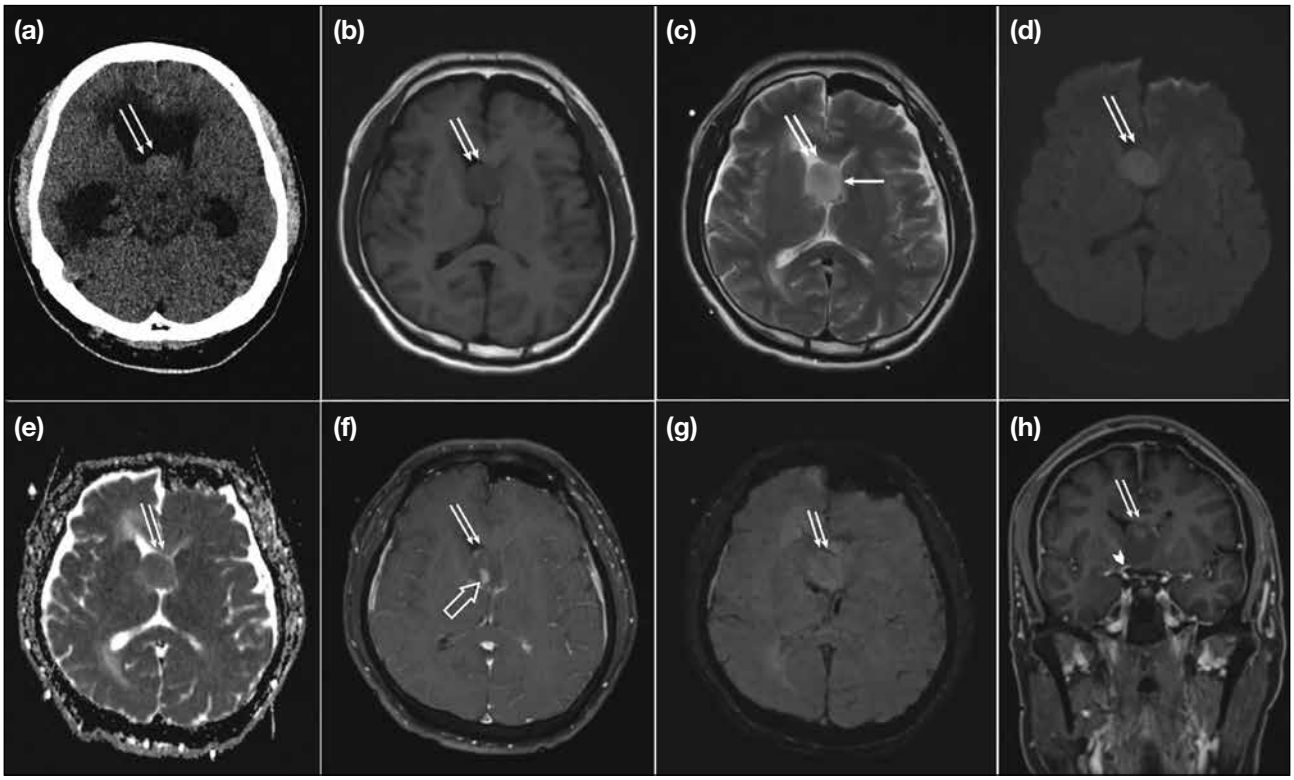

Figure 1. Non-contrast axial computed tomography (CT) and gadolinium-enhanced magnetic resonance imaging (MRI) in a 41-year-old man with diffuse midline glioma, H3K27-altered. (a) Non-contrast axial CT of the brain showing a round isodense mass (double arrow) at the foramen of Monro with hydrocephalus. (b-f) Axial MRI of the brain showing a well-defined solitary intraventricular tumour measuring 2 × 2.3 × 2.7 cm^3 (transverse × anteroposterior × craniocaudal) epicentred at the right lateral ventricle/foramen of Monro (double arrows). It is (b) T1 iso- to hypointense, (c) T2 hyperintense with restricted diffusion with (d) high diffusion-weighted imaging and (e) low apparent diffusion coefficient values. (f) Internal small foci of enhancement (hollow arrow) were seen in the post-contrast T1-weighted images. (g) There was no abnormal susceptibility artefact to suggest calcification or prior haemorrhage. The mass displaced the septum pellucidum (arrow in [c]) to the left while the third ventricle was displaced left and inferiorly. There was no definite suprasellar extension. (h) Coronal T1-weighted post-contrast MRI of the brain showing the mass (double arrow) abutting the right A1 segment of the anterior cerebral artery inferiorly (arrowhead), which remained patent.

2) and H3K27M (Figure 2b), with retained ATRX (alpha-thalassemia/mental retardation, X-linked). Staining for p53 showed a wild-type pattern, while staining for H3K27me3 was lost in tumour cell nuclei. Stainings for epithelial membrane antigen and IDH1 (isocitrate dehydrogenase 1) R132H were negative. The Ki-67 proliferative index was up to 30%. Histone H3 Sanger sequencing detected a mutation of c.83A>T (p.Lys28Met) [K27M] in the *H3F3A* gene. The overall findings were consistent with diffuse midline glioma (DMG), H3K27-altered (grade 4 of the World Health Organization [WHO] Classification of Tumours of the Central Nervous System).

Following discussion with local colleagues, a final diagnosis was made of H3K27-altered DMG. Subsequent workup including MRI of the whole spine (not shown) revealed no spinal cord involvement.

There were limited randomised data and no consensus on treatment for H3K27-altered DMG for the patient. Based on available evidence, resection and chemoradiotherapy with temozolomide was scheduled followed by adjuvant temozolomide if grade 4 disease was confirmed. As expected and considering the presence of infiltration of the basal part, post-resection MRI showed partial resection (Figure 3). Final histology of the resected specimen was similar to the previous biopsy, confirming the diagnosis of a grade-4 H3K27-altered DMG (Figure 2a). Further molecular studies showed no *IDH1* or *IDH2* gene mutation on sequencing and no *MGMT* (O^6-methylguanine-DNA methyltransferase) gene promoter methylation evident on polymerase chain reaction.

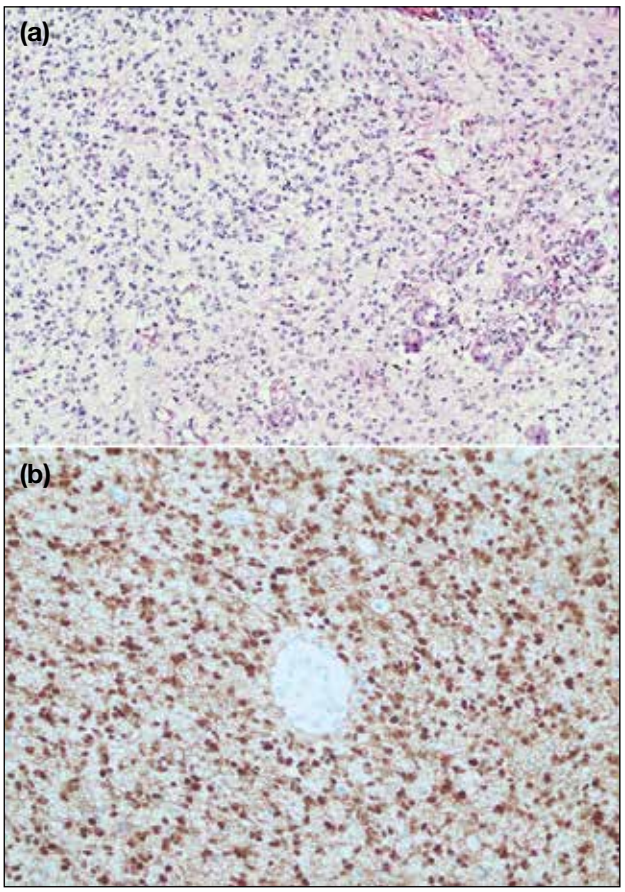

Figure 2. Histopathological and immunohistochemical studies in the same patient with H3K27-altered diffuse midline glioma as in Figure 1. (a) The biopsy and resection specimens of the glial tumour showed moderate to high cellularity with areas of microvascular proliferation. No necrosis was seen. There was no rosette or pseudorosette (hematoxylin and eosin staining, × 100). (b) On immunohistochemical studies, the tumour cells were positive for H3K27M (× 200).

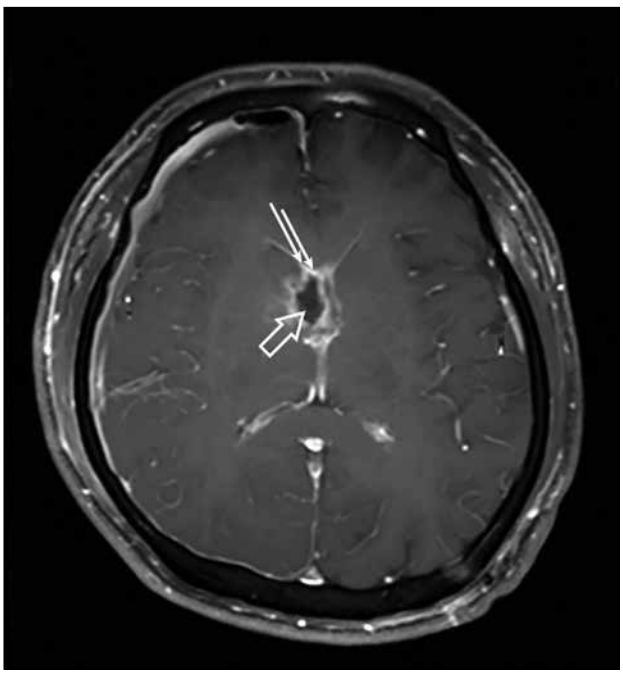

Figure 3. Post-contrast T1-weighted axial magnetic resonance image of the brain 1 week post resection showing possible residual tumour as evidenced by a well-defined solitary intraventricular area measuring 1 × 1.6 × 1.9 cm^3 (transverse × anteroposterior × craniocaudal) epicentred at the right lateral ventricle/foramen of Monro (double arrow). It is T1 iso- to hypointense, T2 hyperintense (not shown) and possibly with tiny internal foci of enhancement (hollow arrow).

Chemoradiotherapy was completed and the patient was scheduled for review with possible subsequent adjuvant chemotherapy.

DISCUSSION

Intraventricular tumours are rare and represent only 0.8% to 1.6% of all intracranial tumours.[1] Most intraventricular tumours are benign and are more common in children than in adults, comprising about 16% of childhood and adolescent intracranial tumours.[1] Common intraventricular tumours include: (1) neoplasm of the choroid plexus, e.g., choroid plexus papillomas, choroid plexus carcinomas, meningioma, and metastases; (2) neoplasm of the ventricular wall and septum pellucidum, e.g., ependymoma, subependymoma, subependymal giant cell astrocytoma, and central neurocytoma; (3) secondary intraventricular tumours, e.g., glioblastoma multiforme; and (4) non-neoplastic lesions, e.g., colloid cysts, arachnoid cysts, ependymal cysts, and choroid plexus cysts.[1] The most common clinical presentations of intraventricular tumours are secondary to hydrocephalus and subsequent increase in intracranial pressure, including headache and vomiting with papilledema in adults.[1]

Patient age, tumour location and imaging features will narrow the list of differential diagnoses. Ependymomas and choroid plexus tumours are more often found in children, and meningiomas and central neurocytoma are more usually seen in adults. Tumours such as central neurocytomas and subependymal giant cell astrocytomas are predominantly found in the anterior aspect of the lateral ventricles, whilst ependymomas and subependymomas are more commonly found in the fourth ventricle.[1]

H3K27M-mutant DMG was included in the 2016 WHO Classification of Tumours of the Central Nervous

System, according to its histological and molecular characteristics. It is usually located in the midline structures. In the 2021 updated guideline, it was renamed 'H3K27-altered'.[2] It is a diffusely infiltrative WHO grade 4 tumour with very poor prognosis and a 5-year survival of < 1%. Patients with H3-mutant DMGs have a significantly shorter overall survival than those with the H3 wild-type.[3] The most common locations at presentation are the brainstem, thalamus, and spinal cord. A study has reported better prognosis for patients with this type of DMG in unusual anatomical locations (e.g., lateral ventricles) compared with those at the typical location (i.e., brainstem).[3] It is a unique entity affecting children and very rarely adults.[4] The average age at presentation of H3K27M-altered DMG is 7 to 11 years.[5] Its presentation in the lateral ventricle is extremely rare with only two reported adult cases.[3,5] It is therefore uncommon to have H3K27-altered DMG in the intraventricular region and occurrence is also rare in adults.

The radiological appearances of H3K27-altered DMG are highly heterogeneous and lack specificity.[4] On MRI, the tumours are typically T1 iso- or hypointense and T2 hyperintense, and signal intensities are homogeneous on fluid-attenuated inversion recovery images. Restricted diffusion can be seen with invasive growth of the tumour. Intratumoural haemorrhage and necrosis are common and ring enhancement of the tumour can be seen although enhancement is usually not significant.[2] A connection between imaging findings and the H3K27-altered histone changes is not known due to the lack of relevant research making the diagnosis by imaging alone difficult.[2]

Due to the intraventricular location of this high-grade tumour, surgical resection is difficult.[2] The management plan for our case was maximal safe surgical resection plus adjuvant radiotherapy. Complete excision was not possible as the disease was quite infiltrative at the basal part.

In summary, we report an extremely rare case of primary lateral ventricle H3K27-altered DMG in a middle-aged man. Its intraventricular location made diagnosis based on imaging findings difficult, with our initial differential diagnoses of subependymoma, ependymoma and central neurocytoma incorrect. Further endoscopic biopsy helped confirm the final diagnosis and the patient underwent resection followed by chemoradiotherapy, and likely subsequent adjuvant chemotherapy. Early biopsy and molecular characterisation are the key to accurate diagnosis and prompt treatment. A high index of suspicion is needed to avoid missing the diagnosis. New clinical, imaging and histopathological information remain to be established but will aid in the diagnosis of this rare disease.

REFERENCES

1. Agarwal A, Kanekar S. Intraventricular tumors. Semin Ultrasound CT MR. 2016;37:150-8.
2. Zhao B, Sun K, Zhang Z, Xu T, Zhao L, Liu C, et al. A rare presentation of primary lateral ventricle H3 K27-altered diffuse midline glioma in a 14-year-old girl: a case description. Quant Imaging Med Surg. 2022;12:5288-95.
3. Wang L, Li Z, Zhang M, Piao Y, Chen L, Liang H, et al. H3 K27M-mutant diffuse midline gliomas in different anatomical locations. Hum Pathol. 2018;78:89-96.
4. Yekula A, Gupta M, Coley N, U HS. Adult H3K27M-mutant diffuse midline glioma with gliomatosis cerebri growth pattern: case report and review of the literature. Int J Surg Case Rep. 2020;68:124-8.
5. Luo Y, Zeng L, Xie XQ, Wang F, Liu YZ, Kang JB, et al. H3K27M mutant diffuse midline glioma: a case report. Eur Rev Med Pharmacol Sci. 2020;24:2579-84.

Hong Kong J Radiol. 2024;27(1):e43-5. Published 3 January 2024 | https://doi.org/10.12809/hkjr2217651

CASE REPORT

Tumour-Induced Osteomalacia: A Case Report

TK Chow, KW Chan, YH Hui, WY Ho

Nuclear Medicine Unit, Department of Radiology, Queen Mary Hospital, Hong Kong SAR, China

INTRODUCTION

Tumour-induced osteomalacia (TIO), also known as oncogenic osteomalacia, is a rare acquired paraneoplastic syndrome. Since the culprit tumour is difficult to localise using conventional anatomical imaging, functional imaging plays an important role in localisation. We present the case of a middle-aged male with TIO who underwent various imaging investigations with failure to localise the culprit tumour, where finally a ^{111}indium-pentetreotide scintigraphy (octreotide scan) located the tumour over his left foot. This case highlights the importance of covering the entire body when performing an octreotide scan in patients with suspected TIO so as not to miss any hidden tumour in the extremities.

CASE PRESENTATION

A 35-year-old man initially presented with right ankle pain. Magnetic resonance imaging revealed a non-traumatic stress fracture of the right distal tibia. One year later, the patient complained of increasing bone and joint pain. Bone scintigraphy, performed at an external centre, revealed multiple fractures of the ribs, bony pelvis and extremities, along with features of metabolic bone disease (Figure 1).

Biochemically, the patient was found to have a hypophosphataemia level of 0.48 mmol/L (normal range: 0.75-1.3) and an elevated alkaline phosphatase level of 852 U/L (normal range: 50-136). Further workup revealed normal calcium level of 2.28 mmol/L (normal range: 2.11-2.55) and parathyroid hormone level of 4.4 pmol/L (normal range: 1.6-6.9), low 1,25-dihydroxyvitamin D level of 4.9 pg/mL (normal range: 19.6-54.3), and elevated fibroblast growth factor 23 (FGF23) level of 252 RU/mL (normal range: <180). A presumptive diagnosis of TIO was made in view of his typical symptoms and biochemical profile. An extensive search for the culprit tumour by various imaging modalities was performed. Whole-body magnetic resonance imaging, octreotide scan (from vertex to mid-thigh) and ^{18}F-fluorodeoxyglucose positron emission tomography/computed tomography (PET/CT) [from vertex to thigh] performed at external centres showed no suspicious lesion that could indicate TIO.

Two years later, the patient self-detected a lump over the first web space of his left foot. Contrast CT revealed a well-circumscribed lobulated isodense mass with avid heterogenous contrast enhancement at the first web

Correspondence: *Dr TK Chow, Nuclear Medicine Unit, Department of Radiology, Queen Mary Hospital, Hong Kong SAR, China*
Email: ctk594@ha.org.hk

Submitted: 12 Oct 2022; Accepted: 13 Dec 2022.

Contributors: TKC designed the study, acquired and analysed the data, and drafted the manuscript. KWC, YHH and WYH critically revised the manuscript for important intellectual content. All authors had full access to the data, contributed to the study, approved the final version for publication, and take responsibility for its accuracy and integrity.

Conflicts of Interest: All authors have disclosed no conflicts of interest.

Funding/Support: This study received no specific grant from any funding agency in the public, commercial, or not-for-profit sectors.

Data Availability: All data generated or analysed during the present study are available from the corresponding author on reasonable request.

Ethics Approval: The patient was treated in accordance with the Declaration of Helsinki and provided informed consent for all procedures, and for publication of this case report.

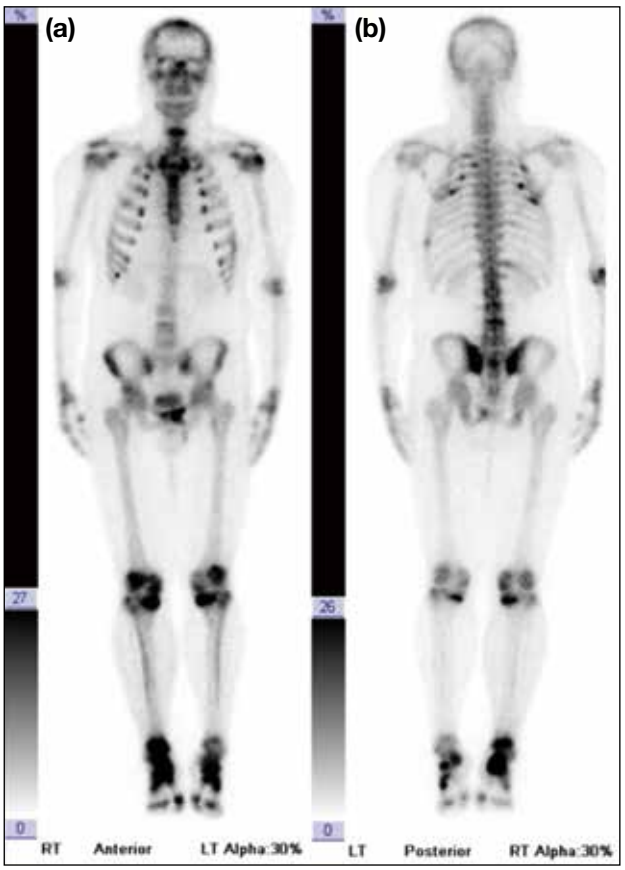

Figure 1. (a) Anterior and (b) posterior images of whole-body planar bone scintigraphy showing multiple fractures at bilateral ribs, pubic bones and lower limbs with features of metabolic bone disease, including diffusely increased tracer uptake in both axial and appendicular skeleton, as well as the presence of a hot sternum tie sign and rickety rosary beading at the costochondral junctions.

space. The nature of the lesion was non-specific but it was suspected to be the cause of TIO. The patient was then referred to our centre where whole-body octreotide scan revealed an octreotide-avid soft tissue mass at the first web space of the left foot. In the absence of any other suspicious lesion (Figure 2), this confirmed it to be the culprit tumour.

Subsequently, surgical resection of the tumour in the left foot was performed. Histological diagnosis revealed a phosphaturic mesenchymal tumour composed of spindle to short oval cells arranged in irregular bundles, characterised by a rich vasculature and mildly irregular or twisted outline with indistinct nucleoli. The phosphate level normalised 3 weeks after the surgery.

DISCUSSION

TIO is caused by a small benign tumour, most commonly classified histopathologically as phosphaturic mesenchymal tumour, mixed connective tissue type.[1] The tumour will secrete FGF23, a phosphaturic hormone that leads to inhibition of renal phosphate reabsorption. FGF23 also reduces the production of 1,25-dihydroxyvitamin D.[2] Eventually, these will result in hypophosphataemia.

Patients with TIO present with muscle weakness, bone pain, and multiple fractures.[3] Characteristic biochemical features are hypophosphataemia and hyperphosphaturia. Other common biochemical features include normal calcium, parathyroid hormone and low-to-normal 1,25-dihydroxyvitamin D level, and elevated alkaline phosphatase and FGF23 level.[3] Nonetheless the non-specific nature of the symptoms often leads to underdiagnosis with a consequent delay in management, often years after initial presentation.[1]

With a consistent clinical history and typical biochemical features establishing the diagnosis of TIO, localisation of the culprit tumour is the next important step in management. Nonetheless this often presents another major challenge that delays curative treatment. The culprit tumour is typically small and can present anywhere in the body but more commonly in the lower extremities or craniofacial region.[4-6] There is no specific pattern or pathognomonic feature of the culprit tumour on conventional anatomical imaging,[1] rendering tumour localisation difficult.

Culprit tumours of TIO frequently express somatostatin receptors (SSTR), evidenced by avid uptake on somatostatin analogue imaging.[3] Therefore, ^{111}In-octreotide scintigraphy and ^{68}Ga-DOTA–conjugated SSTR-targeting peptide PET/CT (SSTR PET/CT) are useful for tumour localisation. Due to possibly obscure locations of culprit tumours, they are easily missed if a whole-body scan is not performed. Whenever a patient is suspected to have TIO, it is vital to ensure that the entire body is included in the scan range so as not to miss any hidden tumour in the extremities or craniofacial region.

In recent years, SSTR PET/CT imaging has gained popularity due to its lower radiation exposure, shorter acquisition time, and improved spatial resolution compared with ^{111}In-octreotide scintigraphy.[7,8] Previous studies have shown that SSTR PET/CT imaging exhibits the highest sensitivity and specificity among different functional imaging studies for localising the culprit tumour of TIO.[8,9] A recent systematic review and

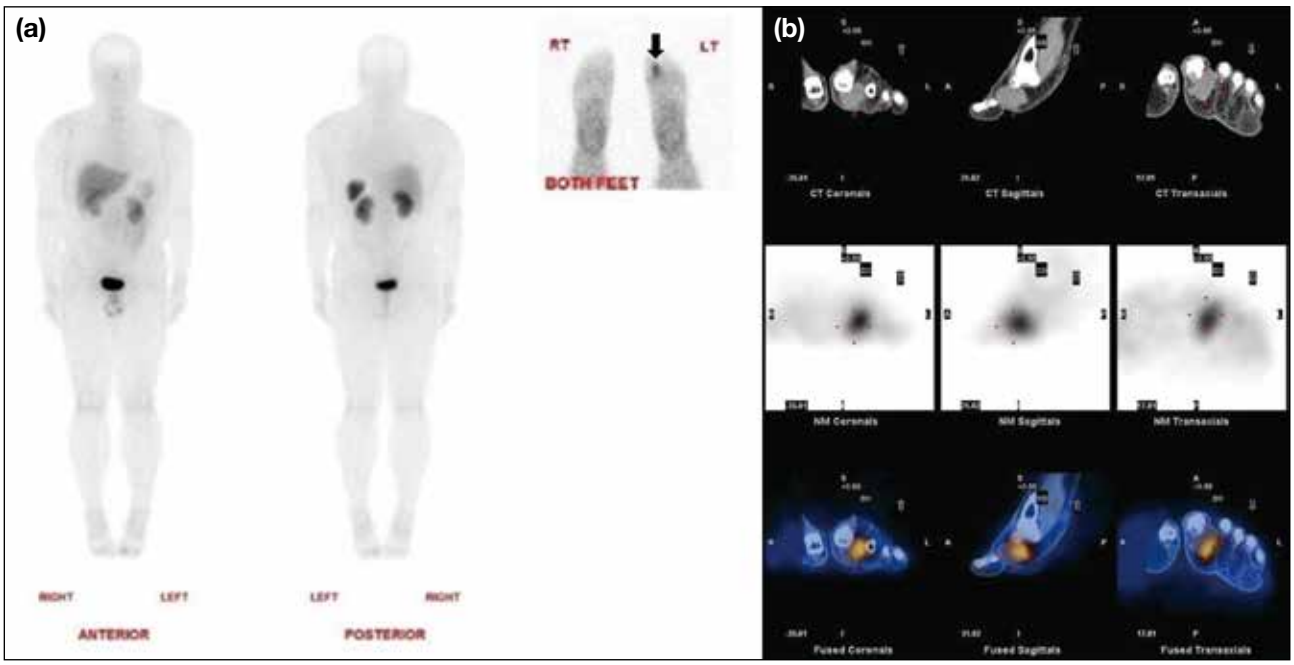

Figure 2. (a) Anterior (left) and posterior (right) view of whole-body planar image of ^{111}In-octreotide scintigraphy showed an octreotide-avid lesion at the left foot (arrow). (b) Single-photon emission computed tomography/computed tomography showing an octreotide-avid soft tissue lesion at the first web space of the left foot.

meta-analysis showed a pooled detection rate of 87.6% for culprit tumour localisation using SSTR PET/CT imaging.[10]

Definitive treatment for TIO is surgical resection of the culprit tumour. This usually results in rapid resolution of hypophosphataemia.[1]

CONCLUSION

TIO is a rare but devastating disease. One of the major challenges is localisation of the culprit tumour and subsequent curative surgical resection. Somatostatin analogue imaging, including ^{111}In-octreotide scintigraphy and ^{68}Ga-DOTA-SSTR PET/CT, is useful in localising the culprit tumour. It is worth noting that coverage of the entire body in the scan range is mandatory to avoid missing any hidden tumour in the extremities.

REFERENCES

1. Jan de Beur SM. Tumor-induced osteomalacia. JAMA. 2005;294:1260-7.
2. Hendry DS, Wissman R. Case 165: oncogenic osteomalacia. Radiology. 2011;258:320-2.
3. Dahir K, Zanchetta MB, Stanciu I, Robinson C, Lee JY, Dhaliwal R, et al. Diagnosis and management of tumor-induced osteomalacia: perspectives from clinical experience. J Endocr Soc. 2021;5:bvab099.
4. Chong WH, Molinolo AA, Chen CC, Collins MT. Tumor-induced osteomalacia. Endocr Relat Cancer. 2011;18:R53-77.
5. Zhang J, Zhu Z, Zhong D, Dang Y, Xing H, Du Y, et al. ^{68}Ga DOTATATE PET/CT is an accurate imaging modality in the detection of culprit tumors causing osteomalacia. Clin Nucl Med. 2015;40:642-6.
6. Chong WH, Andreopoulou P, Chen CC, Reynolds J, Guthrie L, Kelly M, et al. Tumor localization and biochemical response to cure in tumor-induced osteomalacia. J Bone Miner Res. 2013;28:1386-98.
7. Hofman MS, Lau WF, Hicks RJ. Somatostatin receptor imaging with ^{68}Ga DOTATATE PET/CT: clinical utility, normal patterns, pearls, and pitfalls in interpretation. Radiographics. 2015;35:500-16.
8. El-Maouche D, Sadowski SM, Papadakis GZ, Guthrie L, Cottle-Delisle C, Merkel R, et al. ^{68}Ga-DOTATATE for tumor localization in tumor-induced osteomalacia. J Clin Endocrinol Metab. 2016;101:3575-81.
9. Breer S, Brunkhorst T, Beil FT, Peldschus K, Heiland M, Klutmann S, et al. ^{68}Ga DOTA-TATE PET/CT allows tumor localization in patients with tumor-induced osteomalacia but negative ^{111}In-octreotide SPECT/CT. Bone. 2014;64:222-7.
10. Meyer M, Nicod Lalonde M, Testart N, Jreige M, Kamani C, Boughdad S, et al. Detection rate of culprit tumors causing osteomalacia using somatostatin receptor PET/CT: systematic review and meta-analysis. Diagnostics (Basel). 2020;10:2.

Hong Kong J Radiol. 2024;27(1):e46-50. Published 7 March 2024 | https://doi.org/10.12809/hkjr2217603

CASE REPORT

[^{18}F]Fluorodeoxyglucose Positron Emission Tomography/Computed Tomography Findings in Anti–Gamma-Aminobutyric Acid B Receptor Encephalitis: A Case Report

KL Chiu, WH Ma, KM Ma

Department of Radiology and Nuclear Medicine, Tuen Mun Hospital, Hong Kong SAR, China

INTRODUCTION

Encephalitis is a severe inflammatory disorder of the brain that develops as a rapidly progressive encephalopathy and may affect patients of all ages.[1] Autoimmune encephalitis, which is the most common cause of non-infectious encephalitis[2] characterised by the presence of autoantibodies against different neuronal targets, may be associated with various cancers. Anti–gamma-aminobutyric acid B (anti-$GABA_B$) receptor encephalitis is a relatively uncommon entity. Very few have been reported in findings on [^{18}F]fluorodeoxyglucose positron emission tomography/computed tomography ([^{18}F]FDG PET/CT) and its role in diagnosis and management.[3] We present a patient with anti-$GABA_B$ receptor encephalitis who underwent [^{18}F]FDG PET/CT.

CASE PRESENTATION

A 79-year-old man with a history of hypertension, diabetes mellitus, hyperlipidaemia and gout was admitted for status epilepticus. He had no known history of epilepsy or malignancy and presented with a history of gradual onset slurring of speech and generalised weakness over a few days, followed by repeated seizures and status epilepticus on the day of admission. Cerebrospinal fluid findings following lumbar puncture were not suggestive of infection. Electroencephalogram revealed mild slowing background with excessive slow wave; epileptiform discharge was not detected. CT of the brain revealed no acute intracranial haemorrhage but a hyperdense lesion at the left frontal lobe, suspicious of brain tumour (Figure 1).

Magnetic resonance imaging (MRI) of the brain performed 4 days after admission revealed a small enhancing intra-axial lesion in the left frontal lobe with restricted diffusion and perilesional oedema, likely representing a tumour. Slightly increased fluid-attenuated inversion recovery (FLAIR) signal was also evident in the right hippocampus, suspected to be related to convulsion (Figure 2).

Tumour marker testing revealed elevated carcinoembryonic antigen level at 14.4 ug/L

Correspondence: *Dr KL Chiu, Department of Radiology and Nuclear Medicine, Tuen Mun Hospital, Hong Kong SAR, China*
Email: klchiu@ha.org.hk

Submitted: 4 July 2022; Accepted: 5 September 2022.

Contributors: KLC designed the study, acquired and analysed the data, and drafted the manuscript. WHM and KMM critically revised the manuscript for important intellectual content. All authors had full access to the data, contributed to the study, approved the final version for publication, and take responsibility for its accuracy and integrity.

Conflicts of Interest: All authors have disclosed no conflicts of interest.

Funding/Support: This study received no specific grant from any funding agency in the public, commercial, or not-for-profit sectors.

Data Availability: All data generated or analysed during the present study are available from the corresponding author on reasonable request.

Ethics Approval: The study was approved by the Central Institutional Review Board of Hospital Authority, Hong Kong (Ref No.: CIRB-2023-175-1). The patient was treated in accordance with the Declaration of Helsinki. The requirement for patient consent was waived by the Board due to the use of anonymised patient data.

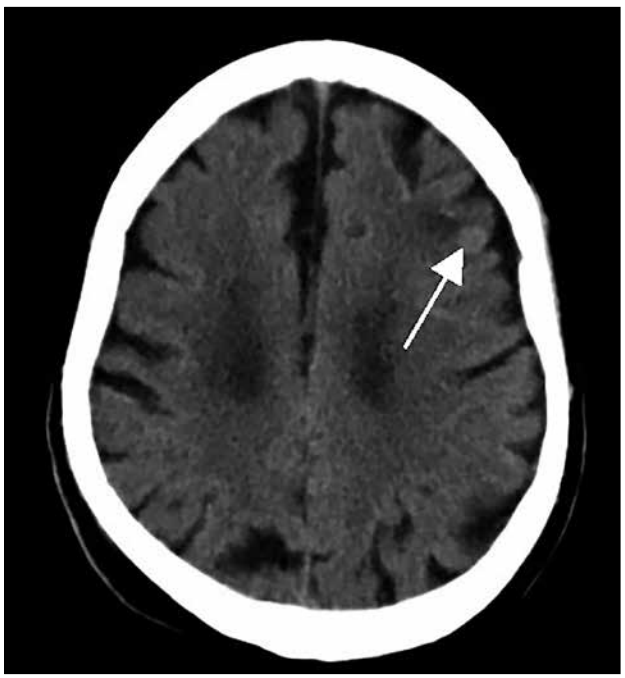

Figure 1. Computed tomography of the brain showing left frontal lesion (arrow).

(reference interval, ≤ 5.0). Paraneoplastic markers (anti-Hu/Yo/Ri) were negative. Autoimmune markers (anti–NMDA [N-methyl-D-aspartate] receptor, anti-CASPR2 [contactin-associated protein-like 2], anti-AMPA1/2 [alpha-amino-3-hydroxy-5-methyl-4-isoxazolepropionic acid 1/2], anti-LGI1 [leucine-rich-glioma-inactivated 1] and anti-DPPX [dipeptidyl-peptidase-like protein 6] antibodies) were negative except anti-$GABA_{B1}$/ anti-$GABA_{B2}$ receptors that were positive. MRI of the brain was repeated 1 month after admission and revealed the increased FLAIR signal at the right hippocampus to have become slightly more conspicuous (Figure 3).

[^{18}F]FDG PET/CT was performed the day after the second MRI of the brain. A hypermetabolic lung mass was found in the apicoposterior segment of the left upper lobe as well as multiple hypermetabolic mediastinal, hilar and cervical lymph nodes (Figure 4). Findings raised suspicion of an underlying primary lung tumour with multiple nodal metastases. Focal hypermetabolism observed in the right hippocampus was consistent with limbic encephalitis. Nonetheless no overt hypermetabolism was observed in the left frontal lobe brain lesion (Figure 5).

The patient underwent plasmapheresis with substantial improvement in neurological symptoms. Incisional biopsy of the right submandibular cervical lymph node confirmed small-cell lung carcinoma. Chemotherapy and radiotherapy were planned, but the patient developed a severe hospital-acquired chest infection and sepsis with rapid deterioration of his condition despite antibiotics. Oncological treatment was suspended and the patient eventually succumbed.

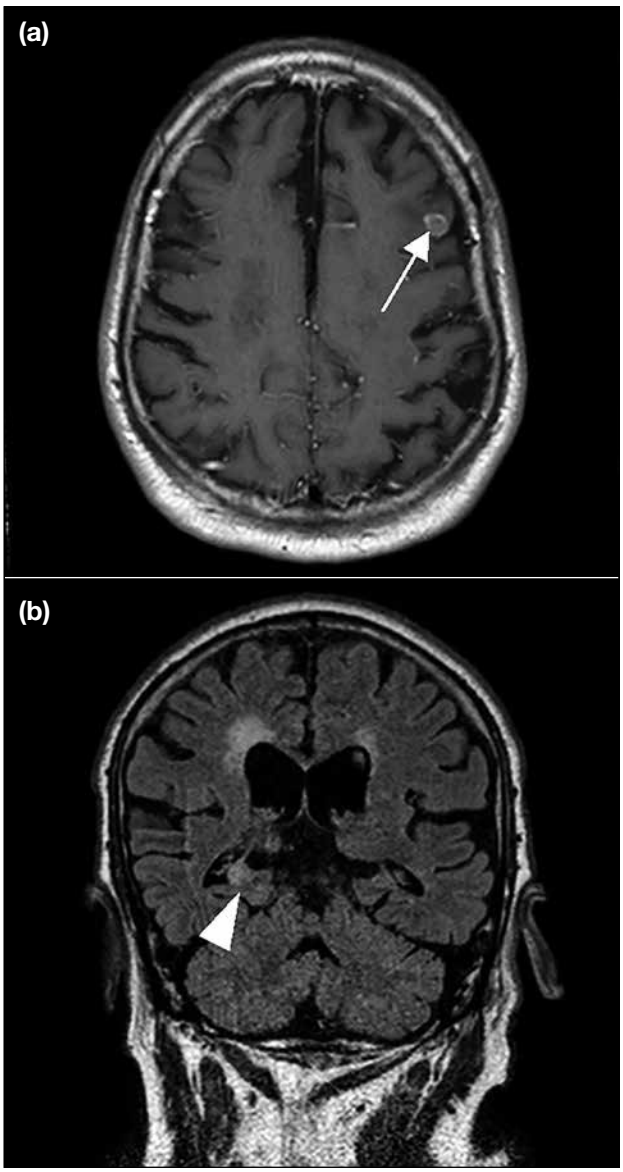

Figure 2. Magnetic resonance imaging of the brain 4 days after admission. (a) T1-weighted image with contrast demonstrating an enhancing left frontal lobe lesion likely representing a tumour (arrow). (b) Coronal fluid-attenuated inversion recovery image demonstrating slightly increased signal at the right hippocampus (arrowhead) suspected to be related to convulsion.

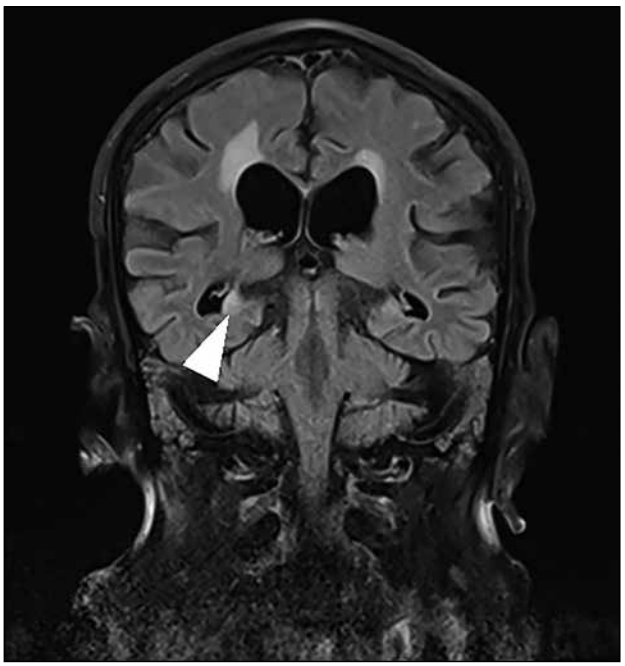

Figure 3. Magnetic resonance imaging of the brain 1 month after admission. The increased fluid-attenuated inversion recovery signal at the right hippocampus had become slightly more conspicuous (arrowhead).

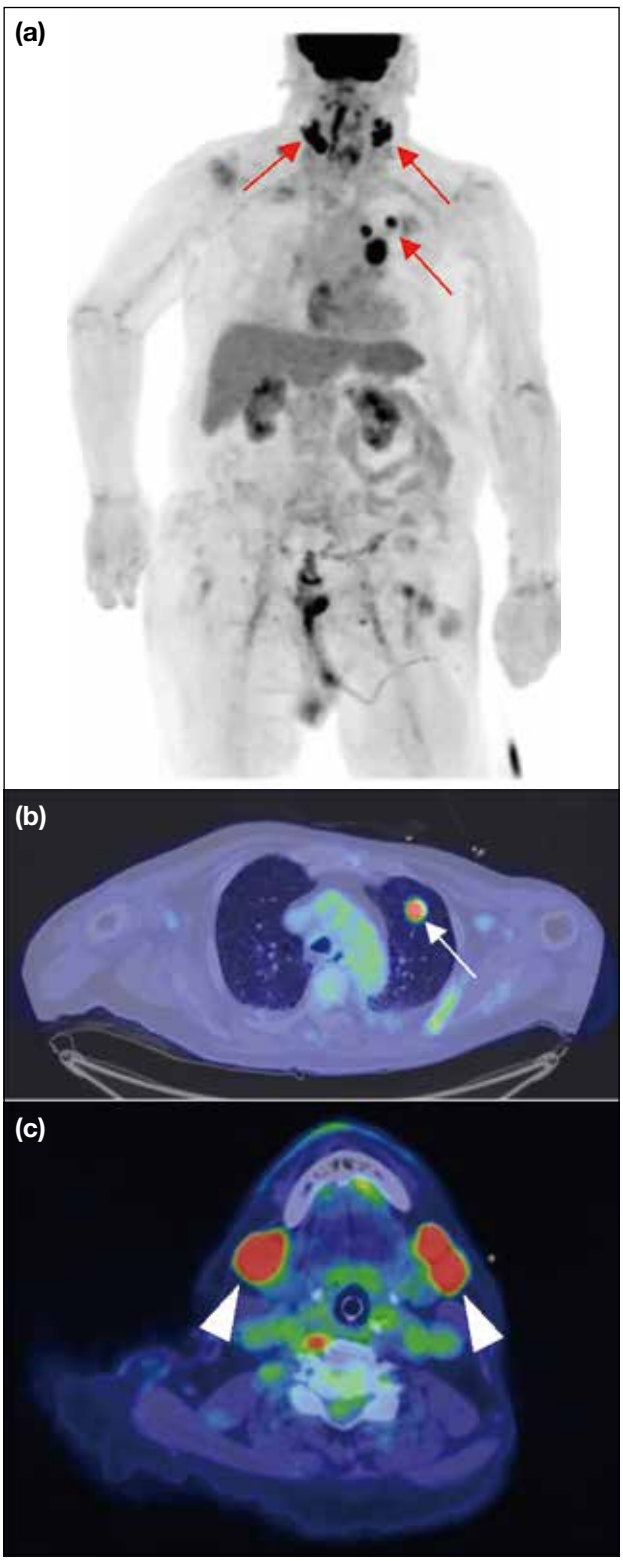

Figure 4. [^{18}F]fluorodeoxyglucose positron emission tomography/computed tomography of the body. (a) Maximum intensity projection image demonstrating hypermetabolic left upper lobe lung mass with suspected mediastinal, hilar and bilateral cervical nodal metastases (red arrows). (b) Fusion image of the left upper lobe lung mass (white arrow). (c) Fusion image of suspected bilateral submandibular nodal metastases (arrowheads) later biopsy proven to be small-cell lung carcinoma.

DISCUSSION

According to the diagnostic criteria of autoimmune encephalitis proposed by Graus et al,[1] the diagnosis of anti-GABA$_B$ receptor encephalitis could be established in the patient presented here. Autoimmune encephalitis is an emerging neurological disease associated with neuronal autoantibodies against various neuronal targets. Encephalitis with autoantibodies against GABA$_B$ receptors is an uncommon entity with an estimated relative frequency of 5%.[4] GABA receptors play an important role in neuronal activity associated with learning, memory and cognitive functions[5] and have been found to cause limbic encephalitis.[6]

Limbic encephalitis refers to inflammation of the limbic system and is considered a classic paraneoplastic syndrome. Common malignancies associated with limbic encephalitis include lung tumours (especially small-cell lung cancer), seminoma, thymoma, breast cancer, and lymphoma. Patients with limbic encephalitis typically present with memory loss, confusion, hallucinations, personality change, and seizures. Prompt diagnosis and management are essential for neurological recovery. Nevertheless the initial diagnostic tests currently utilised are mainly cerebrospinal fluid analysis,

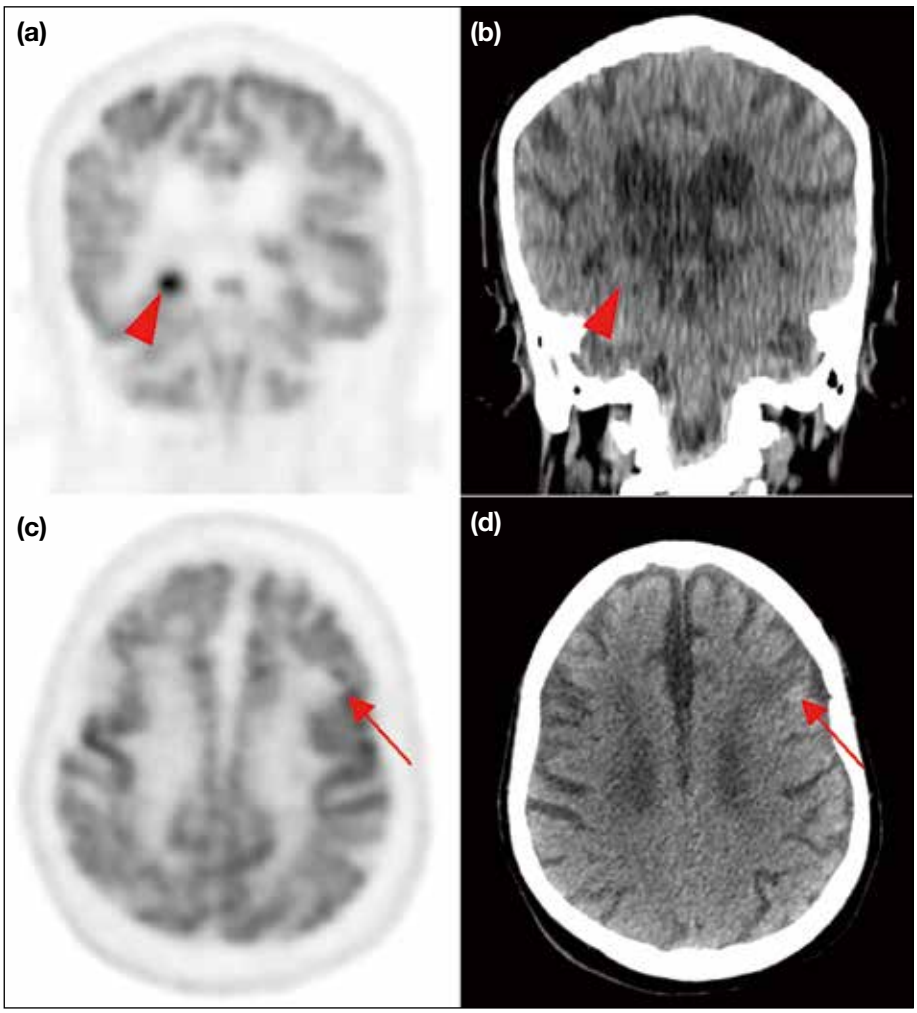

Figure 5. [^{18}F]fluorodeoxyglucose positron emission tomography/computed tomography of the brain. (a, b) Focal hypermetabolism in the right hippocampus consistent with limbic encephalitis (arrowheads). (c, d) No overt hypermetabolism was observed in the left frontal lobe lesion (arrows).

electroencephalogram, and MRI of the brain.[1] The role of [^{18}F]FDG PET/CT remains unclear, despite being a sensitive functional brain imaging technique. Baumgartner et al[7] reported a higher sensitivity of [^{18}F]FDG PET/CT in detecting limbic encephalitis–associated pathological findings than MRI. [^{18}F]FDG PET/CT offers information on the neuronal metabolic activity that increases in the presence of brain inflammation. In the case we present, the FLAIR signal abnormality was very subtle on MRI of the brain.

According to a case series by Höftberger et al,[8] 50% of patients had small-cell lung carcinoma. They also demonstrated that a patient may have neurological improvement with oncological treatment alone. Therefore, the clinical outcome for patients with anti-$GABA_B$ receptor encephalitis and underlying small-cell lung carcinoma is dictated by successful treatment of the tumour. [^{18}F]FDG PET/CT is also a sensitive oncological diagnostic tool in addition to functional brain imaging. Our patient underwent [^{18}F]FDG PET/CT following equivocal results of other investigations and consequent diagnosis weeks after initial presentation. Unfortunately, our patient succumbed and was not able to receive timely oncological treatment. We suggest that incorporation of [^{18}F]FDG PET/CT in the initial assessment may benefit the diagnosis and subsequent initiation of oncological treatment in patients with underlying tumour as well as their clinical outcome.

REFERENCES

1. Graus F, Titulaer MJ, Balu R, Benseler S, Bien CG, Cellucci T, et al. A clinical approach to diagnosis of autoimmune encephalitis. Lancet Neurol. 2016;15:391-404.
2. Granerod J, Ambrose HE, Davies NW, Clewley JP, Walsh AL, Morgan D, et al. Causes of encephalitis and differences in their clinical presentations in England: a multicentre, population-based prospective study. Lancet Infect Dis. 2010;10:835-44.

3. Bordonne M, Chawki MB, Doyen M, Kas A, Guedj E, Tyvaert L, et al. Brain 18F-FDG PET for the diagnosis of autoimmune encephalitis: a systematic review and a meta-analysis. Eur J Nucl Med Mol Imaging. 2021;48:3847-58.
4. Lancaster E, Martinez-Hernandez E, Dalmau J. Encephalitis and antibodies to synaptic and neuronal cell surface proteins. Neurology. 2011;77:179-89.
5. Collingridge GL, Isaac JT, Wang YT. Receptor trafficking and synaptic plasticity. Nat Rev Neurosci. 2004;5:952-62.
6. Lancaster E, Lai M, Peng X, Hughes E, Constantinescu R, Raizer J, et al. Antibodies to the GABAB receptor in limbic encephalitis with seizures: case series and characterisation of the antigen. Lancet Neurol. 2010;9:67-76.
7. Baumgartner A, Rauer S, Mader I, Meyer PT. Cerebral FDG-PET and MRI findings in autoimmune limbic encephalitis: correlation with autoantibody types. J Neurol. 2013;260:2744-53.
8. Höftberger R, Titulaer MJ, Sabater L, Dome B, Rózsás A, Hegedus B, et al. Encephalitis and GABAB receptor antibodies: novel findings in a new case series of 20 patients. Neurology. 2013;81:1500-6.

Hong Kong J Radiol. 2024;27(1):e51-64. Published 22 March 2024 | https://doi.org/10.12809/hkjr2217677

PICTORIAL ESSAY

Pathologies and Postoperative Features of Posterior Tibial Tendon Dysfunction: A Pictorial Essay

RYS Mak, JHM Cheng, KH Chin, CY Chu

Department of Radiology, Pamela Youde Nethersole Eastern Hospital, Hong Kong SAR, China

INTRODUCTION

The posterior tibial tendon (PTT) is the largest tendon in the medial compartment of the ankle and the most important dynamic stabiliser of the longitudinal foot arch.[1] It is also the most common site of tendon abnormalities in the medial ankle, where dysfunction would result in a cascade of failures of other secondary supporting structures, eventually leading to collapse of the longitudinal arch and acquired pes planus deformity.[1] Knowledge of the imaging appearance of posterior tibial tendon dysfunction (PTTD) enables early diagnosis and treatment, hence preventing progression to fixed pes planus deformity.

ANATOMY AND PATHOPHYSIOLOGY

The PTT runs posterior to the medial malleolus and inserts mainly on the medial aspect of the navicular, with minor slips inserting into the cuneiforms and the first to fourth metatarsals.[1] As the tendon passes posterior to the axis of the ankle joint and medial to the subtalar joint, it acts as a plantar flexor and invertor of the foot, as well as the adductor of the forefoot at the midtarsal joint.[2-4]

PTTD is a spectrum of pathologies ranging from tenosynovitis, tendonitis, and partial tear to complete rupture.[5] It is most prevalent in middle- to old-aged females,[5] commonly resulting from chronic degeneration but may also be caused by acute trauma or by conditions with alterations of anatomy, mechanical forces, and tendon vascularity. Risk factors include pre-existing pes planus, obesity, hypertension, chronic steroid use, gout, and inflammatory arthropathies such as rheumatoid arthritis.[3,6] Ischaemia and mechanical stress are the main underlying pathophysiologies of most PTTD.[6] In particular, the PTT around the level of the medial malleolus is the most susceptible site due to a number of factors.[6] First, the mid tendon has relatively poor vascular supply; second, the synovial sheath ends at the midportion of the talus, distal to which the mesotendon

Correspondence: *Dr RYS Mak, Department of Radiology, Pamela Youde Nethersole Eastern Hospital, Hong Kong SAR, China*
Email: mys877@ha.org.hk

Submitted: 18 November 2022; Accepted: 13 March 2023.

Contributors: All authors designed the study. RYSM and JHMC acquired and analysed the data. RYSM, JHMC and KHC drafted the manuscript. JHMC, KHC and CYC critically revised the manuscript for important intellectual content. All authors had full access to the data, contributed to the study, approved the final version for publication, and take responsibility for its accuracy and integrity.

Conflicts of Interest: All authors have disclosed no conflicts of interest.

Funding/Support: The study received no specific grant from any funding agency in the public, commercial, or not-for-profit sectors.

Data Availability: All data generated or analysed during the present study are available from the corresponding author on reasonable request.

Declaration: Part of the study was previously presented as a poster in the 30th Annual Scientific Meeting of Hong Kong College of Radiologists (12-13 November 2022, virtual).

Ethics Approval: The study was approved by the Hong Kong East Cluster Research Ethics Committee of Hospital Authority, Hong Kong (Ref No.: HKECREC-2022-043). The patients were treated in accordance with the tenets of the Declaration of Helsinki. The requirement for patient consent was waived by the Committee due to the retrospective and descriptive nature of the study.

is absent; third, the PTT curves around the medial malleolus, creating a focal point of mechanical strain.[6] The second most common location for tears is at the distal portion of the tendon.[6]

In PTTD, the tendon's normal antagonist, the peroneus brevis, acts as a deforming factor in foot eversion, leading to hindfoot valgus and forefoot varus deformities. Progression to arch collapse is associated with tension on the spring and deltoid ligaments and the talonavicular capsule. Hindfoot valgus also leads to an eversion force of the Achilles tendon on the calcaneus, leading to equinus deformity due to shortening of this tendon.[2,4,7-9]

CLASSIFICATION

Johnson and Strom's four-stage classification is a widely adopted clinical staging system for PTTD, which serves as a guide to management.[10] The clinical findings and corresponding magnetic resonance imaging (MRI) features of PTTD are described in the Table.[10-12]

PRIMARY IMAGING FINDINGS

Tenosynovitis

Tenosynovitis can be caused by mechanical trauma or inflammatory arthropathy such as seronegative spondyloarthropathies, rheumatoid arthritis, systemic lupus erythematosus, and gout.[3,6,13] Tenosynovitis manifests radiologically as an abnormal amount of fluid in the tendon sheath on both MRI and ultrasound (Figures 1 and 2). The tendon itself appears normal at this early stage with normal size and signal intensity on MRI.[5] On ultrasound, increased flow in the peritendon area and hypoechoic tissue around the tendon may be detected.[14]

Tendinosis

The next phase of the disease is tendinosis, with collagen degeneration, local necrosis, calcification, and hypocellularity.[6] On MRI, the normal PTT should appear black on all spin-echo images[5] and is about twice the size of the adjacent round flexor digitorum longus (FDL) and flexor hallucis longus tendons.[1] In posterior tibial tendinosis, the tendon appears thickened with normal or increased signal intensity on both T1- and proton density–weighted images (Figure 3); these intrasubstance signals represent severe degeneration or intrasubstance tears not reaching the tendon surface, thus there is a certain degree of overlap of the appearance of tendinosis and partial tear.[5] Contrast enhancement of the tendon is also a common finding in tendinosis.[14]

On sonography, the PTT normally shows homogeneous echogenic longitudinal fibres with no tendinous or peritendinous vascularity.[14] In tendinosis, the tendon is enlarged and appears inhomogeneous, with internal vascular flow sometimes detected on Doppler examination (Figure 4).[14]

Table. Clinical staging and corresponding magnetic resonance imaging findings for posterior tibial tendon dysfunction.[10-12]

Stage	PTT and foot pathology	MRI findings
I	• Inflamed PTT • Intact longitudinal foot arch	• PTT tenosynovitis, low-grade tendinosis
II	• Degenerated, elongated, and dysfunctional PTT • Reversible/flexible pes planus deformity • Subclassification on weight-bearing radiography: (a) minimal forefoot abduction and < 50% uncovering of talar head (b) significant forefoot abduction and > 50% uncovering of talar head (c) forefoot varus with concomitant stage 2a/b deformity	• PTT tendinosis ± low-grade partial tear ± tenosynovitis • Spring ligament abnormality • Hindfoot valgus
III	• Degenerated ± torn PTT and non-functional PTT • Subtalar joint osteoarthritis • Hindfoot valgus • Rigid/fixed pes planus deformity	• High-grade PTT tear ± tenosynovitis • Spring and tibiospring ligamentous abnormalities • Talar head uncoverage • Hindfoot valgus • Early talocalcaneal ± calcaneofibular impingement • Subtalar joint osteoarthritis
IV	Stage III findings with additional: • Irreversible osteoarthrosis of ankle and midfoot • Fixed hindfoot valgus	Above findings with additional: • Deltoid sprain • Tibiotalar and subtalar osteoarthritis • Talocalcaneal and calcaneofibular impingement

Abbreviations: MRI = magnetic resonance imaging; PTT = posterior tibial tendon.

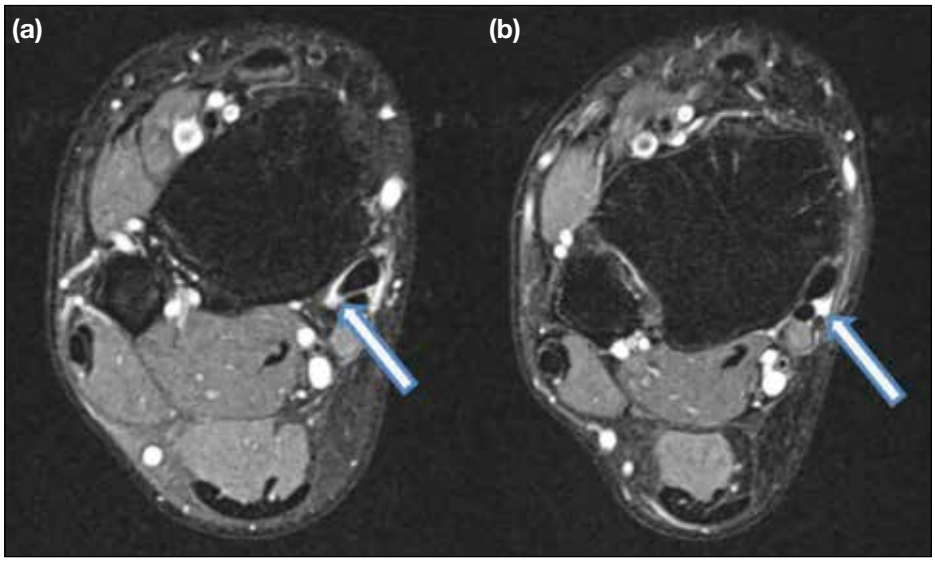

Figure 1. A 25-year-old man with known seronegative spondyloarthropathy complained of right ankle pain. (a, b) Axial fat-saturated proton density–weighted magnetic resonance images showing mild tenosynovial effusion along the posterior tibial tendon (arrows), suggestive of mild tenosynovitis. There was also Achilles tendinosis (not shown). His symptoms improved after starting on golimumab.

Partial and Complete Tears

In chronic tenosynovitis or tendinosis, the PTT is weakened, and tears of the tendon can occur. They can be classified into three types according to Rosenberg et al.[15] Type 1 is a partial tear with associated tendon hypertrophy. On MRI, the tendon is thickened, appearing rounded with loss of its normal oval shape and shows increased linear or heterogenous intrasubstance signal in all sequences, which represents internal tears (Figure 5).[5] A severe form of this type of injury is a longitudinal split of the PTT into two separate parts, which together with the adjacent FDL and flexor hallucis longus tendons, give rise to the appearance of four medial ankle tendons, known as the four-tendon sign (Figure 6a-c).[13] Type 2 is a more severe partial tear with reduced tendon calibre and further increase in internal signal.[5] The segment proximal and distal to the segment of thinned tendon is frequently hypertrophied, which may be due to the background chronic type 1 injury.[5,13] Type 3 injury is a complete tear characterised by a visible gap in the tendon within the tendon sheath (Figure 7).[5]

SECONDARY AND ASSOCIATED IMAGING FINDINGS

Accessory Navicular Bones

There are three types of accessory navicular bones. Type I is a 2- to 3-mm sesamoid bone in the PTT separated from the navicular bone; type II is connected to the navicular bone by a thin layer of cartilage (Figures 6d-e and 8a); type III is a prominent protuberance fused with the navicular tuberosity (Figure 5e).[3] Types II and III may be associated with a younger onset of midfoot pain and planovalgus foot,[3] which are associated with a more proximal insertion of the PTT, straightening the distal tendon curve.[6,16] As a result, there is more focal frictional wear and tear on the tendon at the medial malleolus.[6,16]

MRI features include bone marrow oedema in the accessory navicular bone and the adjacent tuberosity (Figures 6d-e and 8a), fluid in the synchondrosis, soft tissue swelling, adventitial bursa formation, and fracture of the synchondrosis from the chronic pulling of the PTT.[3,6]

Tibial Spur

Osteophytes may develop at the posteromedial aspect of the medial malleolus adjacent to the tendon, presumably due to reactive periostitis in chronic tears (Figure 5j-l).[5,15]

Spring Ligament Injury

As the PTT weakens, it fails to invert the hindfoot and lock the transverse tarsal joints, causing the force of the gastrocnemius-soleus muscle complex to act at the talonavicular joint rather than the metatarsal joints.[17] This leads to increased stress on the talar head and injury to the spring ligament.[17] On MRI, insufficiency of the spring ligament is characterised by thickening (> 6 mm) and increased signal heterogeneity on proton density–weighted images (Figures 5g-i and 6f).[18]

Sinus Tarsi Syndrome

Increased plantar flexion of the talus and hindfoot

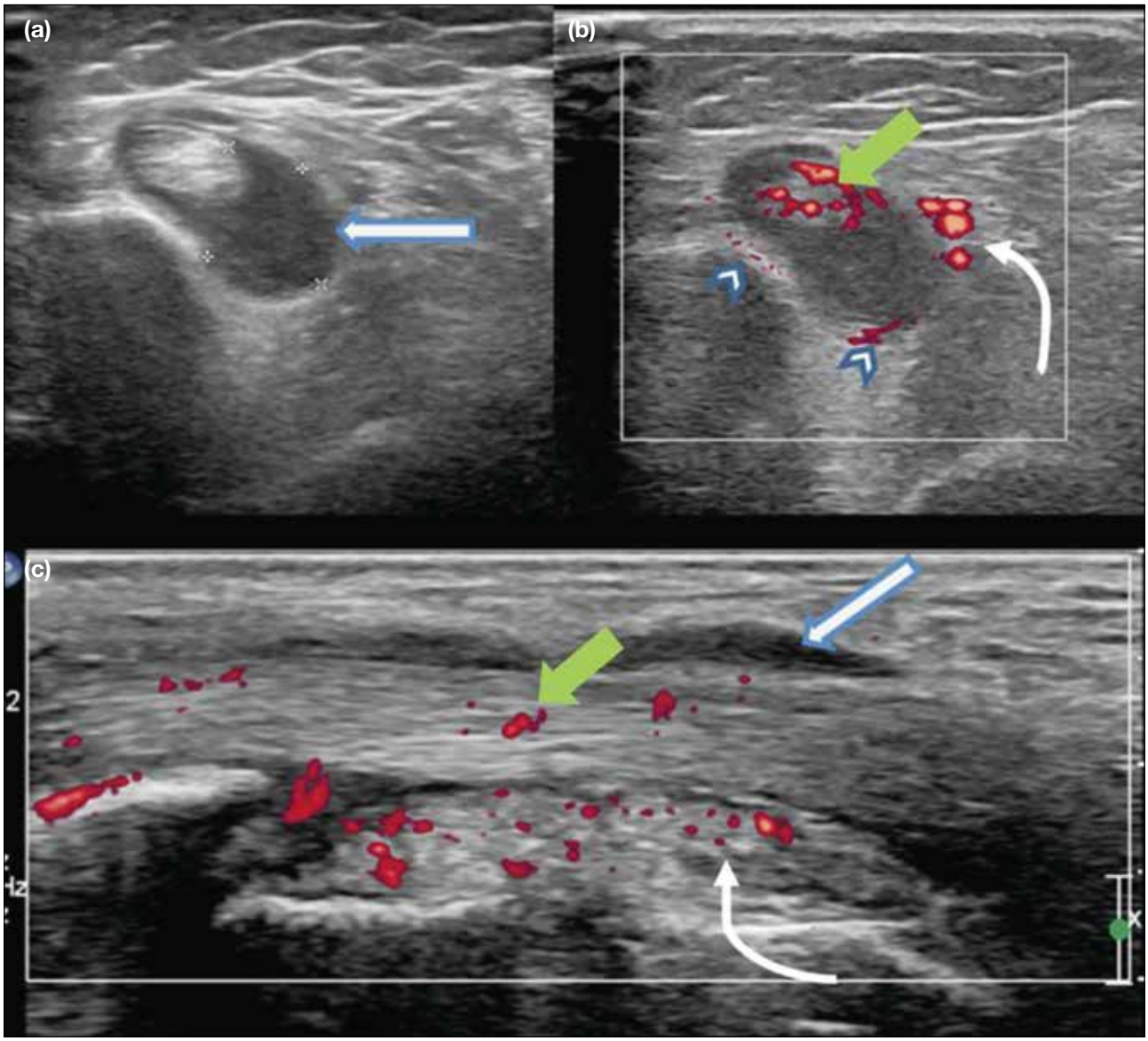

Figure 2. A 10-year-old girl with enthesitis-related arthritis (HLA-B27–positive) presented with right medial ankle pain. (a, b) Short-axis ultrasound (US) images of the posterior tibial tendon (PTT) showing effusion (blue and white arrow) around the tendon, which is thickened with a moderate increase in vascularity within the tendon (green arrow), in the tendon sheath (arrowheads), and adjacent soft tissue (curved arrow). (c) Long-axis US image of the PTT showing similar findings, with effusion (blue and white arrow) and increased vascularity in the tendon (green arrow) and the adjacent soft tissue (curved arrow). Findings are suggestive of tenosynovitis and tendinosis.

valgus due to PTTD also increases the stress on the interosseous talocalcaneal ligaments and cervical ligaments within the sinus tarsi, causing insufficiency of these ligaments over time.[3,18] On MRI, the normal fat signal around the ligament in the sinus tarsi is replaced by abnormal tissue that shows T1 hypointensity and T2 hyperintensity (Figure 8). When fibrotic change within the abnormal tissue predominates, the signal may show T1 and T2 hypointensity.[3,18] Other imaging features include partial or complete tears of the tarsal sinus ligaments.[3]

Plantar Fasciitis

Plantar fasciitis has been found to have a low association with advanced PTT injury, due to increased strain on the plantar fascia which is responsible for supporting the longitudinal arch.[3,18] MRI shows thickening (> 4 mm), irregularity or increased heterogenous signal within the fascia, associated with perifascial and bone marrow oedema.[3]

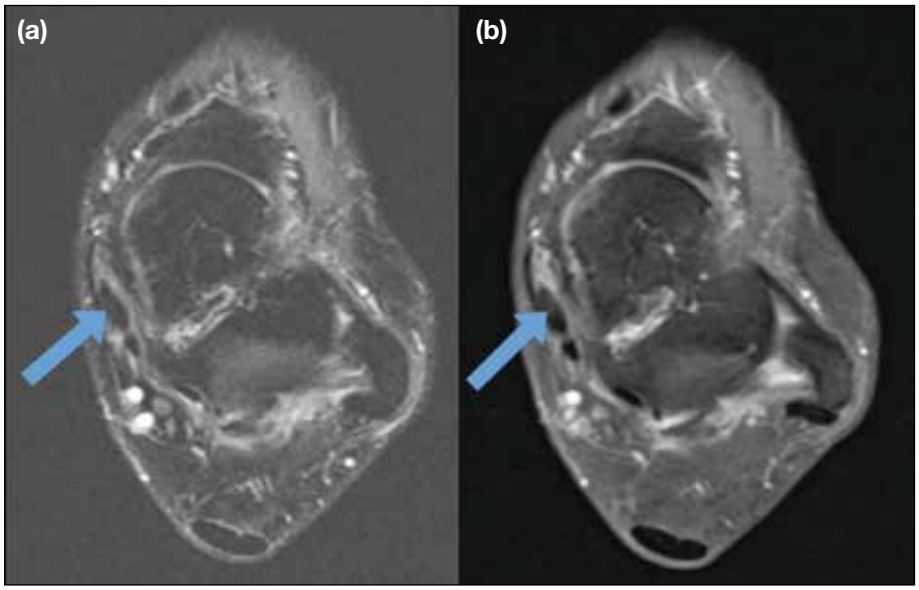

Figure 3. A 63-year-old woman presented with left foot and ankle pain with flexible flatfoot deformity. (a) Axial fat-saturated (FS) proton density–weighted and (b) axial post-contrast FS T1-weighted magnetic resonance images showing posterior tibial tendinosis as evidenced by mildly increased intratendinous signal (arrows).

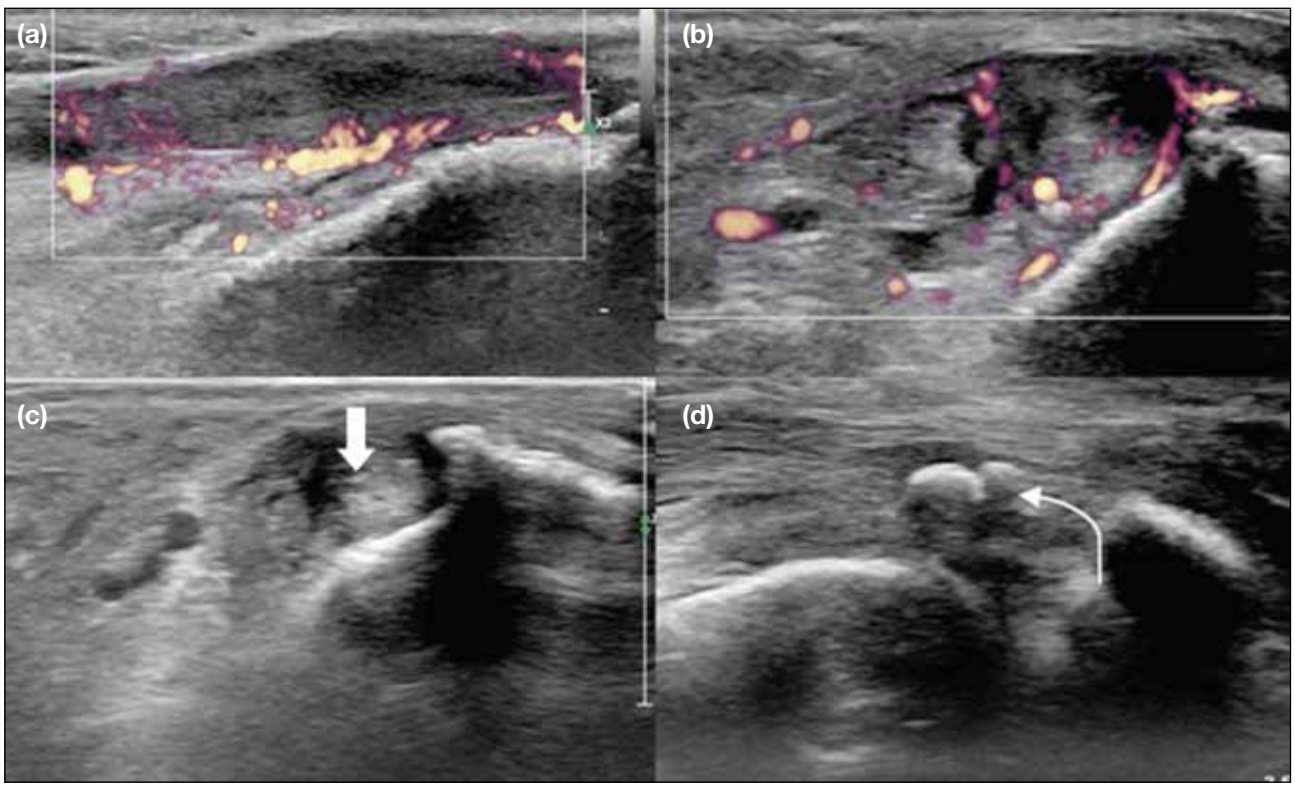

Figure 4. Ultrasound images of a 61-year-old woman presenting with bilateral progressive flexible flatfeet, more severe on the left. (a) Long-axis and (b) short-axis images of the left posterior tibial tendon (PTT) demonstrate enlargement and increased heterogeneity and vascularity of the tendon, suggestive of tendinosis. (c) Short-axis image of the left PTT at the supramalleolar level showing a partial tear (arrow). (d) Calcification/ossification (curved arrow) seen in the long-axis image of the PTT insertion.

Deltoid Ligament Complex Injury

The deltoid ligament complex consists of deep and superficial layers. The deep layer opposes ankle valgus and stabilises the tibiotalar articulation, while the superficial ligaments limit hindfoot eversion and inward displacement of the talar head to stabilise the

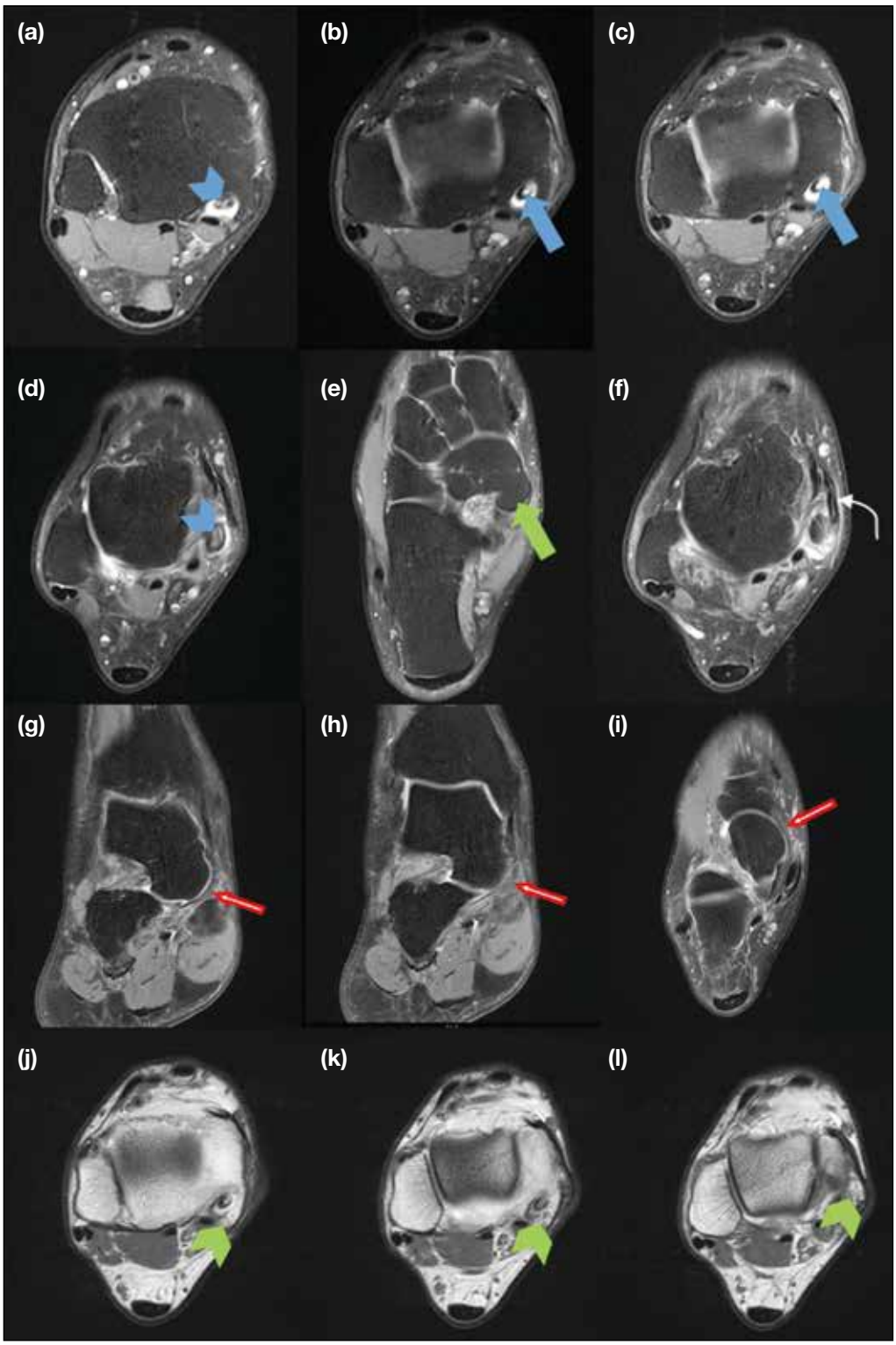

Figure 5. A 61-year-old man complained of right heel pain for approximately a year. Magnetic resonance imaging of his right ankle is suggestive of posterior tibial tendon dysfunction. (a-d) Axial fat-saturated (FS) proton density (PD)–weighted magnetic resonance imaging (MRI) of the posterior tibial tendon from proximal to distal show increased signal and abnormal thickening of the tendon at the level of distal tibia and talus (blue arrowheads in [a] and [d]), suggestive of tendinosis. Fluid signal within the tendon suggests partial tear (blue arrows in [b] and [c]). Small amount of fluid within the tendon sheath are in keeping with tenosynovitis. (e) A cornuate (type III) os naviculare is present (green arrow). (f) Axial FS PD-weighted MRI of the overlying flexor retinaculum showing thickening with increased signal (curved arrow) could be chronic injury or a partial tear. (g-i) Increased signal in and thickening of the spring ligament on the coronal and axial FS PD-weighted MRI (red arrows) is probably related to abnormal stress. (j-l) Axial PD-weighted MRI of the right tibia from proximal to distal shows a prominent spur at the posteromedial aspect of the distal tibia (green arrowheads).

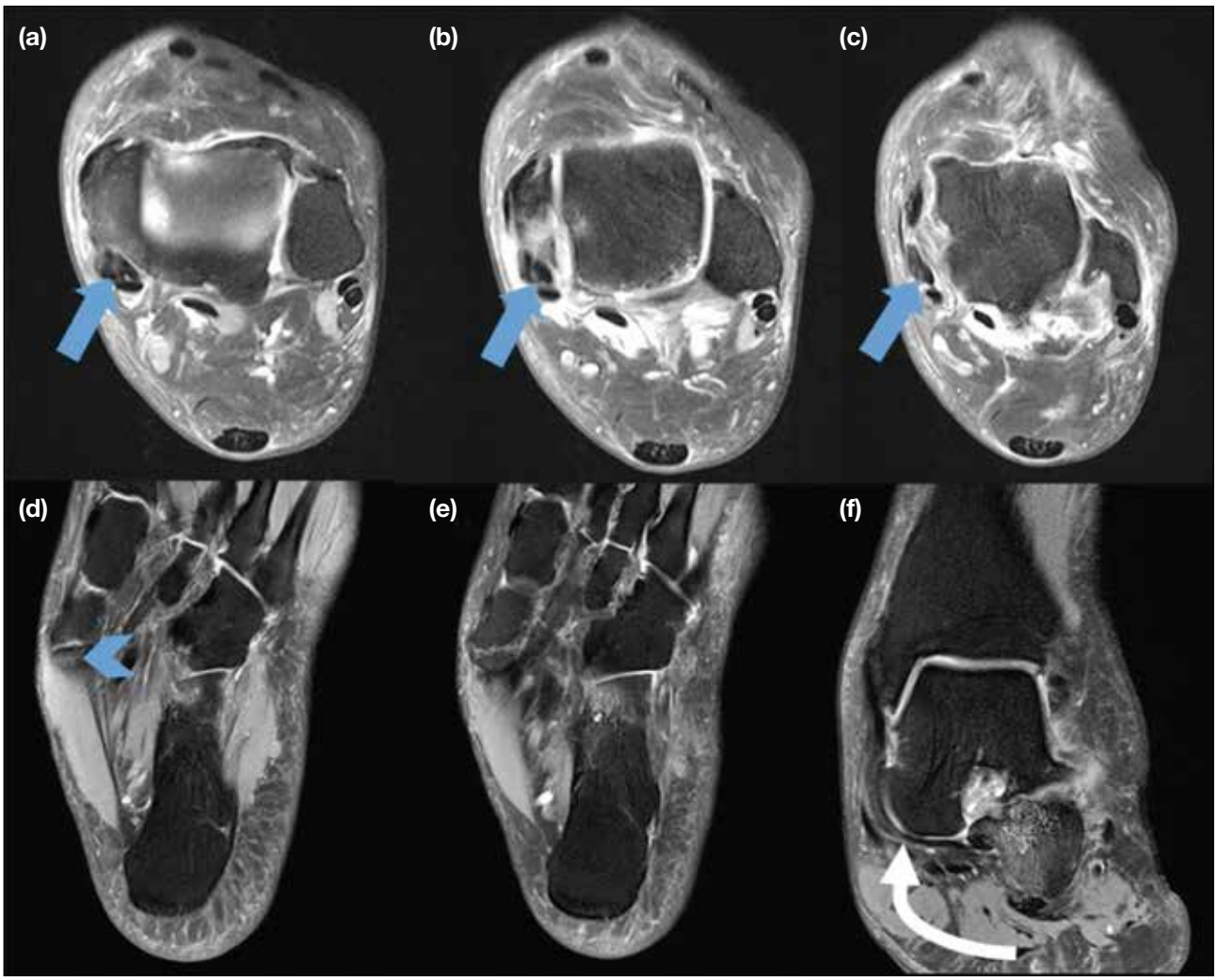

Figure 6. A 57-year-old woman presented with persistent left ankle swelling and pain over the medial aspect of the foot. Magnetic resonance imaging (MRI) of the left ankle revealed a split tear of the posterior tibial tendon (PTT). (a-c) Axial fat-saturated (FS) proton density (PD)–weighted MRI from proximal to distal reveal a grossly thickened PTT with a full thickness split tear, leading to the four-tendon sign (arrows). (d, e) A type II os naviculare with slight increase in marrow fluid signal (arrowhead in [d]) on the FS PD-weighted sequence could represent os naviculare syndrome. (f) Coronal FS PD-weighted MRI showing thinning of the superomedial calcaneonavicular ligament (curved arrow), a component of the spring ligament complex, suggestive of partial tear.

talonavicular joint.[3] Insufficiency of the deltoid ligament complex is seen in late stage of PTTD.[18] On MRI, low-grade sprain causes amorphous signal with loss of the normal striated appearance (Figure 7c and 7d), while high-grade injuries manifest as fluid-filled gaps or even discontinuity of the ligament.[3]

Bony Malalignment

Dysfunction of the PTT causes tension and eventual failure of the secondary supporting structures including the spring ligament, tarsal sinus ligaments, and deltoid ligaments. The biomechanics of the foot are altered, causing a cascade of foot deformities.

Pes Planus

Collapse of the medial longitudinal arch results in pes planus, which can be demonstrated by a reduction in the calcaneal inclination angle on lateral weight-bearing radiographs.[19] The calcaneal inclination angle is drawn between the plane of support and the calcaneal inclination axis (i.e., the line connecting the most inferior point of the calcaneal tuberosity with the most distal and inferior point of the calcaneus along the calcaneocuboid joint) [Figure 9].[19,20] The normal range is 20° to 30°.[19,20]

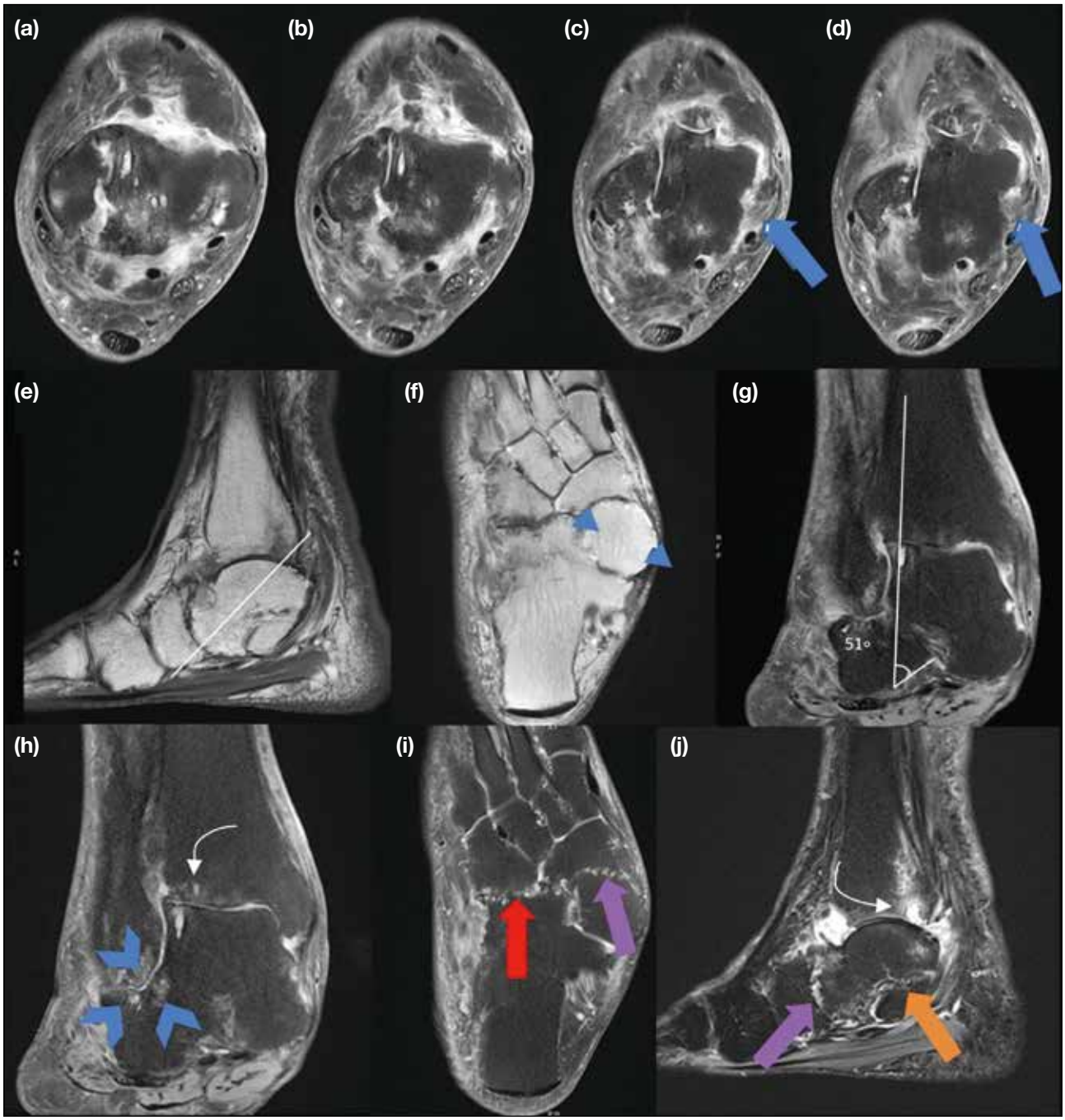

Figure 7. A 67-year-old woman with a history of rheumatoid arthritis reported longstanding bilateral ankle pain and stiffness, more severe in the medial aspect of the right ankle. She had bilateral fixed pes planus, as well as ankle, subtalar, and forefoot deformity. Magnetic resonance imaging (MRI) of her right ankle was performed. (a, b) Axial fat-saturated (FS) proton density (PD)–weighted MRI of the right ankle from proximal to distal show absence of the right posterior tibial tendon, suggestive of complete tear. (c, d) Increased signal in the deltoid ligament in the FS PD-weighted sequence (arrows) suggests partial tear. Sagittal T1-weighted MRI reveals plantar flexion of the talus and inferomedial migration of the talar head. The long axis of the talus, which is indicated by the white line in (e), is inferiorly tilted, instead of bisecting the navicular as in a normal foot. (f) On axial PD-weighted MRI, the navicular covers only about half of the talar head articular surface (the medial and lateral edges of which are marked by the blue triangles). (g) Coronal FS PD-weighted MRI demonstrates hindfoot valgus with an increased tibiocalcaneal angle (51°). (h) Coronal FS PD-weighted image of the right hindfoot shows talocalcaneal and subfibular impingement, bone marrow oedema, and subchondral cysts (arrowheads), signifying secondary osteoarthritis. There was also osteoarthritis of the tibiotalar joint (curved arrow). (i) Axial FS PD-weighted image illustrating osteoarthritis of the calcaneocuboid (red arrow) and talonavicular joints (purple arrow). (j) Osteoarthritis of the subtalar joint (orange arrow), tibiotalar joint (curved arrow), and talonavicular joint (purple arrow) are seen on sagittal FS T2-weighted image.

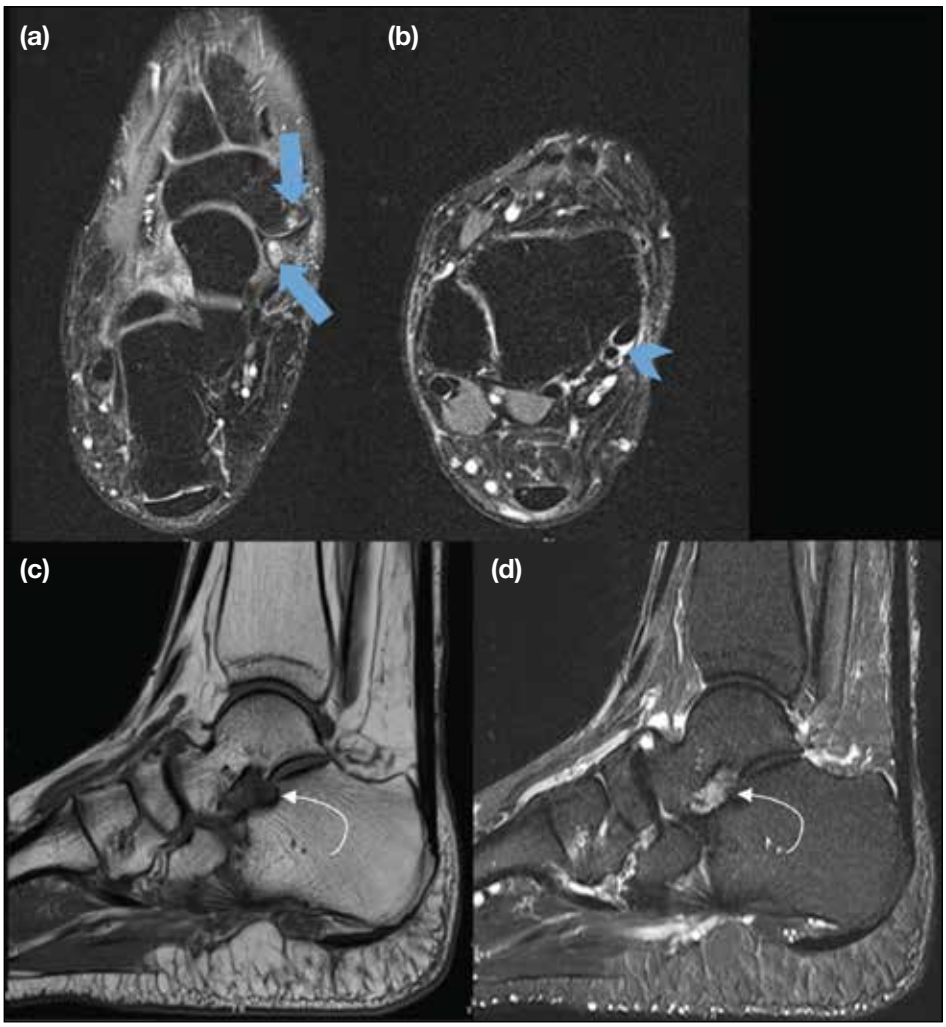

Figure 8. A 38-year-old woman presented with bilateral flatfoot deformity. Magnetic resonance imaging of her right ankle showing tenosynovitis of the posterior tibial tendon (PTT), os navicular syndrome, and sinus tarsi syndrome. (a) A type II os naviculare with bone marrow oedema (arrows) is evident on an axial fat-saturated (FS) proton density–weighted sequence. (b) Mildly increased tendon sheath fluid is seen along the PTT (arrowhead), suspicious for tenosynovitis. (c) Sagittal T1-weighted and (d) sagittal FS T2-weighted images showing abnormal T1 hypointense, T2 hyperintense soft tissue signal in the sinus tarsi (curved arrows), respectively, suggestive of sinus tarsi syndrome.

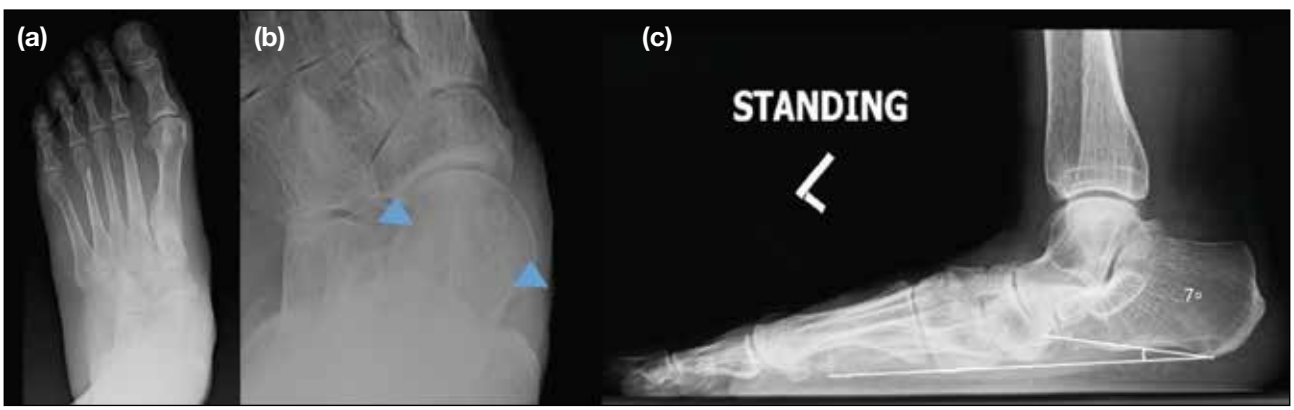

Figure 9. Radiographs of the left foot of the same patient with flatfoot deformity in Figure 4. (a) Standing dorsoplantar (DP) radiograph of the left foot and (b) cropped DP view focusing on the talonavicular joint demonstrate reduced talonavicular coverage. The navicular covers only about half of the talar head articular surface (the medial and lateral edges of which are marked by the blue triangles in [b]). (c) Lateral weight-bearing radiograph of the left foot showing marked reduction of the calcaneal inclination angle (7°), suggestive of pes planus.

Talonavicular Fault

As pes planus progresses, there is excessive plantar flexion of the talus, resulting in talonavicular fault which can be demonstrated on weight-bearing lateral radiographs of the foot or sagittal MRI.[6,19] On sagittal images including the base of the first metatarsal, a long axis drawn along the talus should normally divide the navicular into equal superior and inferior halves. If the line is inferiorly positioned, it suggests talonavicular fault (Figure 7e).[6]

Talar Head Uncoverage

The unopposed pull of the peroneus brevis abducts the forefoot and causes lateral subluxation of the talonavicular joint and uncoverage of the talus.[6,16,19] In a normal foot, most (75%-100%) of the talar head is covered by the navicular; in flatfoot deformity, the talar head becomes more uncovered (Figures 7f and 9b).[21]

Hindfoot Valgus

The degree of hindfoot valgus can be measured on radiographs or on the most posterior coronal image that includes the tibia and calcaneus on MRI, by measuring the angle between the long axis of the tibia and a line along the medial calcaneal wall (Figure 7g), with the normal range measuring 0° to 6°.[22]

Lateral Hindfoot Impingement

As hindfoot valgus progresses, lateral hindfoot impingement, including talocalcaneal impingement and/or subfibular impingement, may occur (Figure 7h).[18] On MRI, talocalcaneal impingement causes bone marrow oedema, cysts, and sclerosis at the site where the lateral talar process impinges on the lateral cortex of the calcaneus.[18] Common findings in subfibular impingement include low signal on T1-weighted imaging and predominantly low signal on T2-weighted imaging from soft tissue entrapment between the distal fibula and calcaneus, direct osseous contact between calcaneus and fibula, and distal fibular oedema.[18,22]

Secondary Osteoarthritis

In late-stage disease, chronic uneven stress and bony malalignment result in secondary osteoarthritis of the subtalar, talonavicular, calcaneocuboid, and tibiotalar joints.[10]

MANAGEMENT

Conservative treatment is the first-line treatment for PTTD and is indicated before operative treatment is considered. It involves treatment of the acute inflammation in the early stages, physiotherapy and accommodation of the deformity in late stages, including appropriate footwear (e.g., flat lace-up shoes) and orthosis.[7,23,24]

Operative treatment is indicated if conservative treatment fails, typically in Stages II to IV diseases and less frequently in Stage I disease, with reported good to excellent outcome in > 80% of the patients at 5 years' follow-up. A wide variety of surgical options have been reported; in general, they consist of different combinations of soft tissue procedures addressing the PTTD and osseous procedures addressing the malalignment. A few commonly performed procedures are discussed below.

In early PTTD (Stages I and II diseases), surgical release, simple tenosynovectomy and tendon debridement are indicated in cases of mild tendon inflammation, which have been reported to be helpful in pain relief.[25] However, combined procedures including soft tissue reconstructions (e.g., tendon transfer and side-to-side anastomosis) and bony procedures are often performed to address the PTTD and osseous deformities.[23]

In more advanced Stage II disease, tendon transfer is often the choice of treatment (Figures 10 and 11).[3] The FDL tendon is the most commonly transferred tendon, which is transferred to replicate the function of the PTT by augmenting hindfoot inversion strength and reducing adduction across the tarsal joint.[23] A calcaneal osteotomy is often performed at the same time to correct hindfoot valgus and medialise the pulling force of the Achilles tendon.[3,23,25]

Patients with an accessory navicular bone causing PTTD can benefit from the Kidner procedure, in which the accessory navicular bone is excised and the PTT is rerouted to a more plantar position at the undersurface of the remaining navicular (Figure 12).[26] Modifications of the Kidner procedure have been reported, which involve advancement of the PTT insertion using suture anchors, biotenodesis screws, or osseous tunnels to reattach the PTT.[23] The Kidner procedure and its modifications remain the current standard of care, with reported success rates of up to 96%.[27,28]

In the late stages of PTTD (Stages III and IV), surgical management often involves different forms of arthrodesis, with or without concomitant soft tissue reconstruction and osteotomy procedures.[3,23,24]

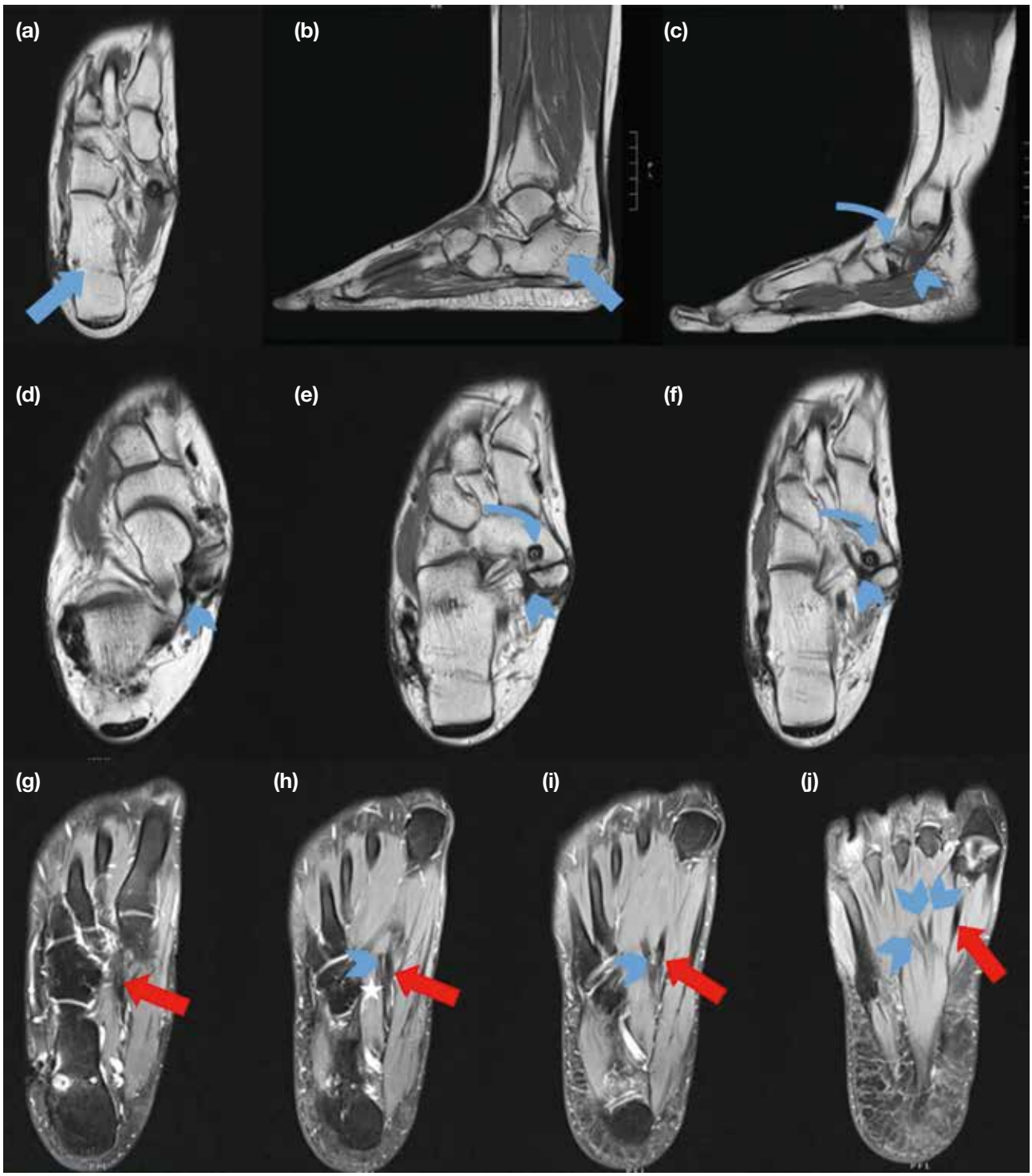

Figure 10. Postoperative magnetic resonance imaging (MRI) of the right ankle of a 26-year-old woman who underwent flexor digitorum longus (FDL) tendon transfer and medialising calcaneal osteotomy for posterior tibial tendon dysfunction after failing conservative treatment. (a, b) Axial and sagittal proton density (PD)–weighted MRI of the right ankle showing evidence of medialising calcaneal osteotomy with satisfactory bony union (arrows). (c) Sagittal and (d-f) axial PD-weighted MRI of the right ankle from proximal to distal showing the distal FDL tendon (arrowheads) transferred into a bony tunnel in the navicular and fixed with a screw (curved arrows in [c], [e], and [f]). (g-j) Axial fat-saturated PD-weighted MRI of the right ankle from proximal to distal demonstrating the FDL tendon (arrowheads in [h] to [j]) attachment to flexor hallucis longus tendon (red arrows) at the level of the Knot of Henry (star in [h]).

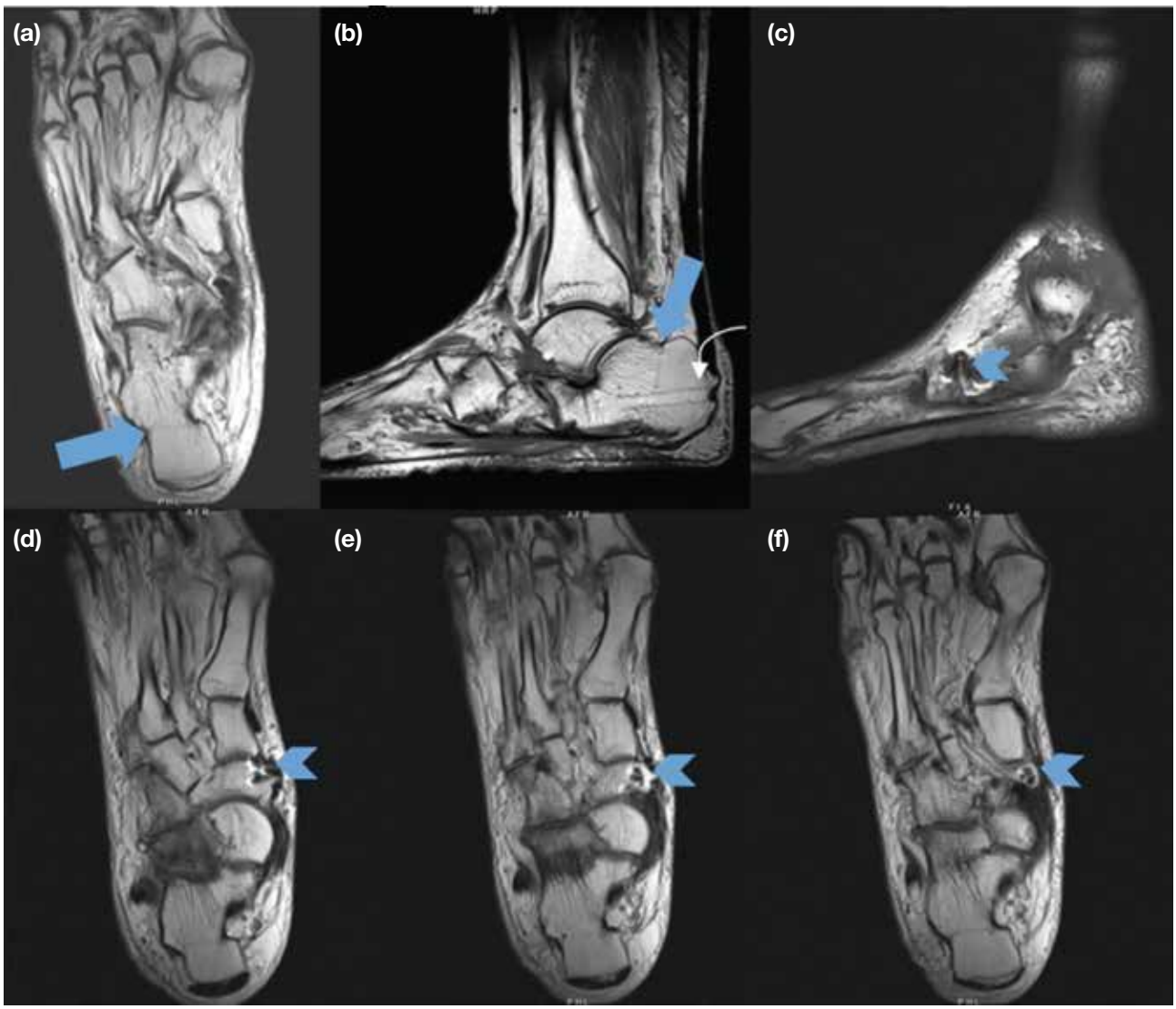

Figure 11. Postoperative magnetic resonance imaging (MRI) of the right ankle of a 67-year-old man who had flexor hallucis longus (FHL) tendon transfer and medialising calcaneal osteotomy for rupture of posterior tibial tendon 8 years ago. (a) Axial proton density (PD)–weighted and (b) sagittal T1-weighted MRI of the right ankle showing satisfactory bony reunion from medialising calcaneal osteotomy (arrows). There is evidence of prior screw insertion from proximal to distal calcaneum for fixation (curved arrow in [b]), which had already been removed. (c) Sagittal T1-weighted MRI and (d-f) axial PD-weighted MRI from proximal to distal showing surgical materials at the tunnel created at the navicular bone (arrowheads), where the transferred FHL tendon is attached.

CONCLUSION

Imaging findings of PTTD include a spectrum of changes ranging from tenosynovitis, tendinosis, and partial to complete tear. A myriad of related secondary findings may be seen as PTTD increases strain on other supporting structures, causing progressive malalignment and deformity of the foot. Familiarisation with the imaging features of PTTD allows early diagnosis, guides appropriate treatment, and aids surgical planning in advanced cases.

REFERENCES

1. Major NM, Anderson MW. Musculoskeletal MRI E-Book. Elsevier Health Sciences; 2019.
2. Den Hartog BD. Flexor digitorum longus transfer with medial displacement calcaneal osteotomy. Biomechanical rationale. Foot Ankle Clin. 2001;6:67-76.
3. Flores DV, Mejía Gómez C, Fernández Hernando M, Davis MA, Pathria MN. Adult acquired flatfoot deformity: anatomy, biomechanics, staging, and imaging findings. Radiographics. 2019;39:1437-60.
4. Funk DA, Cass J, Johnson K. Acquired adult flat foot secondary to posterior tibial tendon pathology. J Bone Joint Surg Am.

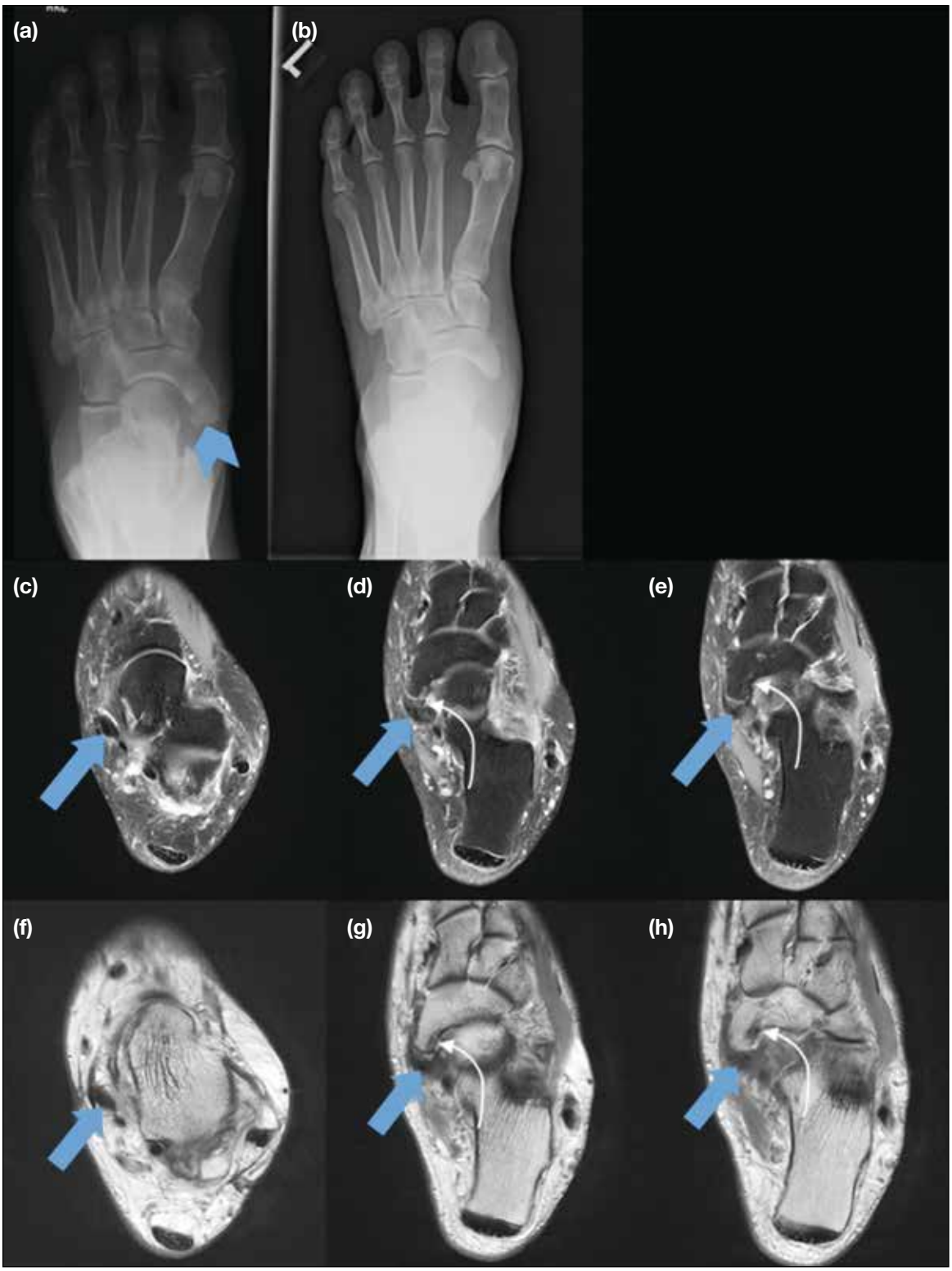

Figure 12. Radiographs and magnetic resonance imaging (MRI) of a 50-year-old woman with a history of left posterior tibialis tendonitis and accessory navicular, who underwent a Kidner procedure and later re-excision of bony overgrowth of the navicular. (a) Preoperative dorsoplantar (DP) radiograph of the left foot showing a prominent navicular bone with type II accessory navicular (arrowhead). (b) Postoperative DP radiograph of the left foot demonstrates that the accessory navicular and part of the parent navicular have been excised. (c-e) Postoperative axial fat-saturated proton density (PD)–weighted MRI of the left ankle from proximal to distal show the distal tibialis posterior tendon (arrows) reattached to the navicular body by a suture anchor (curved arrows in [d] and [e]). (f-h) Axial PD-weighted MRI corresponding to Figure 12c to 12e reveals similar postoperative findings. The distal tibialis posterior tendon (arrows) was reattached to the navicular body by a suture anchor (curved arrows in [g] and [h]), which is better appreciated in this sequence.

1986;68:95-102.
5. Khoury NJ, el-Khoury GY, Saltzman C, Brandser E. MR imaging of posterior tibial tendon dysfunction. AJR Am J Roentgenol. 1996;167:675-82.
6. Schweitzer ME, Karasick D. MR imaging of disorders of the posterior tibialis tendon. AJR Am J Roentgenol. 2000;175:627-35.
7. Giza E, Cush G, Schon LC. The flexible flatfoot in the adult. Foot Ankle Clin. 2007;12:251-71.
8. Jesse MK, Hunt KJ, Strickland C. Postoperative imaging of the ankle. AJR Am J Roentgenol. 2018;211:496-505.
9. Mann RA, Thompson F. Rupture of the posterior tibial tendon causing flat foot. Surgical treatment. J Bone Joint Surg Am. 1985;67:556-61.
10. Johnson KA, Strom DE. Tibialis posterior tendon dysfunction. Clin Orthop Relat Res. 1989;(239):196-206.
11. Chhabra A, Soldatos T, Chalian M, Faridian-Aragh N, Fritz J, Fayad LM, et al. 3-Tesla magnetic resonance imaging evaluation of posterior tibial tendon dysfunction with relevance to clinical staging. J Foot Ankle Surg. 2011;50:320-8.
12. Mankey MG. A classification of severity with an analysis of causative problems related to the type of treatment. Foot Ankle Clin. 2003;8:461-71.
13. Petersen B, Fitzgerald J, Schreibman K. Musculotendinous magnetic resonance imaging of the ankle. Semin Roentgenol. 2010;45:250-76.
14. Premkumar A, Perry MB, Dwyer AJ, Gerber LH, Johnson D, Venzon D, et al. Sonography and MR imaging of posterior tibial tendinopathy. AJR Am J Roentgenol. 2002;178:223-32.
15. Rosenberg ZS, Cheung Y, Jahss MH, Noto AM, Norman A, Leeds NE. Rupture of posterior tibial tendon: CT and MR imaging with surgical correlation. Radiology. 1988;169:229-35.
16. Schweitzer ME, Caccese R, Karasick D, Wapner KL, Mitchell DG. Posterior tibial tendon tears: utility of secondary signs for MR imaging diagnosis. Radiology. 1993;188:655-9.
17. Gazdag AR, Cracchiolo A 3rd. Rupture of the posterior tibial tendon. Evaluation of injury of the spring ligament and clinical assessment of tendon transfer and ligament repair. J Bone Joint Surg Am. 1997;79:675-81.
18. Mengiardi B, Pinto C, Zanetti M. Spring ligament complex and posterior tibial tendon: MR anatomy and findings in acquired adult flatfoot deformity. Semin Musculoskelet Radiol. 2016;20:104-15.
19. Soliman SB, Spicer PJ, van Holsbeeck MT. Sonographic and radiographic findings of posterior tibial tendon dysfunction: a practical step forward. Skeletal Radiol. 2019;48:11-27.
20. Gentili A, Masih S, Yao L, Seeger LL. Pictorial review: foot axes and angles. Br J Radiol. 1996;69:968-74.
21. Meyr AJ, Sansosti LE, Ali S. A pictorial review of reconstructive foot and ankle surgery: evaluation and intervention of the flatfoot deformity. J Radiol Case Rep. 2017;11:26-36.
22. Donovan A, Rosenberg ZS. Extraarticular lateral hindfoot impingement with posterior tibial tendon tear: MRI correlation. AJR Am J Roentgenol. 2009;193:672-8.
23. Dimmick S, Chhabra A, Grujic L, Linklater JM. Acquired flat foot deformity: postoperative imaging. Semin Musculoskelet Radiol. 2012;16:217-32.
24. Pomeroy GC, Pike RH, Beals TC, Manoli A 2nd. Acquired flatfoot in adults due to dysfunction of the posterior tibial tendon. J Bone Joint Surg Am. 1999;81:1173-82.
25. Zaw H, Calder JD. Operative management options for symptomatic flexible adult acquired flatfoot deformity: a review. Knee Surg Sports Traumatol Arthrosc. 2010;18:135-42.
26. Kidner FC. The prehallux in relation to flatfoot. JAMA. 1933;101:1539-42.
27. Kopp FJ, Marcus RE. Clinical outcome of surgical treatment of the symptomatic accessory navicular. Foot Ankle Int. 2004;25:27-30.
28. Prichasuk S, Sinphurmsukskul O. Kidner procedure for symptomatic accessory navicular and its relation to pes planus. Foot Ankle Int. 1995;16:500-3.

Hong Kong J Radiol. 2024;27(1):e65-74. Published 12 March 2024 | https://doi.org/10.12809/hkjr2217645

PICTORIAL ESSAY

Endovascular Management of Iatrogenic Neck Vascular Injury After Central Venous Catheterisation

SC Wong, SY Lam, SKH Wong, HF Chan, LF Cheng

Department of Radiology, Princess Margaret Hospital, Hong Kong SAR, China

INTRODUCTION

Central venous line placement is a common procedure in both elective and emergency settings across different medical and surgical specialties. The jugular and subclavian approaches are common methods of central venous catheterisation in the neck, which can be performed by traditional methods based on anatomical landmarks or under ultrasound guidance.[1]

Though rare, iatrogenic neck arterial injury can occur during attempts at central venous catheterisation, leading to serious complications such as arterial perforation with active bleeding, pseudoaneurysm, arteriovenous fistula, arterial dissection, or vascular occlusion resulting in neurological or ischaemic sequelae. Risk factors include obesity, short neck, and emergency catheterisation.[2,3] Surgical approaches to repair injured arteries may involve extensive dissection or open-cardiothoracic surgical repair and vascular grafting, and often require general anaesthesia. These may entail prolonged recovery and may not be tolerated by critically ill or elderly patients.

Endovascular management of central venous line complications and retrieval of retained indwelling catheters or their components can be a promising first-line treatment option in view of its minimally invasive nature, high success rate with reduced morbidity, and enhanced recovery compared with open surgery. It may be performed under local anaesthesia.

Treatment plans for arterial complications should be individualised based on the type of complication, relationship to adjacent vital vessels, angiographic factors, and patients' underlying health conditions. The pros and cons of different endovascular treatment options need to be examined.

With increasing use of long-term indwelling venous

Correspondence: *Dr SC Wong, Department of Radiology, Princess Margaret Hospital, Hong Kong SAR, China*
Email: wsc696@ha.org.hk

Submitted: 7 October 2022; Accepted: 4 January 2023.

Contributors: All authors designed the study, acquired the data, analysed the data, drafted the manuscript, and critically revised the manuscript for important intellectual content. All authors had full access to the data, contributed to the study, approved the final version for publication, and take responsibility for its accuracy and integrity.

Conflicts of Interest: All authors have disclosed no conflicts of interest.

Funding/Support: This study received no specific grant from any funding agency in the public, commercial, or not-for-profit sectors.

Data Availability: All data generated or analysed during the present study are available from the corresponding author on reasonable request.

Ethics Approval: This study was approved by the Kowloon West Cluster Research Ethics Committee of Hospital Authority, Hong Kong [Ref No.: KW/EX-22-026(170-02)]. The patients were treated in accordance with the tenets of the Declaration of Helsinki. Informed consent from patient was waived by the Committee due to anonymisation and secure storage of all patient data.

Acknowledgement: The authors thank Dr WK Ng, Dr TW Yan and Dr KM Chan, vascular surgeons from the Department of Surgery of Princess Margaret Hospital, for their contribution to the endovascular treatment and surgical dissection in the cases illustrated in the study.

catheters, it is vital that clinicians be aware of the associated risks of retained catheter component(s) within veins or failed catheter removal due to an adherent fibrin sheath. Forceful removal may further jeopardise blood vessels or result in device fragmentation or embolisation.

This article reviews cases of successful treatment of the iatrogenic complications of neck arterial catheterisation during central venous catheterisation as well as of unintentionally retained catheters or their fragments from neck veins, with illustration of different endovascular treatment techniques.

ARTERIAL INJURY

The subclavian, brachiocephalic, and carotid arteries are in close proximity to the internal jugular and subclavian veins, placing them at risk of iatrogenic injury during venous catheterisation. Reflux of pulsatile or fresh blood within the catheter, neck haematoma, abnormal catheter course, or acute neurological deficit should raise suspicion for arterial injury. The risk of complications increases with the calibre of the device that punctured the artery.[4,5]

In the setting of iatrogenic carotid artery puncture by small-calibre vascular access needles (e.g., ≤ 20-G), the risk of major complications is relatively low, with needle removal and external compression being a feasible management option with a low complication rate.[5] However, in the case of subclavian or brachiocephalic artery injury, haemostasis by compression alone may be ineffective due to lack of an underlying bone to facilitate compression in the supraclavicular region, and is associated with a higher complication rate.[3]

Ideally, operators should confirm the venous location of the vascular access needle prior to insertion of large-bore vascular dilator, sheath or catheter, because of the higher complication rates if these instruments are unintentionally introduced into the arterial system.[4] If iatrogenic large-bore catheter injury occurs (such as insertion of a catheter > 7 Fr or a vessel dilator[4,5]), operators should refrain from immediate withdrawal of the malpositioned catheter from major arteries, as the catheter can still tamponade the vessel, limiting bleeding and providing an endovascular access route for closure of the arterial perforation. Intravascular balloon tamponade against the arterial puncture site for temporary haemostasis can also be helpful while contemplating definitive treatment. A misplaced dilator or large-bore catheter should be left in place as recommended by the Practice Guidelines for Central Venous Access 2020 by the American Society of Anesthesiologists[4] prior to removal. Urgent resuscitation, multidisciplinary consultation with interventional radiologists, vascular or cardiothoracic surgeons should be sought to devise an individualised treatment plan. If the site of arterial injury is clearly visible and surgically accessible, treatment options may include direct surgical arterial repair[5] or endovascular treatment. However, when the site of arterial injury is not well defined or easily accessible surgically, prompt imaging evaluation[5] such as computed tomographic angiography is pivotal in treatment planning and assessing complications.

Different endovascular treatment options can be used sequentially or in combination to achieve haemostasis, which comprise endovascular treatment such as stenting, embolisation, or coiling of a pseudoaneurysm using a percutaneous approach. Embolisation or coiling of a pseudoaneurysm may be performed if the pseudoaneurysm sac can be selectively cannulated, which may be technically challenging in the neck region especially if the injured feeding vessel is tortuous.

Endovascular Stenting

Covered stent graft deployment along the injured segment is helpful in preserving perfusion, with exclusion of the pseudoaneurysm from circulation (Figure 1). This is imperative if the injured artery must be preserved to supply organs or extremities.

In the literature, both balloons and self-expanding stents have been used in management of arterial injury.[6] Among self-expanding stents, Fluency (Bard Peripheral Vascular Inc, Tempe [AZ], US), Viabahn (WL Gore & Associates Inc, Newark [DE], US), Wallgraft (Boston Scientific, Natick [MA], US), and Cragg covered stents (Boston Scientific, Natick [MA], US) have all been used.[6] The covered stents available in the Hong Kong market include the Fluency self-expanding stent, the BeGraft peripheral balloon-mounted stent graft system (Bentley InnoMed, Hechingen, Germany), the iCover balloon-expandable stent (iVascular, Barcelona, Spain), and the recently available Advanta V12 balloon-expandable covered stent (Advanta, Getinge, Sweden).

Choice of stent graft should be based on device availability, the operator's experience, arterial diameter, distance of other vital branches from the subclavian artery

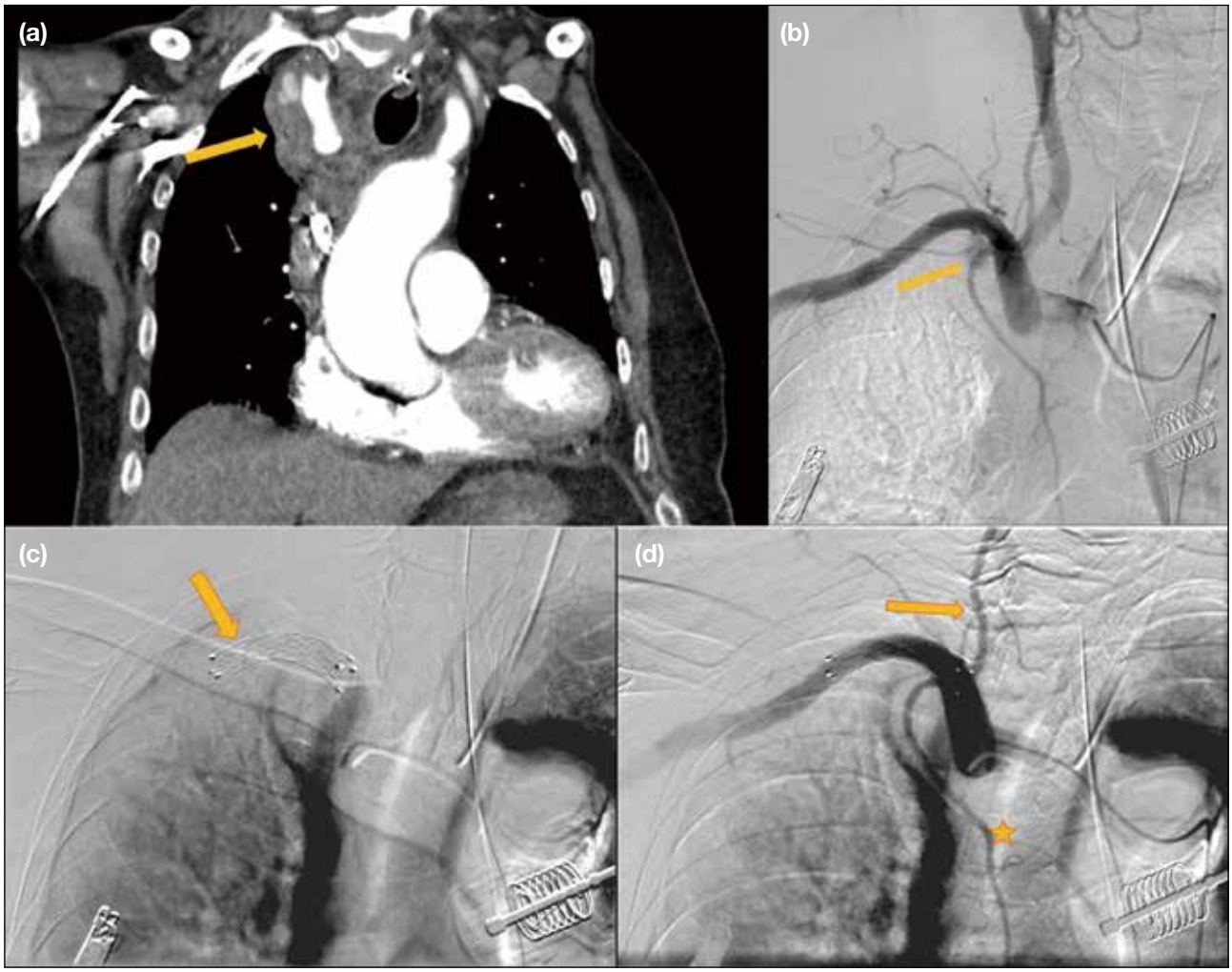

Figure 1. Case 1. Right subclavian artery perforation with pseudoaneurysm formation after attempted central venous catheterisation. (a) Contrast-enhanced computed tomographic angiography of the thorax and (b) digital subtraction angiography demonstrated a pseudoaneurysm (arrows) arising from the proximal right subclavian artery, with adjacent haematoma. (c) Using right femoral access, the right subclavian artery was cannulated with a 4-Fr H1 catheter (Cordis Corporation, Miami [FL], US) and a 0.035 inch × 150 cm Terumo guidewire (Terumo Medical Corporation, Somerset [NJ], US), followed by a guidewire exchange to a 0.035 inch × 260 cm Super Stiff Amplatz guidewire (Boston Scientific, Natick [MA], US). A 10 mm × 40 mm Fluency stent graft (Bard Peripheral Vascular, Tempe [AZ], US) [arrow] was deployed over the wire along the injured segment of the right subclavian artery, distal to the origin of the right vertebral artery. (d) Post-stenting angiography shows successful exclusion of the pseudoaneurysm with preservation of blood flow to the vertebral (arrow) and internal mammary arteries (star).

(especially the vertebral artery), and the availability of adequate landing zones. An ideal covered stent should have flexibility and conformability to the vessel, allowing for adaptation to vascular tortuosity.

Caution should be exercised if stent deployment potentially involves the vertebral artery origin, due to the risk of impairing posterior circulation, resulting in ischaemic stroke, especially if patients lack contralateral dominant vertebral artery supply.

To the best of authors' knowledge and experience, while there is no universal consensus or guideline regarding the use of antiplatelet drugs or anticoagulants after emergency stenting, the clinical decision regarding choice and timing of starting antiplatelet drugs and anticoagulants after stenting should be based on balancing the risks of rebleeding versus stent thrombosis, as well as contraindications for antiplatelet or anticoagulant use from patient co-morbidities (such as recent intracranial haemorrhage).

In the long term, the decision for lifelong antiplatelet treatment (e.g., lifelong aspirin 80 mg per oral daily) would be made on a case-by-case basis, balancing the risk of stent thrombosis versus the risk of long-term antiplatelet use.

Vascular Closure Devices

Suture-mediated vascular closure devices have emerged as an alternative treatment option and are particularly favoured in frail patients in averting major open surgical repair. Originally approved for percutaneous

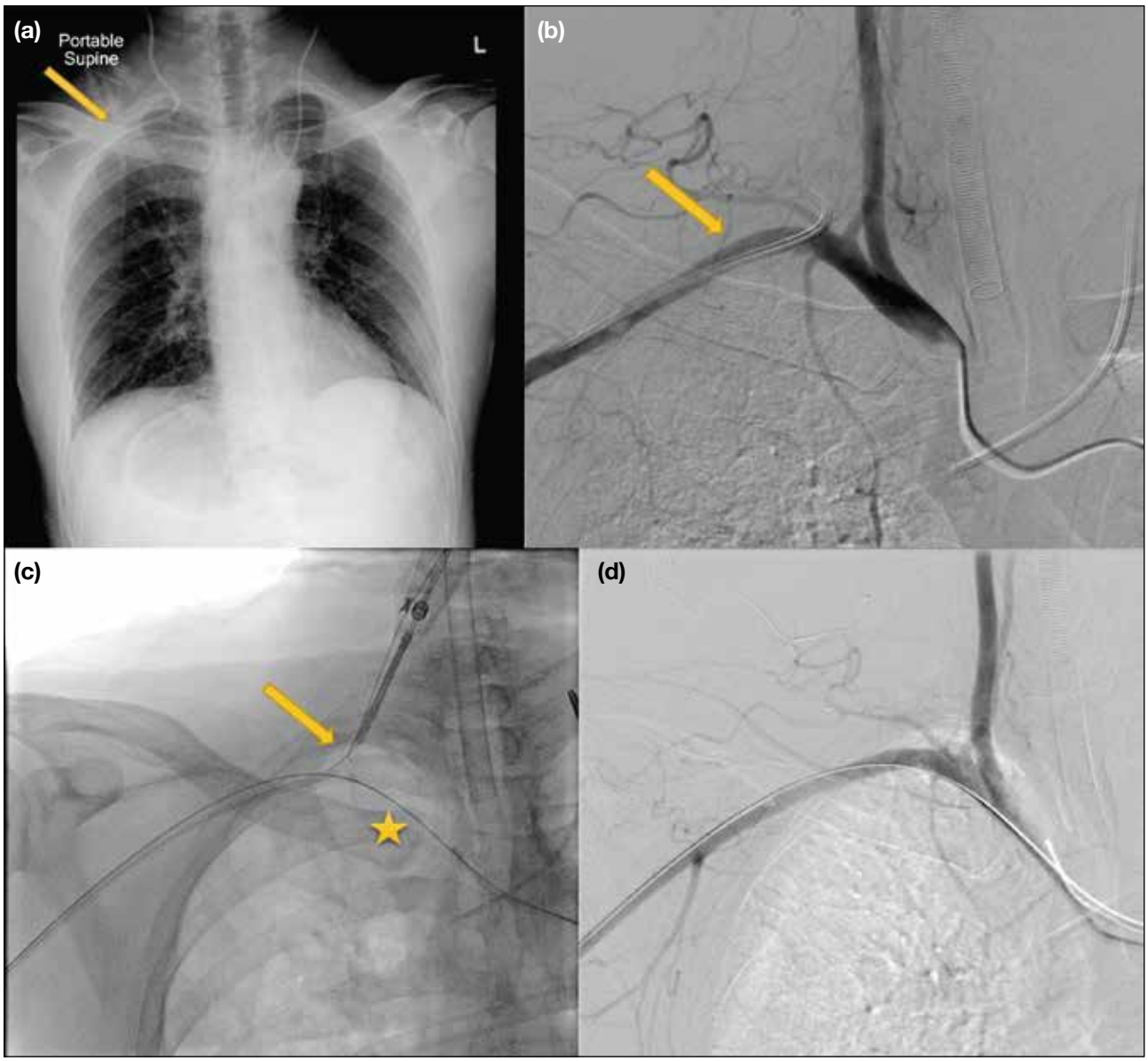

Figure 2. Case 2. A malpositioned triple lumen central venous catheter perforates into the right subclavian artery. Chest X-ray (a) demonstrates the abnormal course of the catheter with subclavian artery catheterisation and the tip (arrow) angulated towards the right axilla. Digital subtraction angiography (b) shows the course of catheter within the right subclavian artery (arrow), with the site of arterial entry distal to the origin of the vertebral artery and the tip in the right axillary artery. The interventional radiology team planned for removal of the catheter with arterial repair by a vascular closure device. (c) A safety guidewire (260-cm Amplatz Super Stiff guidewire; Boston Scientific, Natick [MA], US) was inserted via a right femoral artery sheath, coursing to the right brachial artery (star). Right lower neck dissection was performed by the vascular surgeons to facilitate access to the subclavian artery for deployment of the vascular closure device and repair of the internal jugular vein. The malpositioned catheter in the right subclavian artery was removed over a 0.035-inch Terumo guidewire (Terumo Medical Corporation, Somerset [NJ], US). The right subclavian artery was repaired by Perclose ProGlide (Abbott Vascular, Redwood City [CA], US) [arrow] deployed just adjacent to the subclavian artery at neck dissection. A subsequent right subclavian angiogram (d) reveals a patent subclavian artery without contrast extravasation. The safety guidewire was then removed with neck wound closure by surgery.

closure of femoral artery punctures, which are more superficial, suture-mediated closure devices such as Perclose ProGlide have been used off-label with reports of successful closure of the subclavian or innominate artery.[7,8] The minimal amount of intraluminal material used mitigates the risk of thromboembolism or device dislodgement. To facilitate deployment of the closure device as close to the vessel perforation site as possible in a relatively deep arterial perforation site along the subclavian or innominate artery, regional neck dissection by vascular surgery to gain adequate vessel exposure may be helpful (Figure 2).

Complications of suture-mediated closure devices include complete occlusion of the artery[9] and failed haemostasis. Therefore, placement of a safety guidewire into the injured artery prior to deploying the vascular closure device (Figure 2c) would facilitate rapid deployment of a balloon for temporary occlusion, or stenting as secondary haemostatic measures in case of failure of vascular closure device.

Pseudoaneurysm Treatment with Percutaneous Thrombin Injection

Percutaneous thrombin injection for pseudoaneurysms is a safe and effective treatment with a success rate of > 90%,[10,11] which is useful in the supraclavicular or retroclavicular region and is accessible with percutaneous needle puncture or when the injured artery is not accessible by endovascular catheterisation (Figures 3 and 4). Slow injection under real-time imaging guidance, with the needle tip directed away from the pseudoaneurysm sac, help minimise the risk of non-target embolisation. The advantages of this procedure include simplicity, speed and less discomfort compared with ultrasound-guided compression, as well as a low complication rate (< 1.3%).[11]

A small risk of iatrogenic thrombin embolisation into the parent artery resulting in arterial occlusion[11] exists, which may be minimised with injection distant from the pseudoaneurysm neck. Other risks include allergic rection and infection such as skin cellulitis or abscess formation.

RETRIEVAL OF BROKEN CATHETER FRAGMENTS

Mechanical failure of a long-term central venous catheter may result in catheter fragmentation, dislodgement, or embolisation. Imaging with plain radiographs such as chest X-ray is readily available for prompt screening of catheter integrity in clinical setting.

Computed tomography enables accurate localisation of dislodged catheter fragments, assessment of the relationship to adjacent vasculature, and detection of complications. Imaging can facilitate assessment of crucial factors in treatment planning, including the size, orientation and location of dislodged catheter fragments, the calibre of venous access routes, and the intended extraction route and vascular access site, which can guide the choice of type and size of retrieval device with reference to available institutional resources.

Establishment of venous access through a large calibre superficial vein such as the internal jugular or common femoral vein is beneficial in enabling convenient equipment deployment. Haemostasis in these superficial venous access sites can be more easily achieved with compression.[12] The relatively straightforward course from the right internal jugular vein or femoral veins to the vena cava with reduced angulation compared with the left side facilitates easier engagement and retrieval of retained catheter fragments in the vena cava. Commonly used retrieval tools include Amplatz Goose Neck snare (ev3 Inc, Plymouth [MN], US; Figure 5) or EN Snare (Merit Medical, West Jordan [UT], US; Figure 6).

FIBRIN SHEATH STRIPPING AROUND RETAINED CATHETER THROUGH TRANSFEMORAL VENOUS ACCESS

Fibrin sheath formation is a common complication with long-term indwelling catheter, leading to encasement of catheter tip or side hole impairing catheter patency, thrombus formation or infective complications.[13] Fibrin sheaths may also be adherent to the catheter and vessel wall, precluding catheter removal. While fibrin sheath detection from plain radiography or cross-sectional imaging is difficult given their thin appearance, fluoroscopy with contrast injection into the affected catheter is helpful in depicting fibrin sheath as filling defects, as well as contrast reflux along the proximal catheter with efflux from defects in the sleeve, or excessive ejection of contrast material from the side holes of the proximal port,[13] which may be secondary to blockage of catheter tip outflow by fibrin sheath.

In the event of adherent catheter to vessel wall due to fibrin sheath precluding catheter removal, fibrin sheath

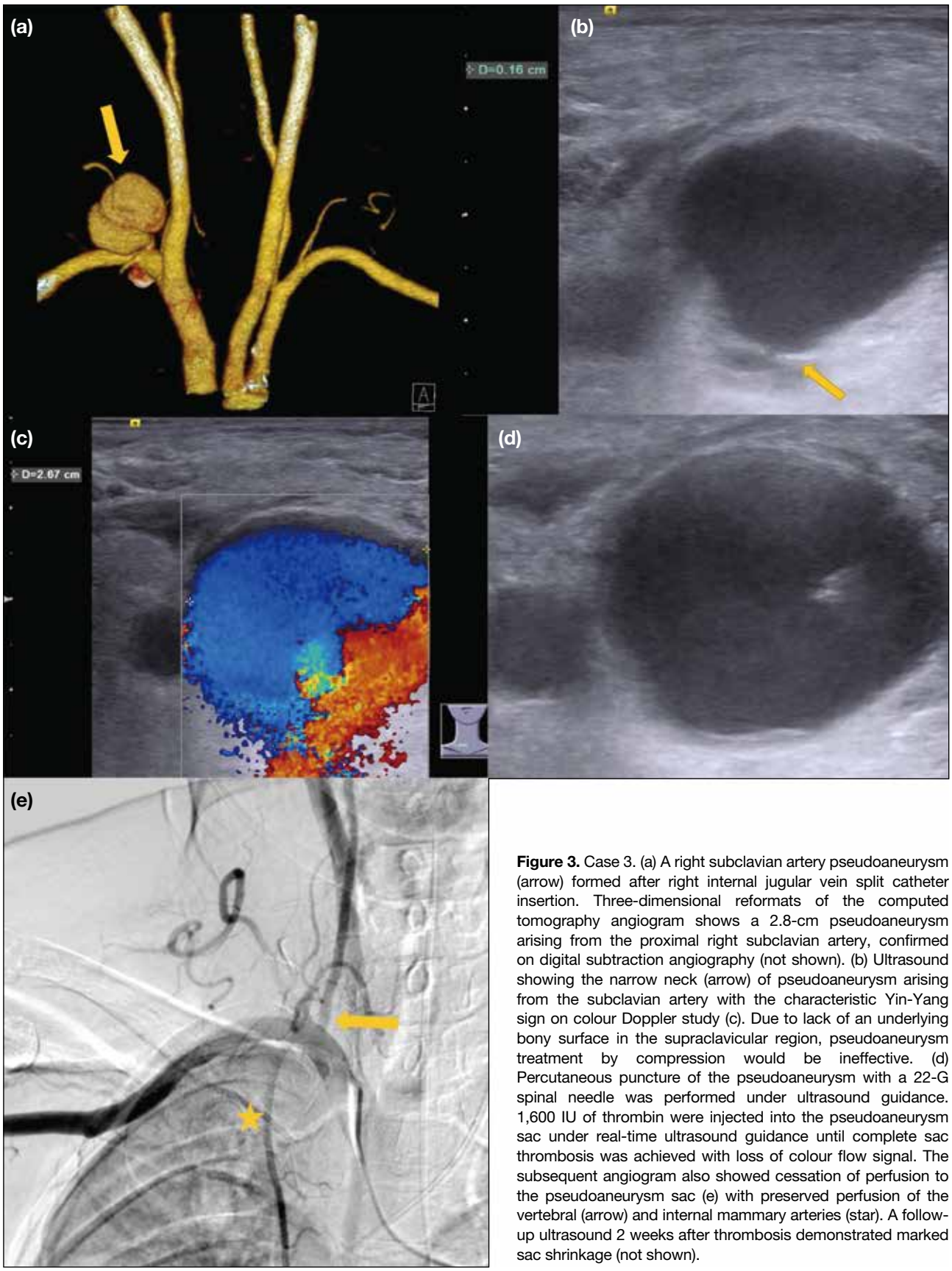

Figure 3. Case 3. (a) A right subclavian artery pseudoaneurysm (arrow) formed after right internal jugular vein split catheter insertion. Three-dimensional reformats of the computed tomography angiogram shows a 2.8-cm pseudoaneurysm arising from the proximal right subclavian artery, confirmed on digital subtraction angiography (not shown). (b) Ultrasound showing the narrow neck (arrow) of pseudoaneurysm arising from the subclavian artery with the characteristic Yin-Yang sign on colour Doppler study (c). Due to lack of an underlying bony surface in the supraclavicular region, pseudoaneurysm treatment by compression would be ineffective. (d) Percutaneous puncture of the pseudoaneurysm with a 22-G spinal needle was performed under ultrasound guidance. 1,600 IU of thrombin were injected into the pseudoaneurysm sac under real-time ultrasound guidance until complete sac thrombosis was achieved with loss of colour flow signal. The subsequent angiogram also showed cessation of perfusion to the pseudoaneurysm sac (e) with preserved perfusion of the vertebral (arrow) and internal mammary arteries (star). A follow-up ultrasound 2 weeks after thrombosis demonstrated marked sac shrinkage (not shown).

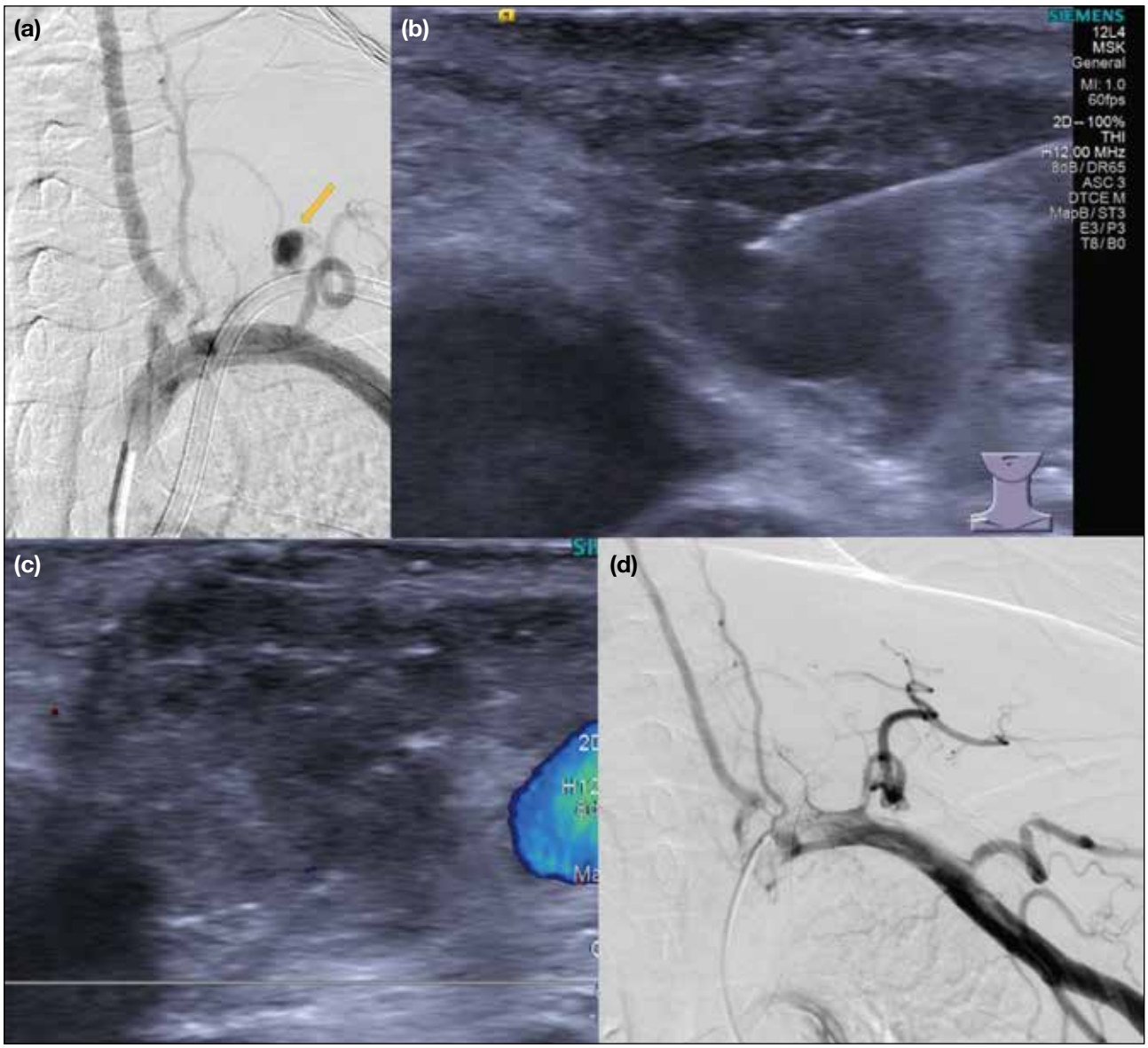

Figure 4. Case 4. Left thyrocervical trunk pseudoaneurysm after left internal jugular vein catheterisation. Digital subtraction angiography (a) shows a pseudoaneurysm (arrow) arising from the left thyrocervical trunk. A trial of endovascular catheterisation of the pseudoaneurysm for coiling was unsuccessful due to tortuous feeding vessels. (b, c) A percutaneous thrombin injection of 1,250 IU was performed under ultrasound guidance and real-time monitoring until complete sac thrombosis with loss of colour Doppler flow signal was carried out. (d) A subsequent left subclavian angiogram confirmed successful embolisation of the pseudoaneurysm.

stripping with snare-ride technique can be helpful in achieving release and successful removal of the catheter that was stuck to the vessel wall by adherent fibrin sheath (Figure 7).

CONCLUSION

In the unfortunate event of iatrogenic vascular injury during catheterisation, prompt assessment with computed tomographic angiography to delineate the intravascular course of the malpositioned catheter, its relationship to adjacent vital vasculature, and detection of complications is crucial for treatment planning. Careful planning of extraction routes and use of appropriate retrieval devices for retained catheter components are pivotal. Multidisciplinary collaboration, providing knowledge in different interventional radiological treatment options, can enable safe and effective intervention with reduced patient morbidity and enhanced recovery.

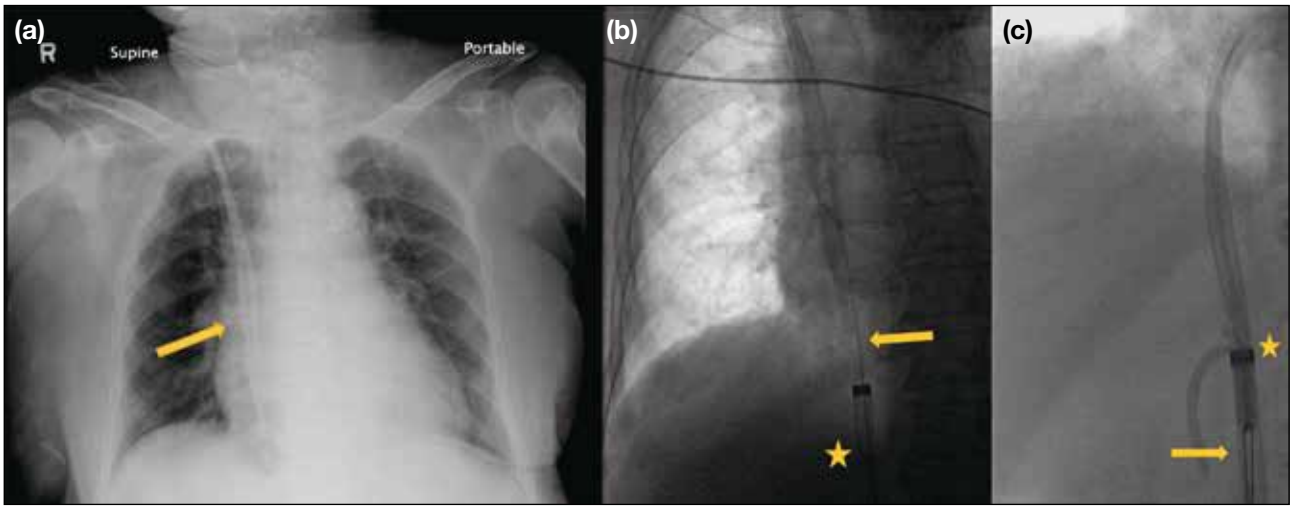

Figure 5. Case 5. Fragmented 10-Fr Ash Split Cath (Medcomp, Harleysville [PA], US) endovascular retrieval using transfemoral venous access. Chest X-ray (a) showing a segment of the catheter (arrow) dislodged into the superior vena cava and the right atrium. In view of the calibre of the catheter and the possibility of it doubling up during retrieval, a more sizable vascular sheath was employed to accommodate the retrieved catheter. Following ultrasound-guided puncture of right femoral vein with an 18-G needle and tract dilatation with a 10-Fr dilator, a 16-Fr vascular sheath (Performer introducer sheath; Cook Medical, Bloomington [IN], US) [stars] was inserted. The catheter was retrieved (b, c) using a 20-mm Amplatz Goose Neck snare kit (ev3 Inc, Plymouth [MN], US) [arrows] inserted into the vascular sheath (stars). Haemostasis at the femoral venous puncture site was achieved with manual compression.

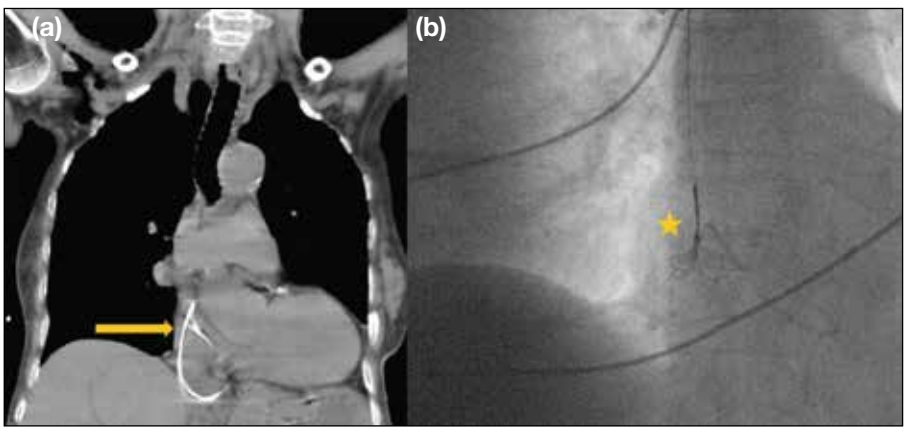

Figure 6. Case 6. Endovascular retrieval of a Hickman catheter fragment by transjugular venous access. (a) Computed tomography of the thorax demonstrates a Hickman catheter (arrow) fragment within the right atrium. (b) Via right internal jugular venous access (star), a 6-Fr EN Snare (Merit Medical, West Jordan [UT], US) was deployed with successful retrieval of the retained Hickman catheter fragment under fluoroscopic guidance.

REFERENCES

1. Saugel B, Scheeren TW, Teboul JL. Ultrasound-guided central venous catheter placement: a structured review and recommendations for clinical practice. Crit Care. 2017;21:225.
2. Ben Mrad I, Ben Fatma L, Ben Mrad M, Miri R, Mleyhi S, Mami I, et al. Endovascular management of a subclavian arterial injury during central venous catheter placement for hemodialysis. Open Access Emerg Med. 2021;13:273-7.
3. Pikwer A, Acosta S, Kölbel T, Malina M, Sonesson B, Akeson J. Management of inadvertent arterial catheterisation associated with central venous access procedures. Eur J Vasc Endovasc Surg. 2009;38:707-14.
4. Practice guidelines for central venous access 2020: an updated report by the American Society of Anesthesiologists Task Force on Central Venous Access [editorial]. Anesthesiology. 2020;132:8-43.
5. Guilbert MC, Elkouri S, Bracco D, Corriveau MM, Beaudoin N, Dubois MJ, et al. Arterial trauma during central venous catheter insertion: case series, review and proposed algorithm. J Vasc Surg. 2008;48:918-25; discussion 925.
6. Dornbos DL 3rd, Nimjee SM, Smith TP. Inadvertent arterial placement of central venous catheters: systematic review and guidelines for treatment. J Vasc Interv Radiol. 2019;30:1785-94.
7. Ng KT, Chau CM, Chan HF, Cheng LF, Ma KF, Chan KM.

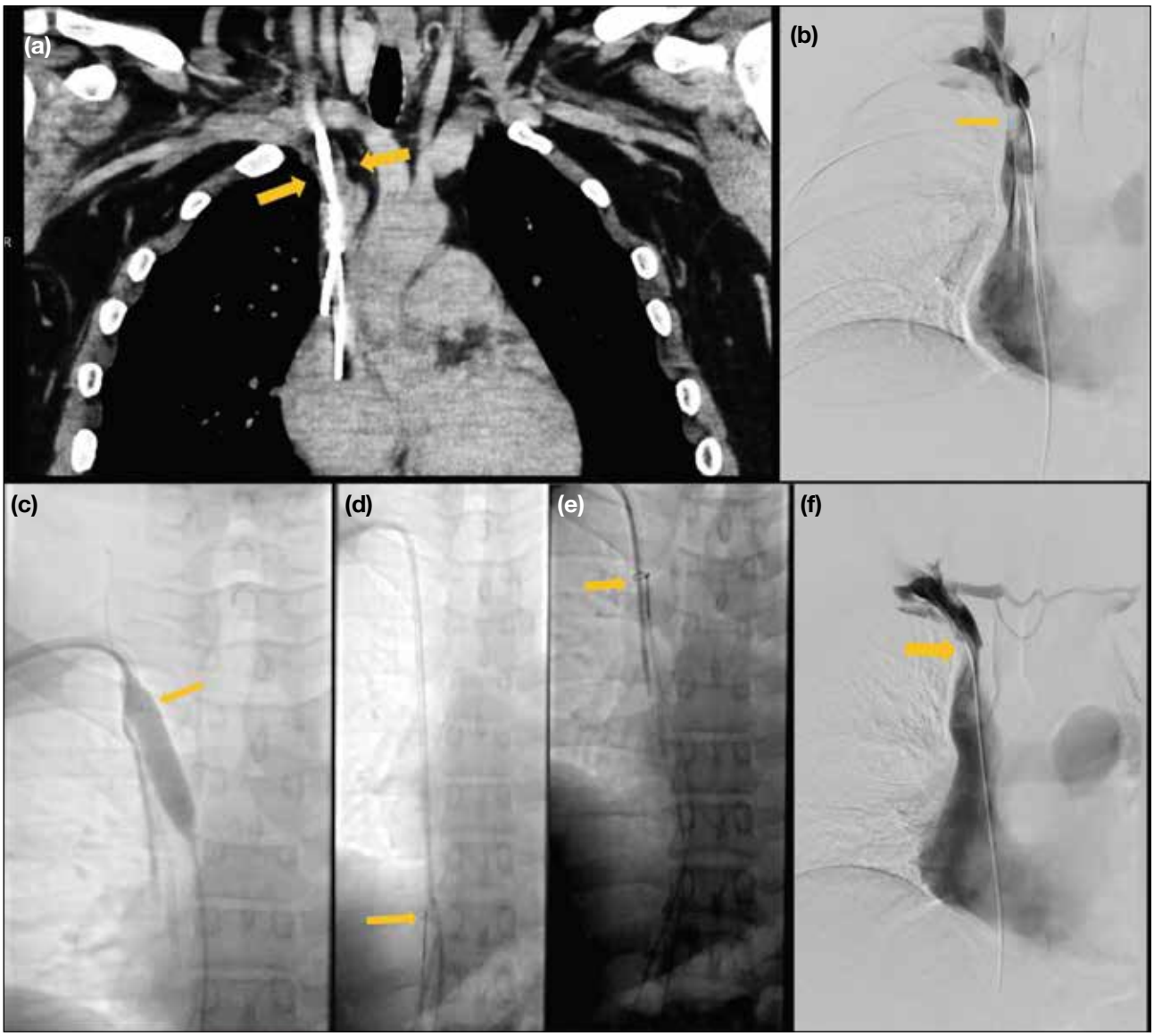

Figure 7. Case 7. Fibrin sheath stripping with snare-ride technique for removal of a right internal jugular Split Cath catheter with prior failed bedside removal. The catheter had been used for 18 months. Computed tomography of the thorax (a) reveals ill-defined bandlike pericatheter hypodensities (arrows) in the superior vena cava (SVC), with corresponding SVC stenosis demonstrated on catheter fluoroscopy (arrow in [b]), due to underlying fibrin sheath formation. Passage of a 0.035-inch Terumo guidewire down to the inferior vena cava (IVC) via the Split Cath catheter (Medcomp, Harleysville [PA], US) and a 4-Fr multipurpose catheter (Merit Medical, West Jordan [UT], US). (c) Right common femoral venous access followed by balloon venoplasty (arrow) along the stenotic SVC segment did not result in successful catheter removal. (d, e) Through-and-through wire access was established by passing the IVC guidewire downwards to the right femoral venous access. A gooseneck snare (Amplatz; ev3 Inc, Plymouth [MN], US) [arrows] was inserted via a right common femoral sheath along with the through-and-through wire to capture the split catheter by the snare-ride technique. Stripping of the fibrin sheath was performed with use of the gooseneck snare (note change in position of the snares as indicated by arrows in [d] and [e]), with successful removal of the catheter with part of the fibrin sheath from the jugular side. (f) Post-procedure angiogram shows mild residual SVC stenosis (arrow) which was patent without thrombus or extravasation.

Percutaneous repair of inadvertent brachiocephalic arterial puncture by closure device: a case report. Hong Kong J Radiol. 2020;23:134-8.
8. Lorenzo JF, Rey JV, Arquillo IL, Encisa de Sá JM. Off-label use of ProGlide percutaneous closure device in iatrogenic arterial catheterizations: our experience. Vascular. 2020;28:756-9.
9. Sharma M, Sakhuja R, Teitel D, Boyle A. Percutaneous arterial closure for inadvertent cannulation of the subclavian artery—a call for caution. J Invasive Cardiol. 2008;20:E229-32.
10. Sarioglu O, Capar AE, Belet U. Interventional treatment options in

pseudoaneurysms: different techniques in different localizations. Pol J Radiol. 2019;84:e319-27.
11. Lo AX, Hon TY, Luk WH, Loke TK, Lo SS, Chan JC. Ultrasound-guided thrombin injection for pseudoaneurysms: a case series at a local hospital. Hong Kong Med J. 2012;18:333-7.
12. Woodhouse JB, Uberoi R. Techniques for intravascular foreign body retrieval. Cardiovasc Intervent Radiol. 2013;36:888-97.
13. Faintuch S, Salazar GM. Malfunction of dialysis catheters: management of fibrin sheath and related problems. Tech Vasc Interv Radiol. 2008;11:195-200.

CATEGORIES OF PAPERS

Hong Kong Journal of Radiology publishes various categories of articles. Each category serves a distinct purpose and is judged by different criteria.

EDITORIAL

Commissioned article presenting the author's opinion on a topical subject or an article published in the current issue. Unsolicited Editorials are not accepted.

Format: An abstract is not required. The text is limited to 1000 words, with a maximum of 1 table or figure, and up to 10 references.

REVIEW ARTICLE

Systematic reviews or meta-analyses of recent developments in a specific topic. Scoping reviews of the literature that identify area(s) for future research will also be considered. No new information is described, and no subjective opinion or personal experiences are expressed.

Format: A structured abstract of ≤ 250 words; headings should include: Introduction, Methods, Results, Conclusion. The text is limited to 5000 words, with a maximum of 20 tables and figures (total), and up to 60 references.

ORIGINAL ARTICLE

Provides new information based on original research. Includes prospective studies with in-depth statistical analysis, unique retrospective observations of a disease or disorder, and studies of novel applications of an interventional procedure or treatment method.

Format: A structured abstract of ≤ 250 words; headings should include: Introduction, Methods, Results, Conclusion. The text is limited to 3500 words, with a maximum of 20 tables and figures (total), and up to 50 references.

PERSPECTIVE

Narrative review articles discussing recent developments in a specific topic. No new information is described; may include subjective opinion or personal experiences.

Format: An unstructured abstract of ≤ 250 words. The text is limited to 2500 words, with a maximum of 20 tables and figures (total), and up to 60 references.

PICTORIAL ESSAY

Teaching exercise with message in the figures and legends. Emphasis is on quality of the illustrations and clinical relevance of the message.

Format: An abstract is not required. The text is limited to 2500 words, with a maximum of 20 tables and figures (total), and up to 15 references.

CASE REPORT

Brief discussion of a case with unique features not previously described. Additional cases (case series) may be added to augment the discussion. The discussion should be succinct and focus on a specific message.

Format: An abstract is not required. The text is limited to 1500 words, with a maximum of 8 tables and figures (total), and up to 15 references.

BRIEF COMMUNICATION

This includes post-meeting commentary, update on new imaging or therapeutic advances, brief description of a specific technique or procedure or new equipment. Teaching exercise aimed at describing a certain radiological or radiotherapeutic technique for trainees and practising radiologists is also welcome.

Format: An abstract is not required. The text is limited to 1500 words, with a maximum of 8 tables and figures (total), and up to 15 references.

LETTER TO THE EDITOR

Short letter on any matter of interest to journal readers, including comments on an article that has previously appeared in the journal. The authors of the article commented on would be invited to reply.

Format: An abstract is not required. The text is limited to 500 words, with up to 5 references. Figures and tables are permitted only exceptionally.

INFORMATION FOR AUTHORS

Aims and Scope

Hong Kong Journal of Radiology is the official peer-reviewed academic journal of the Hong Kong College of Radiologists. It is a multidisciplinary journal covering research work pertaining to the science and practice of the component specialties of the College. The journal publishes various categories of papers, including Reviews, Original Articles, Perspectives, Pictorial Essays, Case Reports, Brief Communications, and Letters to the Editor. Manuscripts will be subject to rigorous peer review. *HKJR* adheres to the Recommendations for the Conduct, Reporting, Editing, and Publication of Scholarly Work in Medical Journals of the International Committee of Medical Journal Editors (ICMJE; www.icmje.org), and the Core Practices of the Committee on Publication Ethics (COPE; publicationethics.org/).

Journal Policies

Reporting Guidelines: *HKJR* recommends the use of reporting guidelines in the preparation of manuscripts, such as those advocated by the EQUATOR Network (eg, CONSORT for randomised trials).

Funding: Any sponsor(s) of the research involved, along with grant number(s) should be provided.

Conflicts of interest: All authors must provide a statement reporting any conflicts of interest. Where none exist, please state 'The authors have no conflicts of interest to declare.'

Ethics: All studies must be conducted in accordance with the Declaration of Helsinki. For studies involving humans, a statement must be included in the manuscript that provides the name of the review board and approval number (or waiver). A statement on patient/guardian consent must also be included. For studies involving animals, appropriate ethics approval is required, and this should be stated in the manuscript.

Submission: Manuscripts should be submitted online via HKAMedTrack (www.hkamedtrack.org/hkjr). Manuscripts must be unpublished works that are not under consideration by another publication.

Copyright: On acceptance of an article by the journal, the corresponding author will be asked to transfer copyright of the article to the College.

Editing: Accepted manuscripts will be copyedited according to journal style. Authors are responsible for all statements made in their work, including changes made by the copy editor.

Proofs and Reprints: The corresponding author will receive page proofs, which should be proofread and returned promptly. Corrections are limited to printer's errors — no substantial author's changes will be made without charge. Quotes for extra copies of reprints are available at the Editorial Office.

Manuscript Preparation

In general, manuscripts should be prepared following the 'IMRaD' structure as recommended by the ICMJE. Please provide a **blinded** manuscript and separate title page in Word format (.doc or .docx). Manuscripts must be written in English. For accepted manuscripts, an abstract in Traditional Chinese will also be required.

Authors: Provide the full name, qualifications (maximum of two), and affiliation (where the study was conducted) for all authors. The authors' names in Chinese characters, if available, should also be provided. **The corresponding author**, on behalf of the authors, is responsible for all contact with the journal. Provide the full name, postal address, telephone and fax numbers, and email address of the corresponding author.

Title: Concisely convey the main topic of the study. Avoid obvious terms such as "a study of" or "novel". If appropriate, please include the study design in the title (eg, 'randomised controlled trial', 'systematic review', 'case report'). An abbreviated title of <45 characters is also required.

Abstract: For article types requiring an abstract, this should provide a complete summary of the article, including the aims/purpose, main methods, key results, and conclusions. Abbreviations and clinical or technical jargon should be avoided. Please refer to the Categories of Papers for details.

Key Words: A maximum of five relevant index terms should be provided, selected from the Medical Subject Headings (MeSH; www.ncbi.nlm.nih.gov/mesh).

Tables: Submit tables on separate pages in as simple a format as possible. They should be numbered and concisely titled. Abbreviations should be defined in footnotes.

Figures: Restricted to the minimum necessary to support the textual material. Illustrations should be submitted as separate files (.jpg format, ≥350-dpi resolution). All figures should be numbered with a legend to indicate the anatomical area and pathological condition shown. All symbols and abbreviations should be defined in the legend. Please ensure that legends and illustrations correspond.

References: Should be numbered in the order in which they are first cited in the text. Each reference citation should be in superscript Arabic numerals after full-stops and commas. In the reference list, include the complete title, and names and initials of all authors.

Acknowledgement(s): Any individuals who contributed substantially to the study but does not qualify for inclusion as an author should be acknowledged. Written permission from acknowledged individuals is required.

Please refer to the *HKJR* website for further guidance:
http://www.hkjr.org/page/information-authors